JOINT INSTITUTE FOR NUCLEAR RESEARCH

January 12, 2022

Technical design Report of the Spin Physics Detector

Draft version 2022.005

This draft is the internal document
of the SPD collaboration
and must not be shown in public!

Contents

Preface

According to the astrophysical and cosmological data, the relative contribution of visible baryonic matter, the properties of which are determined by strong and electromagnetic interactions, is about 5% of the Universe mass. With respect to two other components, dark matter and dark energy, baryonic matter seems to be a well-studied subject. In fact, despite the great advances in quantum chromodynamics made in describing the interaction of quarks and gluons within the framework of the perturbative approach, the question of why nucleons are exactly like we see them, remains open. Understanding the structure and the fundamental properties of the nucleon directly from the dynamics of its quarks and gluons based on the first principles is one of the main unsolved problems of QCD.

The nucleon behaves like a spinning top with a spin of $\hbar/2$. This spin is responsible for such fundamental properties of Nature as the nucleon magnetic moment, different phases of matter at low temperatures, the properties of neutron stars, and the stability of the known Universe. That is why the study of the spin structure of the nucleon is of particular importance. The naive quark model has successfully predicted most of the gross properties of hadrons, such as charge, parity, isospin and symmetry properties and their relations. Some of the dynamics of particle interactions can be qualitatively understood in terms of this model as well. However, it falls short in explaining the spin properties of hadrons in terms of their constituents. Since the famous "spin crisis" that began in 1987, the problem of the nucleon spin structure remains one of the most intriguing puzzles in the contemporary high-energy physics. The central problem, for many years attracting both enormous theoretical and experimental efforts, is the problem of how the spin of the nucleon is built up from spins and orbital momenta of its constituents – the valence and sea quarks and gluons. A full description can be given in terms of the so-called transverse-momentum dependent parton distribution functions.

Over the last 25 years, both polarized deep inelastic scattering experiments (CERN, DESY, JLab, SLAC) and high-energy polarized proton-proton collisions (RHIC at BNL) have been the major providers of information about spin-dependent structure functions of the nucleon. Nevertheless, our knowledge of the internal structure of the nucleon is still limited. This is especially true of the gluon contribution. New facilities for spin physics, such as the Electron-Ion Collider at BNL and the fixed-target experiments at CERN LHC are planned to be built in the near future to get the missing information.

The Spin Physics Detector, a universal facility for studying the nucleon spin structure and other spin-related phenomena with polarized proton and deuteron beams, is proposed to be placed in one of the two interaction points of the NICA collider that is under construction at the Joint Institute for Nuclear Research (Dubna, Russia). At the heart of the project there is huge experience with polarized beams at JINR. The main objective of the proposed experiment is the comprehensive study of the unpolarized and polarized gluon content of the nucleon. Spin measurements at the Spin Physics Detector at the NICA collider have bright perspectives to make a unique contribution and challenge our understanding of the spin structure of the nucleon.

The Conceptual Design Report of the Spin Physics Detector was presented at the 54th meeting of the

JINR Program Advisory Committee for Particle Physics on Jan. 2021 and approved at the 54th meeting on Jan. 2022 basing on the report of the international SPD Detector Advisory Committee.

In this document the Technical Design of the Spin Physics Detector is presented.

Chapter 1

Executive summary

The Spin Physics Detector collaboration proposes to install a universal detector in the second interaction point of the NICA collider under construction (JINR, Dubna) to study the spin structure of the proton and deuteron and the other spin-related phenomena using a unique possibility to operate with polarized proton and deuteron beams at a collision energy up to 27 GeV and a luminosity up to 10^{32} cm^{-2} s^{-1}. As the main goal, the experiment aims to provide access to the gluon TMD PDFs in the proton and deuteron, as well as the gluon transversity distribution and tensor PDFs in the deuteron, via the measurement of specific single and double spin asymmetries using different complementary probes such as charmonia, open charm, and prompt photon production processes. Other polarized and unpolarized physics is possible, especially at the first stage of NICA operation with reduced luminosity and collision energy of the proton and ion beams. The SPD physics program is described in detail in [1-3]. This document is dedicated exclusively to technical issues of the SPD setup construction.

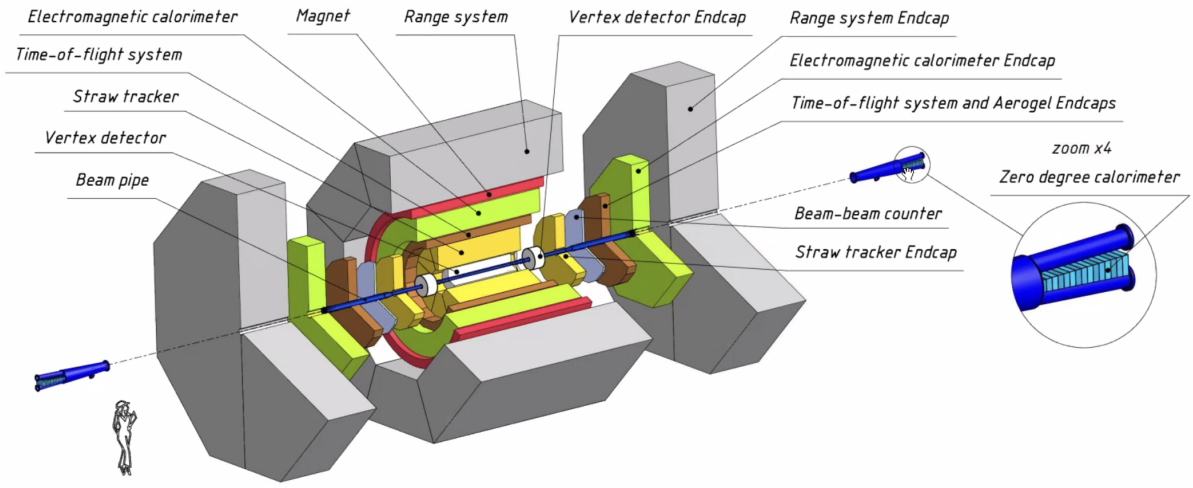

Figure 1.1: General layout of the SPD setup.

The SPD experimental setup is designed as a universal 4π detector with advanced tracking and particle identification capabilities based on modern technologies that will be installed in the SPD experimental hall of the NICA collider. The silicon vertex detector (VD) will provide resolution for the vertex position on the level of below 100 μm needed for reconstruction of secondary vertices of D-meson decays. The straw tube-based tracking system (ST) placed within a solenoidal magnetic field of up to 1 T at the detector axis should provide the transverse momentum resolution $\sigma_{p_T}/p_T \approx 2\%$ for a particle momentum

of 1 GeV/c. The time-of-flight system (PID) with a time resolution of about 60 ps will provide 3σ π/K and K/p separation of up to about 1.2 GeV/c and 2.2 GeV/c, respectively. Possible use of the aerogel-based Cherenkov detector in the end-caps will extend this range. Detection of photons will be provided by the sampling electromagnetic calorimeter (ECal) with the energy resolution $\sim 5\%/\sqrt{E}$. To minimize multiple scattering and photon conversion effects for photons, the detector material will be kept to a minimum throughout the internal part of the detector. The muon (range) system (RS) is planned for muon identification. It can also act as a rough hadron calorimeter. The pair of beam-beam counters (BBC) and zero-degree calorimeters will be responsible for the local polarimetry and luminosity control. To minimize possible systematic effects, SPD will be equipped with a free-running (triggerless) DAQ system. A high collision rate (up to 4 MHz) and a few hundred thousand detector channels pose a significant challenge to the DAQ, online monitoring, offline computing system, and data processing software.

The SPD operation could be started already in 2028 using the possibilities of polarized p-p and d-d collisions at $\sqrt{s} < 9.4$ GeV and $\sqrt{s} < 4.5$ GeV/nucleon, respectively, as well as A-A collisions. The starting configuration could consist of the range system, solenoidal magnet, straw tube-based tracking system, and the pair of zero-degree calorimeters. A simple micromegas-based detector could be installed in the central region instead of the sophisticated vertex detector to improve the momentum resolution.

The estimated cost of the Spin Physics Detector in its full configuration is about 96 M$ at current prices. Any expenses related to the development and construction of the infrastructure for polarized beams at NICA are out of this estimation.

Chapter 4

General concept of the SPD experiment

NICA, a new research facility aimed at the study of the properties of the strong interaction, is under construction at JINR and should be put to operation at the end of 2023. At the first stage of operation, the study of hot and dense baryonic matter will be performed in heavy-ion collisions with the MultiPurpose Detector (MPD) placed at the first interaction point of the collider. This study should shed light on the in-medium properties of hadrons and the nuclear matter equation of state, the onset of deconfinement, chiral symmetry restoration, phase transition, existence of mixed phase and the critical end-point, etc. The collider also provides the ability to operate with polarized proton and deuteron beams of high intensity that will be used for the study of the polarized structure of proton and deuteron with the Spin Physics Detector (SPD) installed in the second interaction point.

The main goal of the SPD experiment is to get information about the gluon Transverse Momentum-Dependent Parton Distribution Functions (TMD PDFs) in the proton and deuteron, as well as the gluon transversity distribution and tensor PDFs in the deuteron, via the measurement of specific single and double spin asymmetries using such complementary probes as charmonia, open charm, and prompt photon production processes. This physics task imposes general requirements on the concept of the experimental setup.

Unlike the case of high-energy collisions where the collision energy $\sqrt{s}$ is a few orders of magnitude higher than a typical hard scale Q of the studied reactions, at the SPD energies for all the probes planned to be used to access the gluon content of the colliding particles $Q \sim M_{J\psi} \sim 2M_D \sim p_{T\gamma\,min}$ is just a few times less than $\sqrt{s}/2$. Therefore, one should expect quite a uniform distribution of all signal particles (muons from the J/ψ decay, prompt photons, products of D-mesons decay, etc.) over the kinematic range. In other words, there is no preferable range in rapidity, which could be specified for each probe for the optimal overall performance. Together with relatively small cross-sections of the discussed probes, this fact leads one to a requirement of $\sim 4\pi$ coverage of the SPD setup.

The Spin Physics Detector must have sufficient tracking capabilities and a magnetic system for spectrometric purposes for the majority of the addressed physics tasks. It has to be equipped with a muon system thick enough for effective separation of muons and hadrons to make it possible to deal with the decay $J/\psi \to \mu^+\mu^-$. A precision vertex detector is needed for the recovering of the secondary vertices from the decays of $D^{\pm/0}$ mesons and other short-lived particles. An electromagnetic calorimeter ensures the capability to detect signal and background photons. A low material budget and general transparency of the setup should also provide favorable conditions for photon physics. Hadron identification capability is needed for any physics task with protons and/or kaons in the final state, in particular, to enforce a signal-to-background ratio for D-mesons selection, and also to improve tracking at low momenta. Since tiny effects are intended to be investigated, a triggerless DAQ system is planned in order to minimize

possible systematic uncertainties of the measurements.

Strict limitations to the SPD detector layout arise from the external conditions, such as the maximal possible load to the floor of the SPD experimental hall (1500 tons together with the lodgement and the detector moving system). Together with the requirement to have the overall thickness of the muon system not less than 4 nuclear interaction lengths (Λ_I), this limits the outer size of the SPD detector and the size of the inner part of the detector. The location of the collider infrastructure, in particular, focusing elements, also defines the size of the SPD setup along the beam axis.

Although *p-p* and *d-d* collisions can be studied at MPD as a reference, and SPD setup has limited capabilities to operate with ion collisions, each of the detectors is optimized for its tasks. MPD with the TPC-based tracking system can disentangle hundreds of charged tracks but can not operate at luminosity above 10^{29} cm^{-2} s^{-1}. The design of the MPD detector does not provide for the construction of a full-fledged muon system. Conversely, the SPD should feel good at high luminosity (up to 10^{32} cm^{-2} s^{-1}) but low track multiplicity. Thus, the two experiments can not simultaneously perform their main tasks therefore, they will operate sequentially SPD after MPD. Based on the plans for putting into operation and commissioning of the accelerator complex, development of the NICA polarized infrastructure, the plans of the MPD collaboration for technical and physics runs as well as on realistic assumptions of the SPD funding, we propose the following stages of the SPD project implementation. The **first stage**

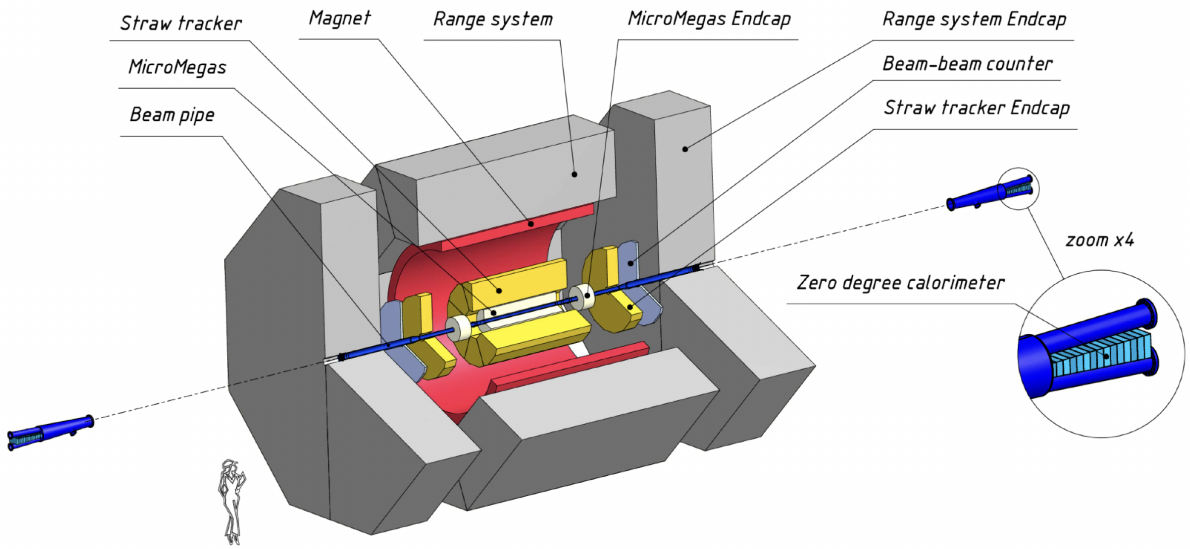

Figure 4.1: General layout of the SPD setup at the first stage.

of the SPD experiment will be devoted to the study of polarized and non-polarized phenomena at low energies and reduced luminosity using heavy ion (up to Ca) and polarized proton and deuteron beams such as: polarized phenomena in elastic *p-p* and *d-d* scattering and other exclusive reactions, spin effects in hyperon production, production of dibaryon resonances and hypernuclei, near-threshold charmonia production, etc. The duration of the first stage can be up to two years. It implies construction of a minimum setup configuration that should include (see Fig. 4.1):

- a Range System (supporting structure of the entire installation and a magnet yoke, muon identification);
- a superconducting magnet (charged particle momentum reconstruction);
- a Straw-based Tracking system (charged particle momentum reconstruction);

– a simple tracker in the inner part of the detector (charged particle momentum reconstruction);

– a Beam-Beam Counter (local polarimetry and luminosity control);

– a Zero Degree Calorimeter (local polarimetry and luminosity control).

It could include also some elements of an Electromagnetic Calorimeter for physics with photons and a local π^0-based polarimetry.

We expect that for the first stage the collider will be able to operate with polarized protons and deuterons in the spin transparency mode. The absolute value of the beam polarization should be not less than 0.5 for protons and 0.6 for deuterons. Collisions of longitudinally and transversely polarized particles, *p-p* and *d-d* (in all combinations: LL, TT, TL and LT), will be available at any energy up to $\sqrt{s} = 9.4$ GeV for protons and $\sqrt{s} = 4.5$ GeV/nucleon for deuterons. The corresponding luminosity is up to about 10^{31} cm^{-2} s^{-1} and 10^{30} cm^{-2} s^{-1}, respectively. Both vertical and radial directions for will be possible for the transverse polarization. Tensor polarization for deuteron will also be available. Absolute polarimetry is expected to be provided with accuracy not worse than 5% for both vertical and radial directions. We also expect that it will be possible to operate in the mode of heavy-ion collision.

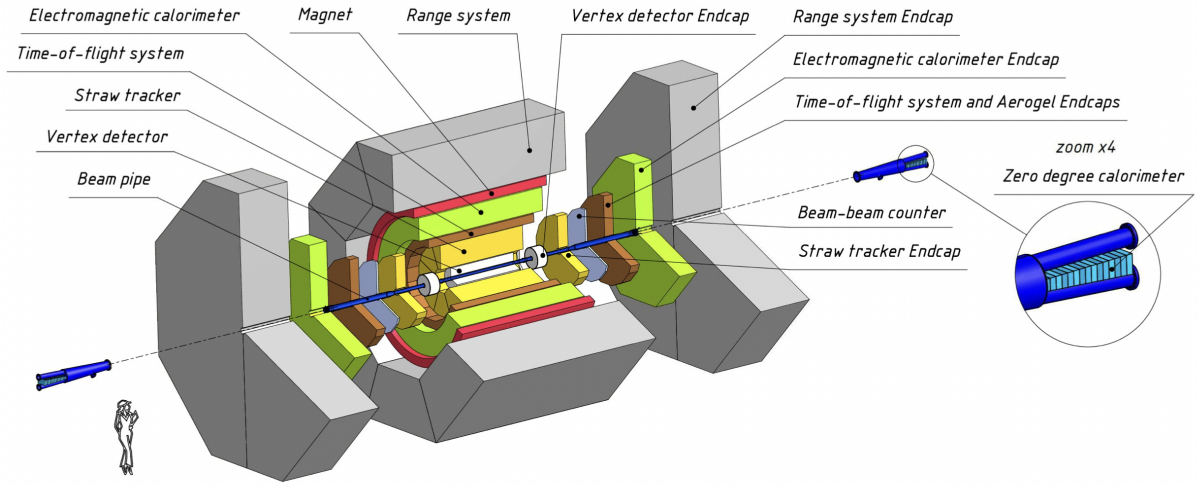

Figure 4.2: Final layout of the SPD setup.

The main part of the SPD physics program of the experiment, the study of the polarized gluon content in proton and deuteron, is planned to be implemented during the **second stage** with the full setup (see Fig. 4.2). This stage can last not less than 4 years. By then we expect the accelerator to be able to deal with polarised protons and deuterons up to energies of 27 and 13.5 GeV/nucleon in the centre of mass system and luminosities of 10^{32} cm^{-2} s^{-1} and 10^{31} cm^{-2} s^{-1}, respectively The transverse polarisation for protons will be available for all energies, while the longitudinal polarisation will be available at spin resonance points with a beam energy step 0.51 GeV. The tentative running plans of the SPD project are presented in Fig. 4.3.

Taking into account the high degree of integration of the detector subsystems, we decided to present the SPD Technical Design Report as a single document. The general subsystems as well as the subsystems that are assumed to be part of the first phase are highly elaborated. The subsystems of the second phase are described in a more schematic way.

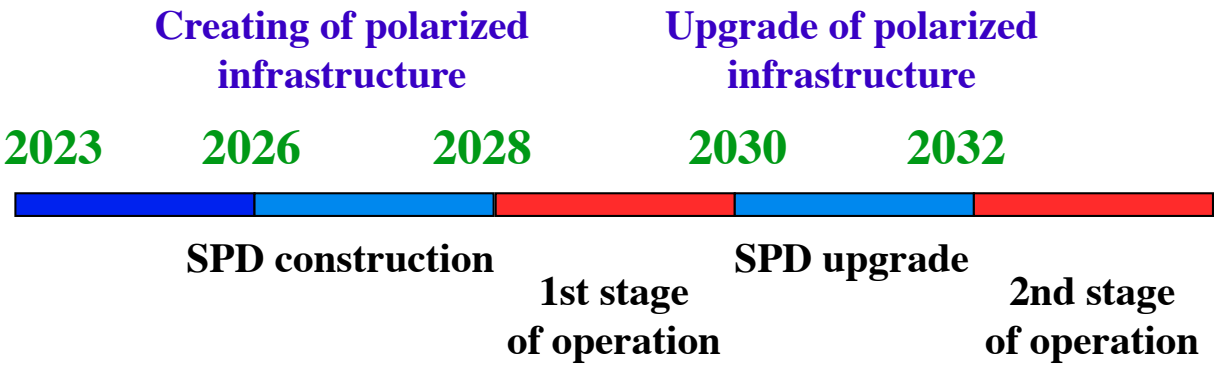

Figure 4.3: Tentative running plans of the SPD project.

1. Electromagnetic calorimeter concept.

The electromagnetic calorimeter (further calorimeter) should meet the criteria imposed by the physical goals of the SPD [1] experiment of various nature and importance. The most important criteria arises from the physical requirements to measurement accuracy of energies, trajectories, and timing of photons and electrons. Technological possibilities of modern experimental physics should be taken into account when choosing the calorimeter setup. Cost factors should be considered also to ensure the feasibility of the project. High multiplicity of secondary particles leads to a requirements of high segmentation and high dense of absorber's medium with a small Moli`ere radius. It is required in order to have sufficient spacial resolution and a capability to resolve overlapping showers. The transverse size of the calorimeter cell should be of the order of the Moli`ere radius. A reliable reconstruction of photons and neutral pions is possible only for small overlap of showers. Occupancy should not exceed 5%, in order to make possible efficient photons reconstruction−with high precision. The SPD experiment imposes the following requirements on the calorimeter characteristics:

- reconstruction of photons and electrons in the energy range from 50 MeV to 10 GeV
- energy resolution for the above-mentioned particles: ∼5%/√E[GeV];
- good separation of two-particle showers;
- operation in the magnetic field;
- long-term stability: 2÷3% in a six month period of data taking.

The energy range requirement follows from the kinematic range of secondary particles, which are produced in a collision of protons with energy up to 27 GeV and emitted into 4π solid angle. Good energy resolution is required for identification and quantitative measurement of single photon and neutral pion energies. Good two-particle separation is needed to separate photon showers from the π0 decay in order to suppress background events in measurements with prompt photons. Long-term stability is necessary for polarization measurements featuring π0 reconstruction in the calorimeter, especially in the end-caps. Calorimeter instability may result in false asymmetry values. While it is essential to meet the physics requirements imposed on the calorimeter design, one should also take into account cost estimation and technical feasibility when choosing its granularity, because of the larger number of cells leads to higher costs of the manufacturing and readout electronics.

2. Overview of the SPD calorimeter.

The SPD electromagnetic calorimeter is placed between the Cryostat with magnet coils and the Particles Identification Detector (PID), as shown at Fig.1. The calorimeter consists of a barrel and two end-caps, covering a 4π solid angle. The outer dimensions of the calorimeter are

determined by the inner size of the Cryostat. The thickness of the calorimeter is determined by the required thickness of the active part and the size of the readout block consisting of photodiode and amplifier boards, as well as by the size of the flexible part of the fibers. For efficient absorption of electrons and photons with energies up to 10 GeV, the calorimeter thickness, which is defined by the number of sampling layers, should be at least 17÷20 X_0 in terms of radiation lengths X_0.

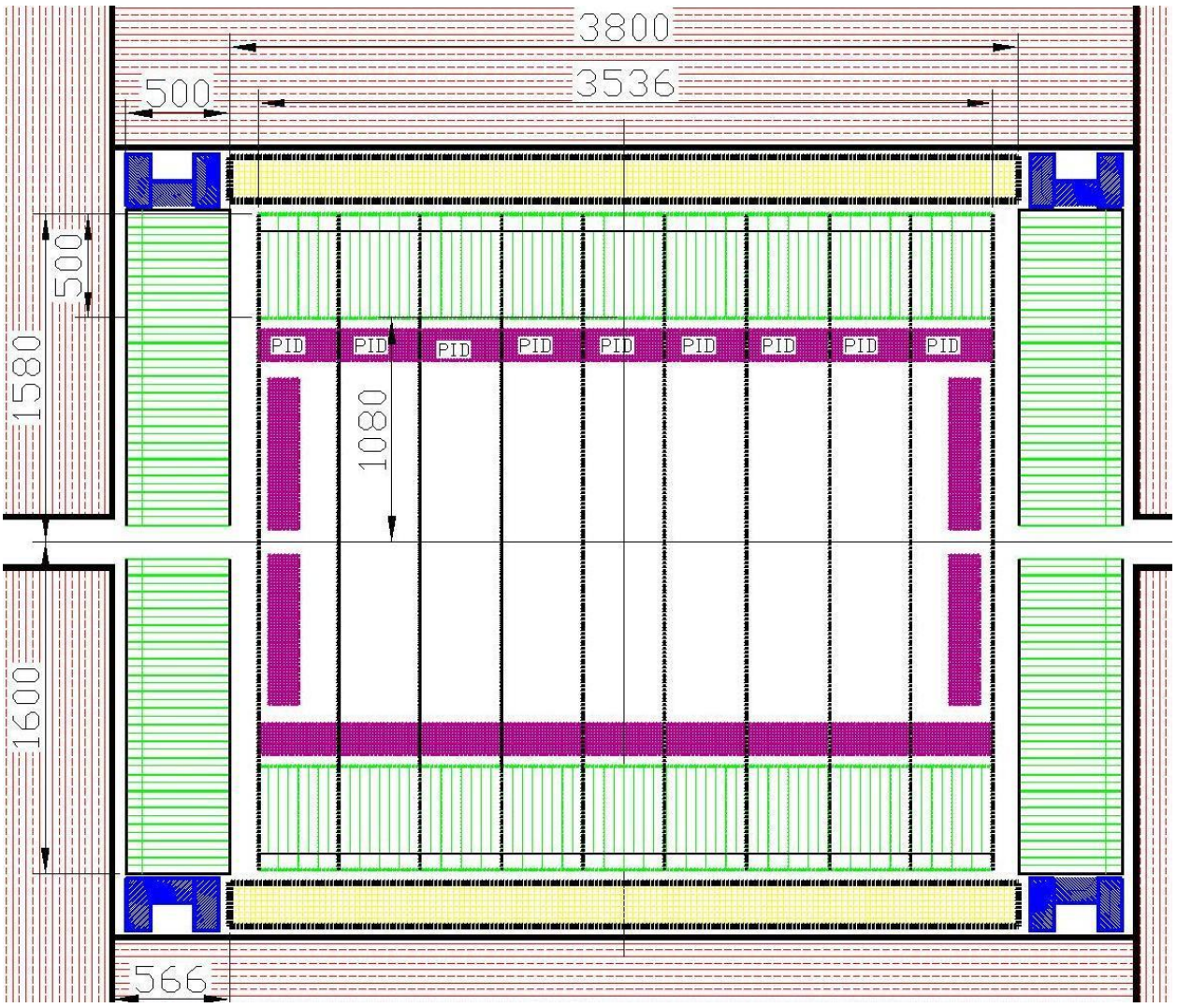

Figure 1: Barrel and End Cap parts of the calorimeter (green) , side view. Purple– PID, yellow – Cryostat, read - muons RS, blue – the frame for End-caps.

For the sampling structure of 190 layers of 1.5-mm polystyrene scintillator and 0.5-mm lead, the length of the active part is 380 mm, which corresponds to 17.6X0. The period of the structure is set to 2 mm in order to avoid optical contact between the lead and the scintillator, and because of the connection technique involves special ”Lego” spikes. The flexible parts of the fibers take up to 8 cm. The transverse size of the calorimeter cell should be of the order of the effective Moli`ere radius of the calorimeter medium, which is, in its turn, defined by the scintillator-to-lead sampling ratio. The selected structure has a Moli`ere radius of 5.2 cm. The separation efficiency of two photons with energies from 200 MeV to 500 MeV depends on the

cell size and reaches a plateau at a cell size of 40 mm, as it was determined in the MC simulation. Therefore, we have selected ~40 mm cell granularity for both of barrel and end-caps. Cells in the barrel part of the calorimeter have trapezoidal shape in the azimuthal direction to minimize the gaps between the modules. The vertex angle of the trapezoid equals 1.87^0.

2.1. **Barrel.**

A schematic drawing of the calorimeter barrel part is shown at Fig.1. Its transverse size is limited by the Cryostat and PID. The barrel part is composed by cells of trapezoidal shape in the azimuthal direction with a vertex angle of 1.87^0. The front size of one cell is equal to 34 mm. In the direction along the beam axis the cell size is equal to 48 mm. A schematic drawing of the calorimeter's barrel part is shown in Fig.2 (a), an isomeric calorimeter view is shown at Fig.2(b). The barrel consists of 44 annular layers, located one after another along the beam axis. Each layer of the calorimeter's barrel is composed of 96 modules along the ϕ angle. The design of the modules is described in more detail in Section 5. Each four layers of calorimeter barrel are grouped forming a ring containing 384 modules, or 1536 cells, with a total weight of 4 ton. The ring is made up of two half rings to facilitate motion and handling at installation. The combining of 4 layers into a single block is provided by usage of 2 mm thickness stainless steel sheets, which finally determines the gap between the layers. Subsequently, the half rings are combined into a single ring and mounted on 2 rails fixed to the cryostat inner side, as shown in Fig. 3. The calorimeter ring is divided into 24 sectors by the angle ϕ, thus forming a cluster of 64 cells which are read by one ADC, as shown in Fig. 2 (b).

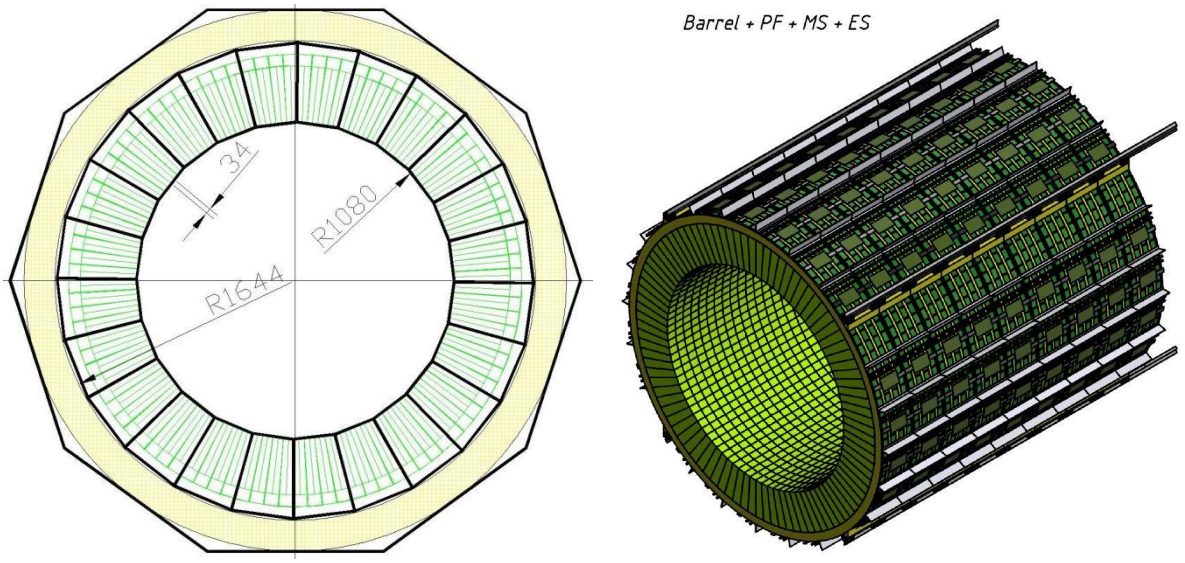

(a) (b)

Figure 2: Schematic drawing (a) of a cross-section of the barrel part of the calorimeter. It is sectioned into 192 cells azimuthally with a vertex angle of 1.87^0. All dimensions are in millimeters. The isometric view (b) shows assembled barrel part.

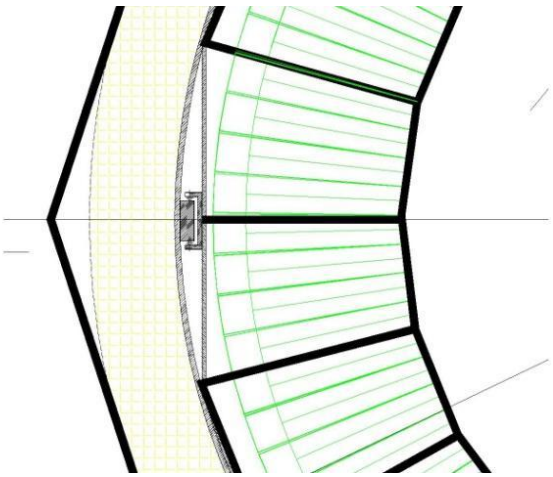

Figure 3: The rails to ECAL support and fastening to the cryostat's inner side.

Two roller trays support each calorimeter's ring.

There are 11 such rings installed inside of cryostat.

One ring has weight about 4 ton.

Figure 3: The rails to ECAL support and fastening to the cryostat's inner side. Two roller trays support each calorimeter's ring. There are 11 such rings installed inside of cryostat. One ring has weight about 4 ton.

Bias voltage for all 1536 cells of one ring is provided by 96 front end cards (FE-boards) and data acquisition from all these cells is provided by 24 pcs. of 64 channels ADC boards. All of 96 pcs of FE-boards, intended for one ring bias voltage, are controlled and power supplied by one HV module. See more details about related electronics below in sections 6, 7. The HV module is located outside of the barrel. It can be remotely placed at a distance up to 100 meters from the calorimeter. All 96 pcs FE-boards of one ring are connected to one HV module in parallel by one flat cable of 5-pair twisted wires. FE-cards are mounted directly on the calorimeter's module together with scintillator's light sense MPPCs. The power supply concept of ADCs and FE-boards are shown in Table 3.

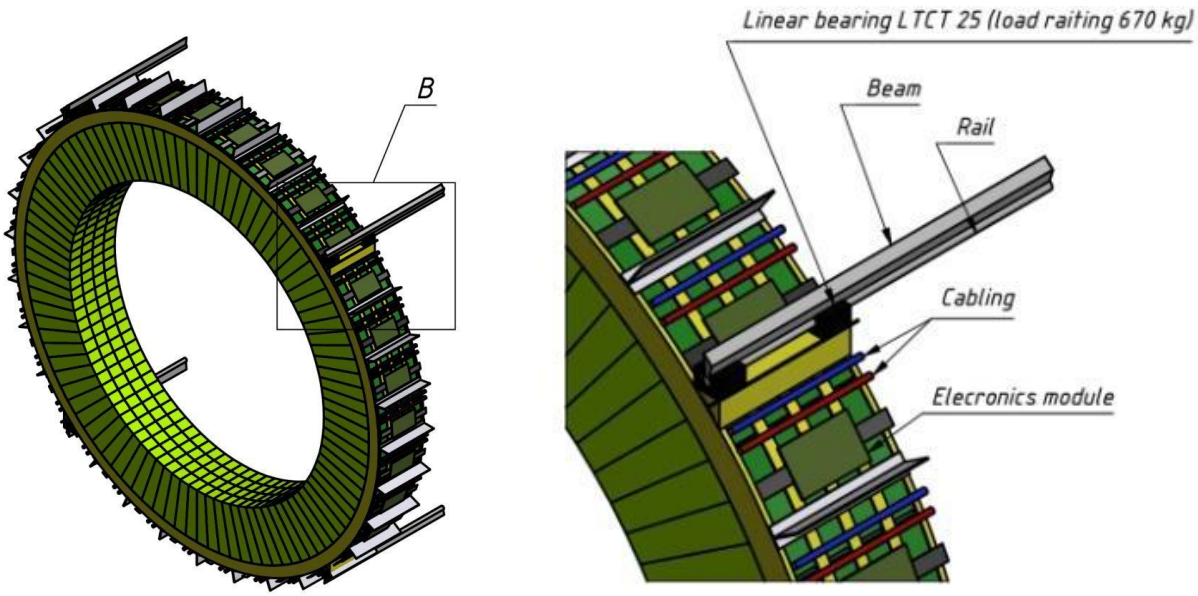

(a) (b)

Figure 4: The isometric view of one ECAL barrel ring (a) and possible supported rails are shown (b). Electronics (ADC) are located according to calorimeter clusters.

ADC and cables traces are located along the surface of the ring, as shown at Fig. 4 (b). A free space of 60-80 mm between the cryostat and the top of the calorimeter should be provided for placement of ADC and cables traces. This space is also required for the air flow that cools the ADCs. Air flow must be forced from outside of the calorimeter to avoid its overheating. The rails for fastening of the ECAL's barrel inside of the cryostat are mounted in this gap also.

2.2. **End Cup.**

Each End Cap (one is shown at Fig. 4) consists of 4608 cells, grouped by 64, forming 72 clusters. All 64 cells of each cluster are connected to 4 pcs. of 16-channel FE-boards for MPPC's bias voltage control and their readout is provided by one ADC. Total amount of ECAL's main components - ADC, FE, HV, MPPC, etc. is presented in Table 2. The cell cross-section is 40×40 mm^2 and the length is 500 mm along beam. The End Cup has absorber's length equal to 17.6 X_0. The weight of the one End Cap is 11.1 tons and for two parts is 22.2 tons correspondingly, as they are shown in Table 1. Totally, there are 9216 cells in both End Caps. There is a hole for the beam pipe in the center of each End Cap. The hole has a size of 160×160 mm^2, which is equivalent to 16 cells.

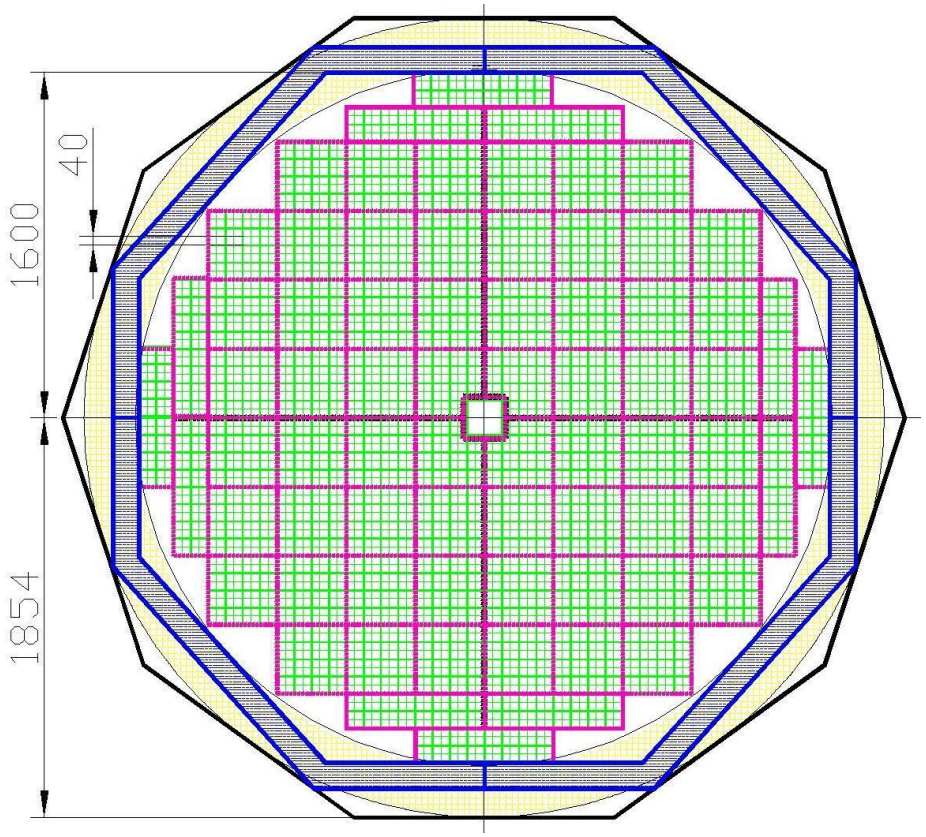

Figure 5: The End Cap part of the calorimeter in frame, installed in RS. One End Cup consists of 4608 cells with total weight 11.1 ton. The holes of size 160×160 mm^2 for the beam pipe can be seen in the centers of the End Caps. All dimensions are in millimeters.

The End Cap is mounted in the frame that supports it and shapes its geometry. The frame is installed directly on the barrel RS, as shown at Fig. 5. There is a gap about 6 cm between the End Cap of the RS and Calorimeter's End Cap for the ADCs placement and cable routes (Fig.1). This gap is also necessary for air circulation for ADC cooling.

3. Design of the calorimeter module prototype.

The first version of the module, which was described in CDR of SPD in 2020 and published in [2], had a sampling structure of 220 layers of 1.5 mm and 0.3 mm scintillator and lead respectively. This version had the absorber's length equal to 12.6X_0 and Moliere radius equal to 7.6 cm. The second (new) version of the module, which was made for testing purposes, consisted of 190 alternating layers of polystyrene scintillator and lead with a thickness of 1.5 mm and 0.5 mm, respectively. The new version of the modules with 190 layers of scintillator and lead has a shorter length along absorbed particles path (48.8 cm instead of 58 cm), but has a greater absorption quality of 17.6X0 and a smaller Moliere radius of 5.6 cm. The lead plates are intended to absorb the particle energy and develop an electromagnetic shower, whereas the scintillator plates produce an amount of light proportional to the energy of the particles. The properties of the absorber and the scintillator define the Moli`ere radius, which is equal to 5.8 cm for the selected structure [3]. The energy resolution for 1 GeV photons is assumed to depend on the calorimeter sampling fraction and is expected to be ~5% [4]. The scintillator plates are made of polystyrene beads with an added luminophore admixture of 1.5% p-Terphenyl and 0.05% POPOP (C24H16N2O2) [5,6]. It has scintillation time of about 2.5 ns and light output of 60% of anthracene, which are good results. The radiation hardness of the scintillator is sufficient for radiation doses up to about 10 MegaRad (10^5 Gray), which is important for operating the calorimeter in the radiation field of secondary particles in the vicinity of the interaction point. The luminophore admixtures re-emit the energy of excitations in polystyrene in the form of visible light. The first admixture (p-Terphenyl) emits light with a wavelength of maximum emission at 340 nm. This light is absorbed by the second admixture (POPOP) and is re-emitted into a spectrum with a wavelength of maximum emission of 420 nm, which is seen as a light of blue glow. The light from the scintillator plates is gathered using wavelength shifting fibers (WLS) [7]. Fibers of type Y-11 manufactured by KURARAY are used.

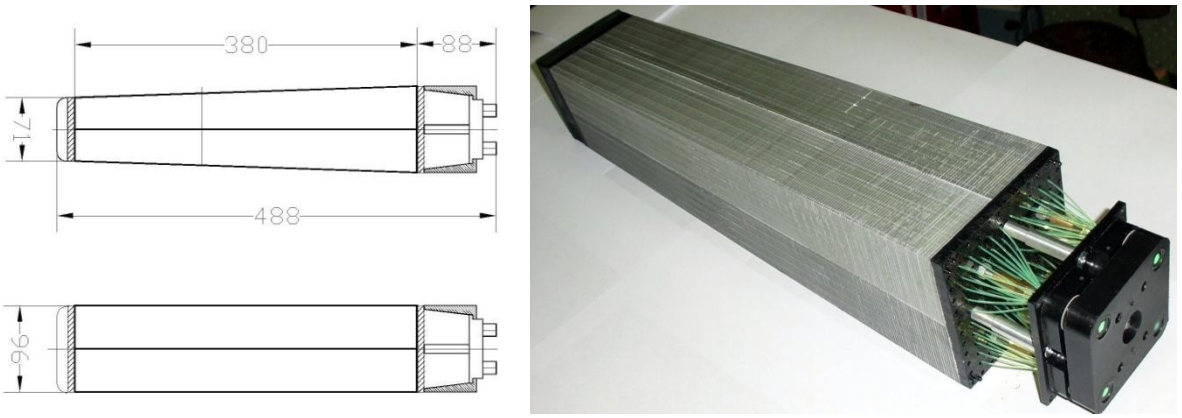

(a) (b)

Figure 6: ECAL module drawing (a) and photo (b) without light shielding cover.

The fibers absorb the light from the POPOP and re-emit it into a spectrum with a wavelength of maximum emission of 490 nm. Thirty six WLS fibers go along each cell, gather in one bundle and transmit light to one multi-pixel 6×6 mm^2 photodiode (multi-pixel photon counter, or MPPC). The schematic module drawing is shown at Fig.6 (a). The active part of the module is 380 mm and total module length is ~490 mm without MPPC board. A single module consists of 4 cells with 190 layers of the scintillator and the absorber with a thickness of 1.5 mm and 0.5 mm, respectively. Four bundles of fibers for guiding the light to the MPPC can be seen at photo in Fig.6(b). Two modules with different sampling structure are shown at Fig.7. These modules have different length due to different layers number – the first version with 220 layers and the second version with 190 layers and different absorber thickness 0.3 mm and 0.5 mm correspondingly. The shortest one (second version) has a total length, which doesn't exceed of 500 mm.

Figure 7: Two calorimeter's modules covered in light isolation paper are shown in this photo. The modules have different length due to different layers number 190 and 220 and different absorber thickness 0.5 and 0.3 mm correspondently.

4. Scintillator production.

4.1. Injection molding technology.

As it was mentioned in details in section 3, calorimeter employs polystyrene scintillator plates from Polystyrene with an added luminophore admixture of 1.5% p-Terphenyl and 0.05% POPOP (C24H16N2O2) [5,6]. Scintillation plates for calorimeter prototypes were manufactured by injection molding technology at the pilot plant of IHEP [12]. Scintillation material of this type has been successfully used in calorimeters for the last 20 years. It has a high radiation hardness (about 10^6 Rad = 10^5 Gray), a good light output (60% of anthracene), a fast decay time (1.2 ns), a high transparency for blue light (420 nm) with attenuation length ~60 cm. The injection molding technology requires a special machine (Fig.8) and matrix form (Fig.9) for scintillation plates production with given dimensions. Thermo plastic injection molding machines are a standard series of injection molding machines designed to perform most typical tasks that do not require the use of special materials or particularly high requirements for molded products. These are injection molding machines that have incorporated the most reliable, time-tested and effective solutions. The production procedure is automatic and allows production rates one cycle per ~one minute (4 tiles). Granulated Polystyrene PSM-115 [13] with dopants: 1.5% Pt-Terphenyle [5] and 0.05% POPOP [6] is used for scintillator production. All used components are pre-dried and then mixed in special mixers. Then the prepared mixture is fed into the receiver of the injection molding machine.

Figure 8: Thermo plastic injection molding machine general view.

4.2. **Matrix form.**

One of the important points is the molding press-form for the scintillator production. It should be made from high precision details of high quality materials (Fig. 9, (a)), and cost of the press-form is about 50 thousand of USA dollars. The number of molding cycles should be on the order of one million to produce 4 million plates required for the SPD calorimeter. Figures 9, (b) shows 4 pcs of scintillator plates coming out of the injection machine. Each injection cycle for

4 plates will take 1 minute. The total number of SPD calorimeter scintillator plates is about 4,000,000 pieces with a total weight of about 15 tons.

4.3. Time estimation for calorimeter modules production.

Taking into account that one injection molding machine cycle is 1 minute and with two molds run 24 hours a day - ~~a~~ totally of 583 days – are needed to produce the all required amount of the scintillator and absorber tiles. Considering 273 working days per year, production process of the tiles will take about 2 years. Assembly of calorimeter modules at the rate of 10 modules per day let one complete this process within 2.8 years, as it is shown in Table 5. To achieve the required result in order to create a calorimeter by 2030, it is necessary to manufacture components and assemble modules in parallel to each other.

(a) (b)

Figure 9: a) 4-set matrix for scintillator production; b) – The scintillation plates released from the molding machine, details of the molding system are visible.

5. Multi-pixel photodiodes.

All of the MPPC's, that are used in this prototype have the same size of 6×6 mm^2. The S13360-6025 [8] series has the best response speed, low capacitance and large number of pixels, but, the largest temperature coefficient of KT ~0.054 V/°C. The temperature coefficient represents a linear dependence of breakdown voltage on temperature. Temperature dependence of MPCC's breakdown voltage leads to MPCC's gain variation if this temperature dependence isn't compensated. To achieve calorimeter's stability of about 2%, one needs to ensure temperature stability of the surrounding environment, or use the breakdown voltage compensation scheme:

$$U_{OP}(T) = U_{BR} + \Delta U + (KT \times \Delta T),$$

where: U_{OP} and U_{BR} are MPCC's bias voltage at temperature T and MPCC's breakdown voltage at device characterization temperature, respectively. ΔU is a given over-voltage and $\Delta T=T-20°C$ is a deviation of the current temperature (T) from temperature selected by the compensation program, typically 20 °C. MPCCs of S14160-6050 series have higher photo detector efficiency, but fewer pixels, which is worse in terms of the dynamic range. This series has a small temperature coefficient. An optimal solution would be usage of MPCCs with properties similar to S13360-6025 or S14160-6050 series, but with a smaller pixel size of 15 ÷20 μm, i.e. larger amount of pixels, which would make them more suitable for the calorimeter. Four MPPC's are surface mounted on a circuit board, as it is shown at Fig.10. A thermistor is also installed on the board to measure the photodiode's temperature. The circuit board is attached to a module in such a way that the photodiodes are located exactly opposite the ends of fiber bundles. There is no optical contact between the photodiode and the WLS, there is an air gap of about 0.1 mm instead. Optical grease is not used in order to avoid instability in the conditions of light guiding. A light insulating basket made of black plastic is installed above of the circuit board.

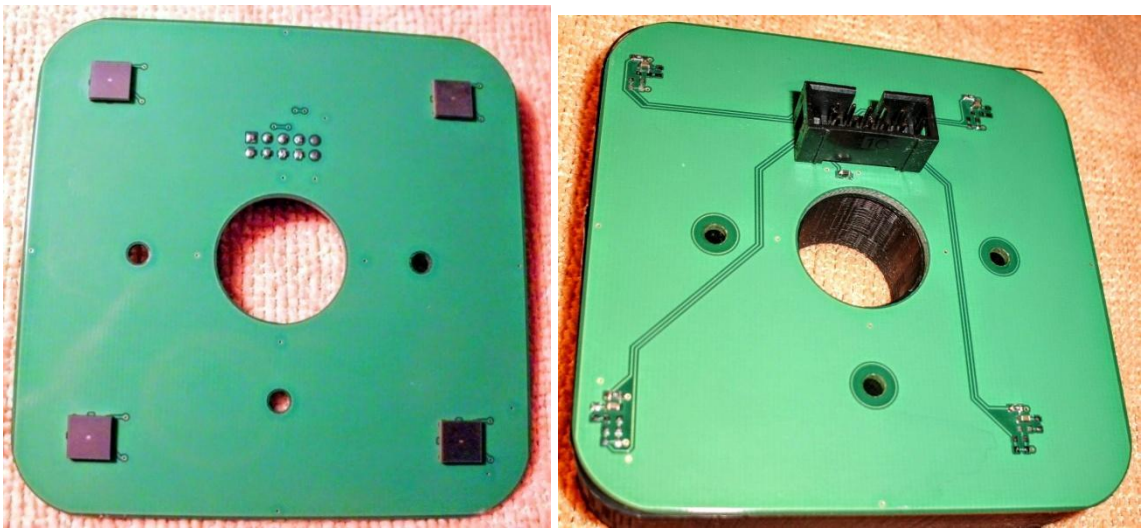

(a) (b)

Figure 10: Printed circuit board with 4 MPPC diodes: front (a) and back (b) sides.

The MPPC boards are connected to the amplifier / bias control board (FE-board) (Fig.11 (a)) with up to 1-meter of flat 5-pair twisted-pair cable. Four wires transmit signals from four MPPC's to the amplifiers of FE-board. One wire used to provide regulated common bias voltage to all MPCCs on the board (up to ~55 V) and another one to connect the thermistor for local temperature measurement of MPCCs. Output signals of each MPCC are transmitted via twisted pairs of wires (signal/GND). Small regulated individual reverse bias voltage can be applied by FE-board on signal wires of each MPCC in range from 0.0 to ~3.0 V for individual adjusting of bias voltage. Such way, the bias voltage of each MPCC can be individually and precisely trim in a small range with 10-bit precision (i.e. ~3 mV step) in order to take into account and compensate possible variations of individual parameters of each MPPCs. FE-board provides hardware control of regulated MPPC's bias voltage and also amplifies MPPC's signals and convert them to differential type, which is required by ADC board. Calculations required for bias voltage compensation with temperature are performed at a software level by control PC, taking into account the local temperature measured by the thermistor installed on MPPC's circuit board. This approach allows calorimeter operation without special measures for MPCC's temperature

stabilization. Signal stability of the order of 1.0% was achieved during measurement over an extended period of time with usage of such technique.

6. MPPC readout and high voltage control.

6.1. Analog-to-digital converter (ADC).

The readout electronics consists of an 64 channel ADC board – an analog-to-digital converter ADC-64 (Fig.11(b)). The ADC continuously performs simultaneous samples on all of 64 input channels with a fixed frequency and provides full digital representation of input signals shape in time. Samples are done at a 64-MHz frequency, which corresponds to the sampling period of 15.625 ns. Each sample is digitized with a 12-bit conversion. At present, there is an ADC-64ECal modification, which improves digitization up to 14-bit and significantly extends the dynamic range of the measured amplitudes. The new ADC-64ECal [9] modification also allows operation in strong magnetic fields, which is necessary for experiments at the NICA accelerator complex.

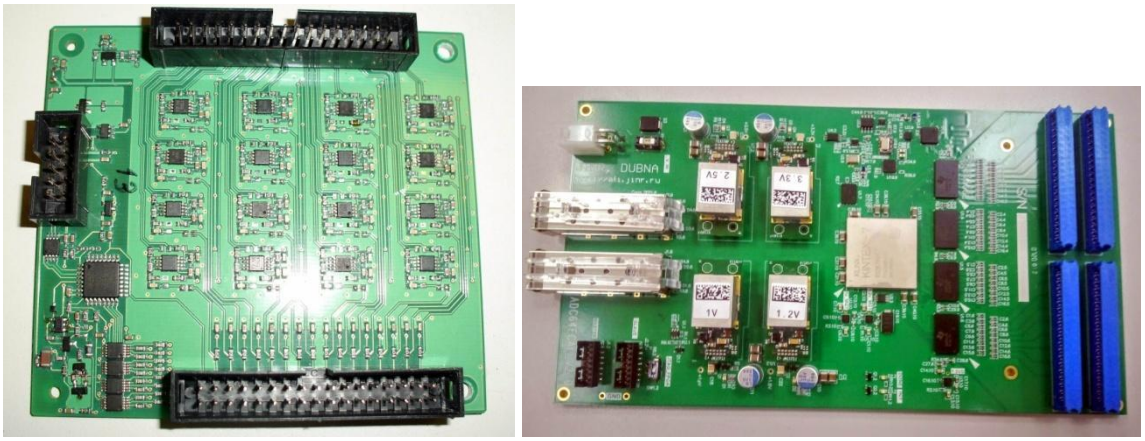

(a) (b)

Figure 11: a) – 16-channel amplifier / bias control board (FE-board),
b) – and ADC-64ECAL digitizer.

The ADC-64ECal power consumption is about 13W per one 64-channel board, i.e. ~200 mW/ch. Total ADC's power consumption shown in Table 3. It is equal 3.4 kW for Barrel and 0.9 kW for End Cap calorimeters. ADC card will be located directly on the calorimeter to reduce signal noise and reduce the cabling bundles between ADC data collector. ADC provides two Ethernet interfaces (one can see them at Fig.11 (b)), one for data transfer to higher level of data acquisition system, and another one for time synchronization (White Rabbit technology is employed), which provides sub-nanosecond accuracy. 50 Ohm coaxial input can be used as external trigger for readout synchronization. The ADC can also operate in streamer mode due to dedicated firmware.

6.2. Front End amplifier.

Front-End (FE) electronics will be located directly on the calorimeter. Small path of analog signal to FE means less signal distortion and pickup noises. FE electronics card with an 16-channels amplifier / bias control is shown in Fig.11 (a). It is used to:

- control the MPPC's bias,
- amplify MPCC's output signals,
- convert them to differential type and transmit them to analog inputs of ADCs (Fig.11(b)).

Each FE-board can service up to 4 pcs MPCC's boards (Fig.10). The FE-board and the MPPCs must be located close to each other, therefore they will be placed on the same printed circuit board. The FE-board board power has consumption is about 33 mW, i.e. ~2 mW/ch., and total their power consumption is ~1.6 kW for the whole calorimeter.

6.3. **High voltage control.**

All required power supply voltages for FE-boards (High voltage, required for MPCC's bias, and Low voltage, required for internal circuits of FE-boards) are supplied from the specially designed HV control power box [11], which is shown at Fig.12. The HV control box can provide required power supply for up to 127 pcs of FE-boards, which are connected in parallel on 10 wire flat cable. The HV control box has Ethernet control from outside. The HV control box communicates with FE-boards by RS-485 interface for MPCC's bias voltage control and temperature feedback. The flat cable length can be over 100 meters. Therefore, this box can be installed outside of the calorimeter at a distance up to 100 meters. The consumed power of this unit is up to 100 watts. Taking into account that 20 such units are needed for the calorimeter, their total consumption is up to 2 KW (Table 3).

Figure 12: Control power box (HV) for MPPC bias Voltage.

6.4. **LED generator.**

To make a precise calibration of each ECAL channel and for the continuous monitoring of channel amplification LED generator has been designed [10] and built. Main requirement to this device is its stability. Light intensity variation should be below 1%. To reach such stability and to reduce residual variations of LED light intensity the feedback loop has been implemented to

the device. The pin diode has been located on the LED back side. Light from the LED back side is detected by the pin diode and analyzed by control circuits to organize a feedback control and improve LED's stability. Light from LED front side have a high luminosity and can be distributed by optical fiber light guides to large amount of calorimeter cells. One such generator can supply light up to 100 channels with intensity about 1000 photo elections, which is enough to provide MPPC's gain control and sensitivity monitoring. This LED control system was used in test setup shown at Fig.13 for monitoring long term stability during data taking on cosmic rays.

6.5. Slow control system.

The main objectives of slow-control system (SC) are:

- Operating equipment parameters control;
- Monitoring of low and high-voltage power supplies;
- Recording of slow-control commands and data;
- Notification about problems (Alarms);
- LED signals recording for long time stability check.

High voltage (HV) has been designed especially for the MAPD based devices and is part of the slow control system. Specific points of HV are:

- Multichannel (~30 000 channels);
- Very precise voltage setting for each channel;
- Need of voltage correction depending of temperature of MAPD;
- Temperature control for ADCs boards

7. Cosmic ray test results.

7.1. Energy resolution.

A test setup was made from four calorimeter modules consisting of 16 cells with a cross-section of 55×55 mm^2 and tested then on cosmic rays. In this prototype, light detectors were based on MPCC types S13360-6025 with 25 micron pixel pitch. For testing on cosmic rays, a small setup (Fig.13) of 4 modules (each 11×11 cm^2), of the total cross-section of 22×22 cm^2, was used. The cells, each 55×55 mm^2, are assembled in a 4×4 setup. The modules are placed vertically, while the direction of the registered cosmic rays is determined by trigger counters. Trigger counters are scintillator detectors based on multi-pixel photodiodes of FC6035 type and size 6×6 mm^2. All counter's photodiodes were connected to coincidence circuit to make trigger for the ADC for cosmic rays events selection. Auxiliary trigger signals from the generator which controls the LEDs were also logically added (by "OR" function) to cosmic rays trigger signals. LED was used for control and calibration of calorimeter cells, estimations of the light yield, and for long-term stability check. Data acquisition ~~i~~was conducted ~~at~~ by the 64 channel ADC board, similar to described at 6.1 with intended software usage from the ADC developer [9]. During a data taking period of 5-6 days, statistics of the order of million events was obtained. The setup allows one to measure energy depositions and trajectories of cosmic ray particles. Relativistic muons with energy above 250 MeV pierce through the calorimeter and form a peak in the deposited energy spectrum. In order to select straight tracks of particles, which pass vertically through one module, only those events are selected, which have the number of hits equal to 1 to avoid side tracks.

Figure 13: Photo of the calorimeter test setup consisting of 4 modules of the size 11×11 cm^2, with the total cross-section of 22×22 cm^2. The environment temperature was measured by thermistors, provided for each 4 MPPCs board and by digital thermometer as well. One of the boards in light protection cover and the digital thermometer are placed on the top of the setup. The optical fibers (visible on photo in Fig.13) distribute the light from LED generator.

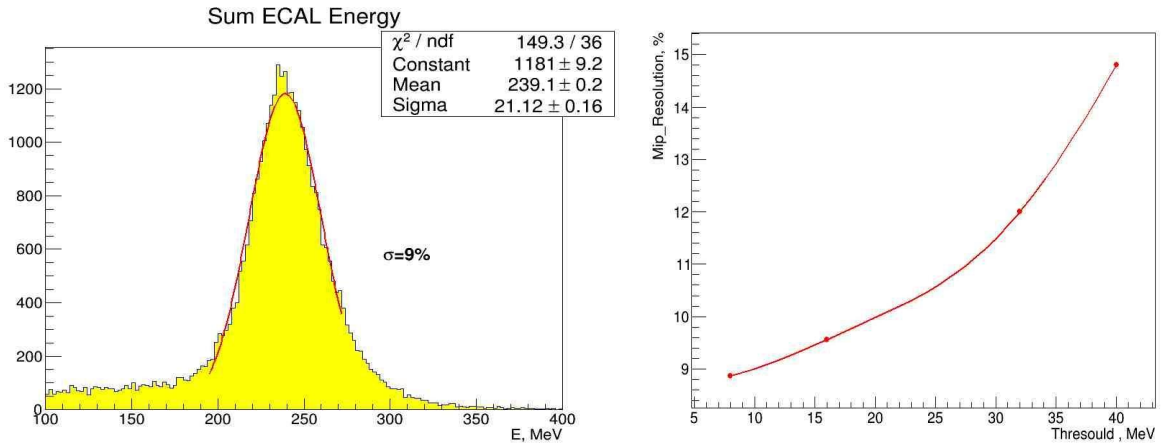

(a) (b)

Figure 14: a) –The energy spectrum of the calorimeter for vertical cosmic ray particles with energy resolution of 9%. This point corresponds to ADC's threshold ~8 MeV. b) – The energy resolution dependence on the ADC's threshold in MeV.

Signals obtained on cosmic muons were used for amplitudes alignment and calorimeter energy calibration. Only events with exactly one cell hit were selected. The bordering cells have more events with smaller amplitudes due to angled tracks. We perform calorimeter calibration using only vertical tracks. Each maximum position in terms of ADC units is mapped to the corresponding energy deposition. The energy scale is determined from the Monte-Carlo simulation as the scale factor between the energy deposition in scintillator plates for the given structure of an electron with 1-GeV energy and a relativistic muon with energy above 1 GeV. From this proportion we estimate the MIP signal in this calorimeter to be 240 MeV. This value divided by the position of the muon's peak maximum is used as a calibration coefficient for each cell. This calibration procedure involving the MIP energy deposition is not absolute or conclusive. Primarily, it aligns the gain coefficients in each cell to ensure equal response of each cell. The measured electron or photon energy can be further revised by reconstructing neutral pions or calibrating the calorimeter using electron or photon beams of known energy. The electromagnetic calorimeter measures electron or photon energy by summing up signals from all 16 cells. Each cell can only contain a fraction of energy deposited by the particle in the calorimeter (if the particle is not a relativistic muon or a MIP). The energy resolution of the calorimeter for vertical cosmic ray particles is 9.0% (Fig.14 (a)). This value corresponds to energy deposition of 240 MeV. Assuming the resolution depends on the energy as $E^{-1/2}$, the energy resolution at 1 GeV is estimated to be 5%. The energy resolution dependence on the ADC's threshold is shown in Fig.14 (b).

7.2. **Long term stability.**

Temperature dependence of calorimeter stability was estimated with usage of daily temperature variations in the range of 18-26 °C. Signals from cosmic rays particles as well as signals from LEDs of a 1-Hz frequency were captured during the measurement over 10 days. Photodiode's temperature was continuously monitored by FE-board through MPPC's board thermistor. The bias voltage on photodiodes was corrected during data capture in accordance with a measured temperature using a linear dependence:

$$U_{bias}(T) = U_{base} + K_t \times (T - 20),$$

where:
T – MPPC's board temperature, °C;
$U_{bias}(T)$ – total bias voltage applied to MPPC at temperature T, V;
U_{base} – MPPC's base voltage from power supply [11] at 20 °C.

The temperature coefficient K_t = 0.054 V/°C was used for temperature compensation of bias voltage is shown in Fig.15 (a,b), depends on MPPC type.

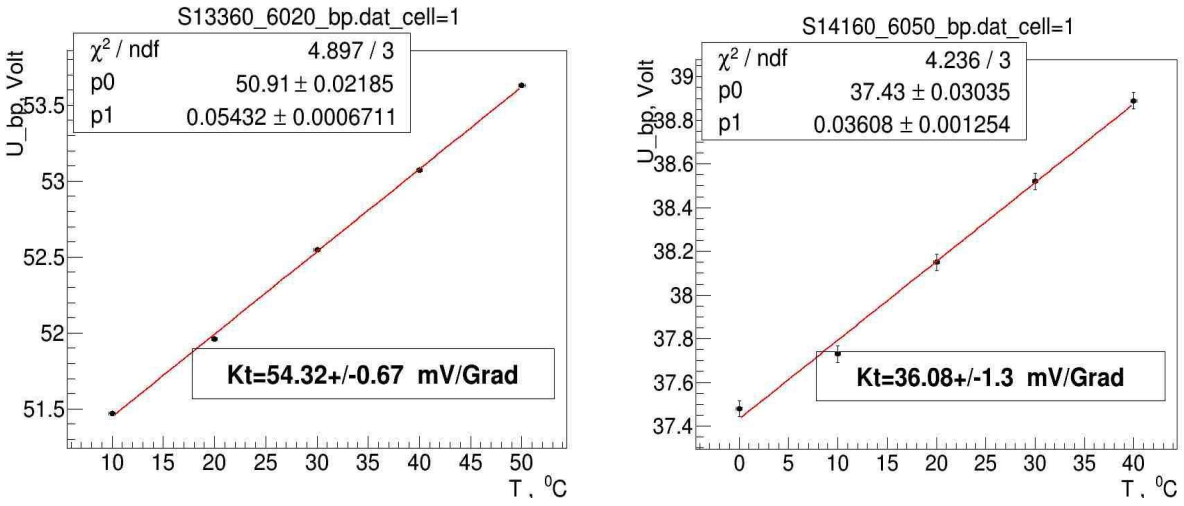

(a) (b)

Figure 15: Dependencies of MPPC break down voltage on temperature for different MPPC types: a) – for S13360-6025, b) – for S14160-6050.

The lower temperature dependence typical for diodes with a low breakdown voltage as S14160-6050. But this type of MPPC has few pixel numbers (~14000) a therefore recently new type – S14160-6015 was developed with 160000 pixels of 15 micron pixel pitch and it will be tested soon.

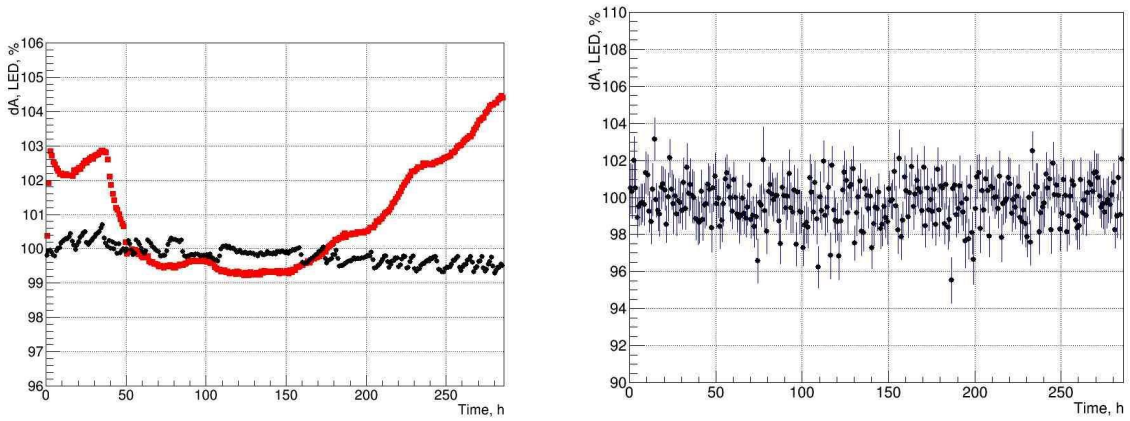

(a) (b)

Figure 16: Dependences of the sum (average value) of MPPC signals on time of measurement (in hours). a) LED signals with temperature-dependent bias voltage compensation (black) and ones without compensation (read). b) – MIP signals with temperature-dependent bias voltage compensation.

Dependences of the calorimeter signals on the measurement time are shown at Fig.16 (a,b). These data are presented in % with respect to the first 5 minutes of the measurement period for normalization. The temperature variations during the measurement were about +/-4°C. After compensation was employed, daily variations in the MPPC's signal amplitude were constrained within ±0.5%. The calorimeter can operate with a stability of ~1.0% during time over 10 days if the temperature compensation of the operating voltage is maintained, as it can be seen from these results and is shown in Fig.16 (b).

8. Cost estimation and the time scale.

The cost of the calorimeter is proportional to the number of channels. Mechanical assembly of a calorimeter cell from the scintillator and the lead plates costs 100$ per channel. Another expensive element is the wavelength shifting fibers. For a 40×40 mm2 cell, 16 fibers of the total length of 8 m are used. Assuming an average price of 4$/m, the price per channel amounts to 50$. The cost of photodiodes depends on the quantity. For purchases of tens of thousands of units, their price is about 50$ per unit. The electronics also contributes significantly to the total cost, especially the ADC with a price of 52$ per channel. The cost of the supply and voltage control systems is 28$ per channel. The total cost of a calorimeter cell is about 355$. Thus, total cost of a 26112-cell calorimeter is 9.272 M$, as it is shown in Table 4. Starting from 2022 with Technical Design progress we need, at first, to prepare the technical documentation with drawings of calorimeter details. Then we can start production operations. The readout front-end electronics should be corresponded to data acquisition system. It should have low power consumption and high rate of data acquisition. For these new electronic base should be used to achieve these goals.

The work schedule for the calorimeter from 2022 to 2030 is shown in Table 6.

9. Tables

Table 1. The weight distribution for ECAL parts. The column 2, 3 relate to absorber (lead) and scintillator in single cell; 4 – single cell weigh in kg; 5-7 – Lead and Scintillator contribution in ton. Total*) - the total weigh of calorimeter main parts, supported mechanical frame is taken into account also

1	2	3	4	5	6	7
Material	**Lead**	**Scint**	**Cell**	**Lead**	**Scint**	**Total*)**
Units	kg	kg	kg	ton	ton	**ton**
Barel	2,07	0,56	2,63	34,98	9,52	**46**
End Cup-2	1,73	0,68	2,40	7,95	3,12	**12**
End Cup-2	1,73	0,68	2,40	7,95	3,12	**12**

Total	5,52	1,92	7,44	50,88	15,76	**70**

Table 2. Number of main ECAL components: 2 – number of calorimeter cells, 3 – number of 64-channel ADC boards, 4 – number of 16-channel front-end boards (FE-board), 5 – number of HV power control units, 6 – number of MPPC , 7 - length of WLS fiber in meters.

1	2	3	4	5	6	7
Item	**N cells**	**ADC64E**	**FE**	**HV**	**MPPC**	**Fiber, m**
Barel	16896	264	1 056	12	16 896	135168
End Cup-2	4608	72	288	4	4 608	36864
End Cup-2	4608	72	288	4	4 608	36864
Total	**26112**	**408**	**1 632**	**20**	**26 112**	**208896**

Table 3. Power consumption of the **ECAL** in kW for: 2 - ADC [9] , 3 – FE-boards [8], 4 – HV power units [8], 5 – total in kW.

1	2	3	4	5
Item	**ADC**	**FE**	**HV**	Total
mW/ch	200	63	1,2	264
Barrel	3,4	1,1	1,2	5,6
End Cup-2	0,9	0,3	0,4	1,6
End Cup-2	0,9	0,3	0,4	1,6
Total	**5,2**	**1,6**	**2,0**	**8,9**

Table 4. The Calorimeter cost estimation. EC_1 and EC_2 – the End Cup calorimeters cost. The cost per channel of various calorimeter components, USD, is shown in bottom line.
The cost of assembling of calorimeter modules and manufacturing of the supporting mechanical frame is estimated in columns 6 and 7.

1	2	3	4	5	6	7	8	9	10	11	12
Item	**N_cells**	**ADC**	**FE**	**HV**	**Assembl.**	**Frame**	**MPPC**	**Fiber**	**Lead**	**Scint**	**Total**
Barrel	16896	880	451	10	1 690	85	845	845	887	229	**5 921**
EC_1	4608	240	123	2	461	85	230	230	242	62	**1 676**
EC_2	4608	240	123	2	461	85	230	230	242	62	**1 676**
Total	26112	**1 360**	**696**	**14**	**2 611**	**256**	**1 306**	**1 306**	**1 370**	**353**	**9 272**

USD/ch	355	52	27	1	100	10	50	50	52	14	355

Table 5. ECAL components manufacturing time estimation. 2 – number of cells; 3*, 4* – time of scintillator and lead plates production, days; 5 – time of calorimeter modules assembling, days, at estimated production rate 10 modules/day; 6 – total required time for calorimeter main part production, years. *) - tasks in columns 3 and 4 must be carried out in parallel.

1	2	3*	4*	5	6
Items	**Num.**	**Scint.**	**Lead**	**Assemb.**	**Year**
Barrel	16896	**279**	279	**422**	**1,8**
End Cup-2	4608	**152**	152	**115**	**0,5**
End Cup-2	4608	**152**	152	**115**	**0,5**
Total	26112	**583**	**583**	**653**	**2,8**

Table 6. The ECAL time scale starting from 2022 to 2031 to be commissioned and ready for installation in SPD hall for data taking with beam.

Items	**2021**	**2022**	**2023**	**2024**	**2025**	**2026**	**2027**	**2028**	**2029**	**2030**
Task Name										
Infrastructure										
Design Frame										
Frame production										
Cooling System										
Slow Control										
FE R&D										
FE, ADC Production										
WLS purchase										
MPPC purchase										
Modules R&D										
Scintillator.Product.										
Mod. Assembling										
Modules Testig										
ECAL installation										
Comissioning										

10. References.

[1] CDR SPD: http://spd.jinr.ru/wp-content/uploads/2021/04/2102.00442.pdf

[2] Simulation Studies of the Moliere Radius for EM Calorimeter. O. P. Gavrishchuk, V.E. Kovtun, T.V. Malykhina Materials XXVII INTERNATIONAL CONFERENCE ON CHARGED PARTICLES

[3] ECAL: Electromagnetic calorimeter for the SPD experiment. V. N. Azorskyi, N. O. Graphov, O. P. Gavrischuk * , A. I. Maltsev **, V. V. Tereshenko (JINR, Dubna). Physics of elementary particles and the atomic nucleus: 2021. V. 52., Vol. 4.P. 975
[4] Simulation Study of Energy Resolution of the Electromagnetic Shashlyk Calorimeter for Different of Layers and Absorber Combinations. East European Journal of Physics. No. 3 (2020), Gavrishchuk, O.P. (JINR, Dubna); Kovtun, V.E. , Malykhina, T.V. (Karazin Kharkiv National University, Ukraine)
[5] p-Terphenil http://omlc.ogi.edu/spectra/PhotochemCAD/html/003.html
[6] POPOP http://omlc.ogi.edu/spectra/PhotochemCAD/html/077.html
[7] WLS http://kuraraypsf.jp/psf/ws.html
[8] https://www.hamamatsu.com/eu/en/product/optical-sensors/mppc/index.html
[9] ADC-64E http://afi.jinr.ru/ADC64s , https://afi-project.jinr.ru/projects/adc64ecal/wiki/index
[10] http://hvsys.ru/
[11] http://hvsys.ru/images/data/news/3_small_1368802865.pdf
[12] http://exwww.ihep.su/scint/index-e.htm
[13] PSM-115 http://www.newchemistry.ru/material.php?id=12

1. Introduction

This Technical Design Report is devoted to the detailed description of the Range (muon) System being designed for the Spin Physics Detector (SPD) at NICA [1]. The Range System of the SPD detector serves for the following purposes: (i) identification of muons in presence of a remarkable hadronic background and (ii) estimation of hadronic energy (coarse hadron calorimetry). It is important to stress that the system is the only device in the SPD setup, which can identify neutrons (by combining its signals with the electromagnetic calorimeter and the inner trackers). Muon identification (PID) is performed via muonic pattern recognition and further matching of the track segments to the tracks inside the magnets. The precise muon momentum definition is performed by the inner trackers in the magnetic field. The Mini Drift Tubes [404, 405] are used in the Range System as tracking detectors providing two-coordinate readout (wires and strips running perpendicularly). Such readout is mostly needed for the events with high track multiplicity and also for the reconstruction of the neutron space angle.

As for the design and construction of the present system, we assume to capitalize on the experience gained by the JINR group in the development of the PANDA (FAIR, Darmstadt) Muon System [406]. These two systems (PANDA and SPD), dealing with muons of comparable momentum ranges and solving the same PID tasks, should look very similar in their design and instrumentation.

2. System layout

The Range System serves as an absorber for hadrons and a ‘filter’ for muons. It also forms the magnet yoke. It consists of a barrel and two end-caps. Each end-cap, in its turn, consists of an end-cap disk and a plug. The schematic 3D view of the system and its main sizes are shown in Fig.4.25 (a). The absorber structure is shown in Fig.4.25 (b). The outer 60-mm Fe layers are used for bolting the modules together, for attachment internal detectors (inside) and external service devices (outside). The interlayer gaps of 35 mm are taken for reliable mounting of the detecting layers comprising the MDTs proper, the strip boards and the front-end electronic boards on them. The 30-mm thickness of the main absorber plates is selected as comparable with muon straggling in steel, thus giving the best possible muon-to-pion separation, and also providing rather good sampling for hadron calorimetry.

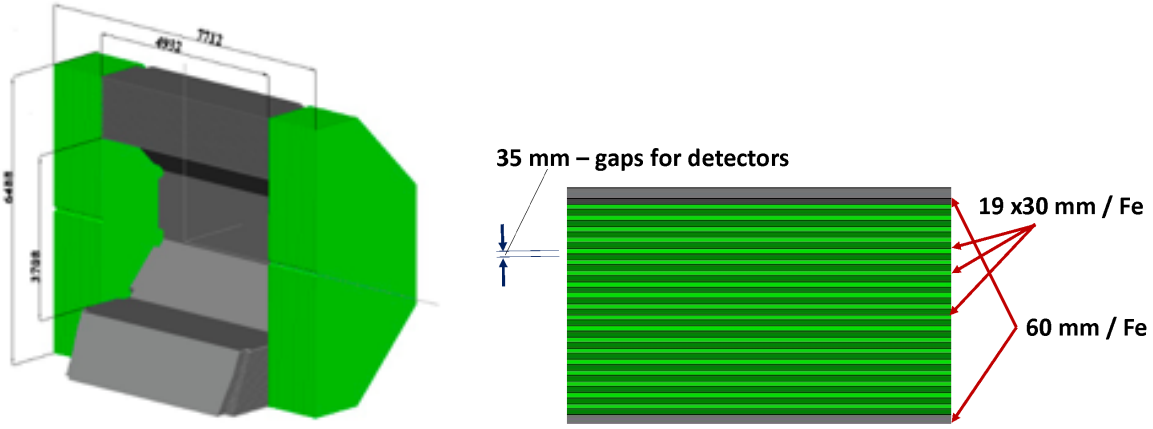

(a) (b)

Figure 4.25: 3D view (half cut) of the Range (muon) system: (a) Barrel is shown in grey, End Cap Disks − in green, and End Cap Plugs − in yellow; (b) absorber structure.

The Barrel consists of eight modules, and each end-cap disk consists of two halves divided vertically.

Such subdivision of the system (14 pieces in total) is chosen to optimize its further assembly and to satisfy the constructional requirements of the SPD experimental hall (cranes capability and floor load). The total weight of the system is about 810 tons, including 30 tons of detectors. The total number of MDT detectors is about 8000 units. The MDTs are deployed in the following way: along the beam direction in the Barrel, and perpendicular to the beam (horizontally) in the end-caps.

The absorption thicknesses of the barrel and end-caps are selected to be equal to 4 nuclear interaction lengths (λ_I) each. It provides uniform muon filtering in all directions. Together with the thickness of the electromagnetic calorimeter (~$0.5\lambda_I$) the total thickness of the SPD setup is about 4.5 λ_I.

3. Mini drift tubes detector

The Mini Drift Tubes (MDT) detector was initially developed and produced at JINR for the Muon System of the D0 experiment at FNAL [407]. Later on, an MDT-based muon system was also produced for the COMPASS experiment at CERN [408]. Developed two-coordinate readout modification of the MDT with open cathode geometry and external pickup electrodes was proposed to and accepted by the PANDA collaboration at FAIR for the muon system of their experimental setup. This new version of the MDT is proposed for the SPD project, as it has all the necessary features – radiation hardness, coordinate resolution and accuracy, time resolution, robustness, as well as advanced level of already conducted R&D within the PANDA project.

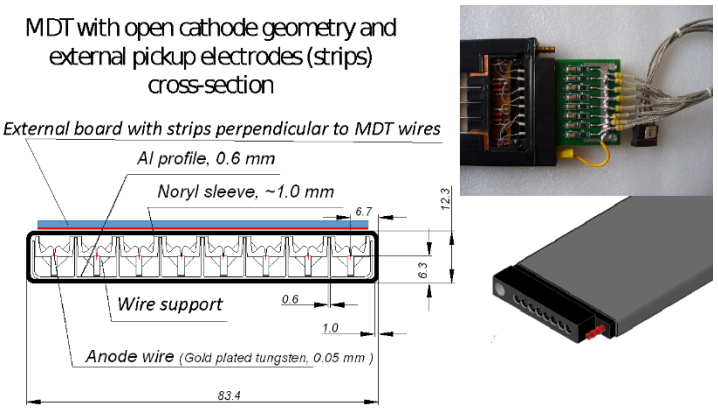

Figure 4.26: Mini Drift Tube with open cathode geometry cross-section (left) and layout (right).

The cross-section and layout of the MDT with open cathode geometry are shown in Fig.4.26. The detec- tor consists of a metallic cathode (aluminum extruded comb-like 8-cell profile), anode wires with plastic supports, and a Noryl envelope for gas tightness. The comb-like profile of the cathode provides each wire with an opening left uncovered to induce wire signals on the external electrodes (strips) perpendicular to the wires. The strips are applied to obtain the second coordinate readout. The shape of the induced signal repeats the initial one, having the opposite polarity, but the amplitude is about 15% of the wire signal (see Fig.4.27). Thus, the strip signal readout requires higher signal amplification and proper electromagnetic shielding.

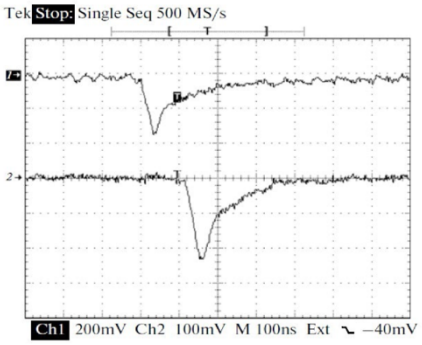

Figure 4.27: Oscillograms of single signals: from the anode wire (1) and the strip (2, inverted); the conversion factors are 60 and 480 mV/μA, respectively.

Application of an open cathode leads to the loss of the electric field symmetry in each of the 8 detec- tor cells, resulting in lower gas gain for the applied voltage comparing to the standard MDT (cathode openings closed with stainless steel lid). The conducted R&D proved that the MDT with open cathode geometry easily achieves the parameters of the one with a closed cathode at higher voltages. The com- parative plots of the counting rate, efficiency, and gas gain for both detector types (see Fig.4.28) show that the MDT with open cathode geometry repeats the standard MDT performance at a high voltage shift of +100 V. The drift time and the amplitude spectra of both detector variants also match, if we set this voltage shift between their operating points.

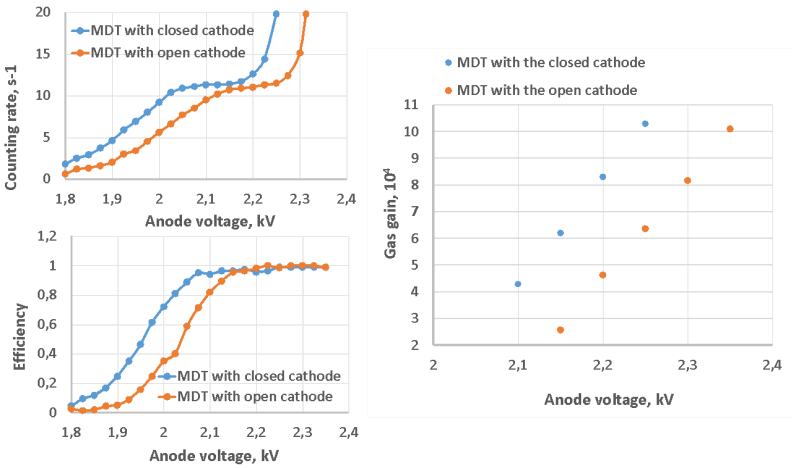

Figure 4.28: Comparative plots of the counting rate, efficiency, and gas gain versus the supply voltage for the MDT with closed and open cathode geometry.

According to the results of the MDT (open cathode geometry) ageing tests, accumulation of a 1 C/cm total charge does not produce any significant effect on the detector performance. To monitor the ageing effects, measurements of the counting rate curves (Co-60 source) together with oscilloscopic observa- tions of the MDT average signals (256 events) for Co-60 and X-rays were made twice a week over the whole period of intense irradiation (see Fig.4.29). Later on, this measurement (with X-rays) was con- ducted up to 3.5 C/cm of irradiation without any visible degradation of the MDT performance. It should ensure stable MDTs performance for the lifetime of the SPD project.

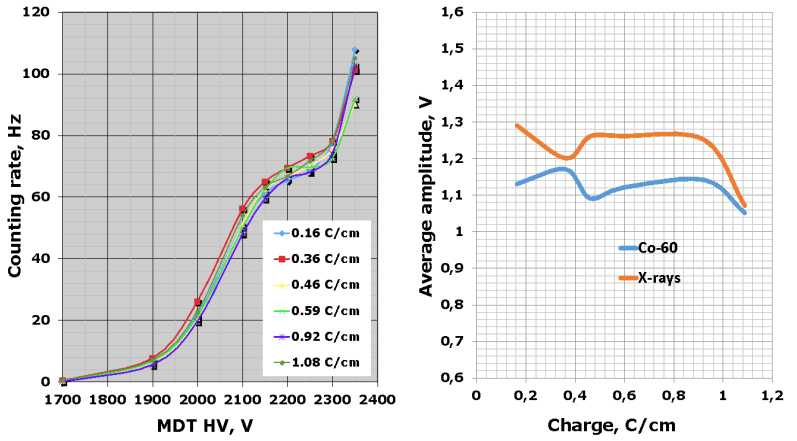

Figure 4.29: Counting rate curves for different accumulated charges (0.16÷1.08 C/cm) (left); average wire signal amplitudes vs accumulated charge for Co-60 and X-ray sources (right).

All R&D studies were made with a gas mixture of 70% Ar + 30% CO2 at atmospheric pressure, the one to be used in the proposed SPD Muon System. It is inflammable, radiation hard and fast enough (150-200 ns drift time). The wire pitch in the present design equals 1 cm, and a 3-cm strip width is selected for the second coordinate. These spatial parameters provide the Range System with coordinate accuracy well enough for identification of muons and give the system the features of a digital hadron calorimeter.

4. Analog front-end electronics

We plan to use the analog front-end electronics (with probable minor modifications) developed for the D0/FNAL and COMPASS/CERN experiments and also accepted by PANDA/FAIR. It is based on two ASIC chips: 8-channel amplifier Ampl-8.3 [409] and 8-channel comparator/discriminator Disc-8.3 [410].
The HVS/A-8 card serves for two purposes – as MDT high voltage distributor and a signal amplifier designed to be the first stage of the Barrel and the End Cap Plugs wire signal readout. It is followed by Disc-8.3 based discriminating electronics (design in process) to fulfill the readout.
The ADB-32 card (initially designed for D0/FNAL) [411] is used for the End Cap Disks wire readout.
It amplifies and discriminates the MDT signal, shaping it to the LVDS standard for further treatment by the digital front-end electronics.
An A-32 preamplifier card is used to start the strip signal readout in the whole system. It should be terminated (similarly to wire readout) by Disc-8.3-based discriminating electronics. In case of the End Cap Disks an ADB-32 card will be used for this purpose.
The view of the basic FEE cards is shown in Fig.4.30.
Totally, the Range System has 106000 readout channels (65000 of which are wires and 41000 strips).
After having been shaped to the LVDS standard, the signals from the analog electronics go to the digital front-end electronics for further treatment.

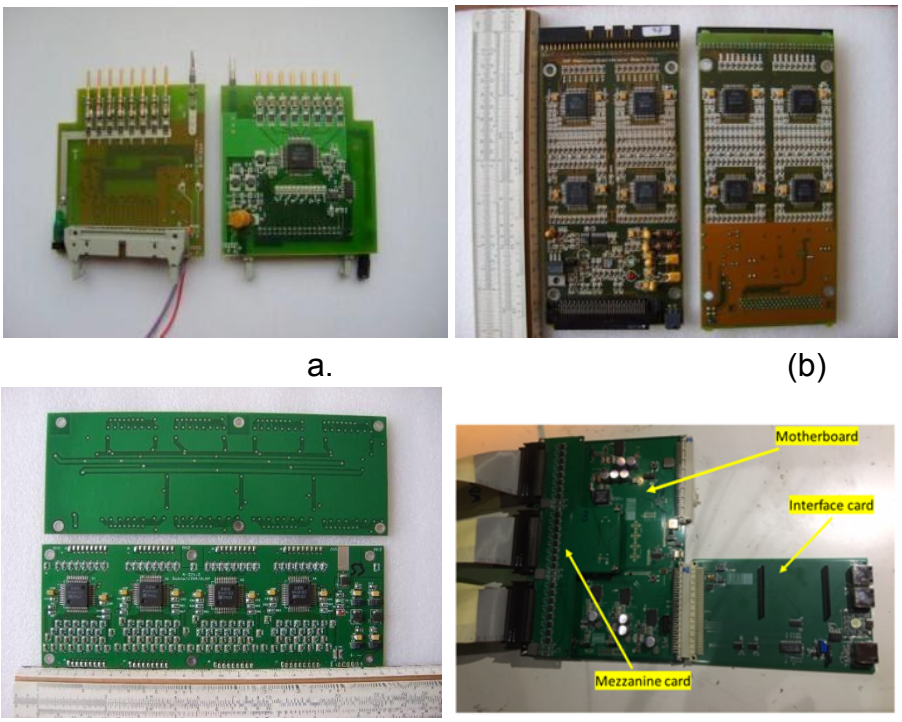

Figure 4.30: Front-end analog electronics cards: HVS/A-8 (a), ADB-32 (b) and A-32 (c). (d) Digital 192-channel MFDM module (Readout unit MFDM).

4.1. Ampl-8.51 – low input impedance amplifier for the Muon system wire and strip readout

As mentioned above, all present analog FEE designed for the Muon system use Ampl-8.3 to read both wire and strip signals. The amplifier ASIC was specially designed for MDT, but also managed to cope with strip signals when used in the two-stage circuit. Generally, Ampl-8.3 meets well strip readout requirements, but not perfectly. In terms of the set strip board parameters, value of the strip wave impedance varies in range of Rz ~ 10 ÷ 30 Ohm, but Ampl-8.3 has a 50 Ohm input impedance. The present impedance mismatch does not seem significant, but anyway matching is preferred, especially for long strip signal readout. Moreover, it would be much better to have an input impedance less than 10 Ohm, so that after matching the wave impedance of the strip (or wire) with the input impedance of the amplifier, carried out using a series-connected resistor Rd, the maximum value of the high-voltage surge is reduced by the resulting voltage divider in (Rd + Rin) / Rin times, increasing the amplifier's resistance to high-voltage breakdown increasing its lifetime and reliability. In addition, the low input impedance of the amplifier reduces external pickup at its input, which increases its immunity to self-excitation and external interference. Low or absent accessibility of strip and wire readout electronics of the range system barrel part makes a real demand for increased reliability of the amplifiers. Following the given considerations, it was decided to develop a low input impedance modification of Ampl-8.3 that would keep all proven virtues of its predecessor.

The new amplifier chip design was carried out under the following guidance:

1) the amplifier general parameters should correspond the ones of Ampl-8.3 (or close);

2) an input stage should be made as a common base npn to provide low input resistance;

3) amplifier inputs should be protected by diodes against HV pulses (both negative and positive);

4) input Rush amplifier circuit should be followed by differential amplifying stages to minimize cross-talks;

5) the amplifier should belong to trans-resistance type, it should not have a common feedback to exclude possibility of parasitic generation by excluding stray capacitances and resistors of the feedback integrated capacitors and resistors between the input and output of the amplifier;

6)maximum layout symmetry to minimize DC voltage shift at the amplifier's differential outputs at a quiescent mode.

As a result, an Ampl-8.51 circuit has been developed to meet all requested parameters. Amplifier circuit design together with spice simulations have been done using Cadence 6 CAD software. General parameters of the Ampl-8.51 spice model are presented in Table 1. All parameters are given taking into account the technological spread of the circuit elements values. For resistors, it is ± 20% of the nominal values. The Rush cascade cannot be implemented in an integral design with a small scatter of parameters, since they are determined not only by the ratio of the resistors, but also by their nominal values. The spread of the main parameters of the ASIC Ampl-8.51 will repeat the technological spread of the resistor values.

Table 4.1 Ampl-8.51 general parameters (spice simulation)

Parameter	Value
Input impedance for signal bandwidth: 1 MHz, Ohm 10 MHz, Ohm 30 MHz, Ohm	 0,25 0,9÷2,2 3,32÷8,7
Input signal polarity	±
Input ± overvoltage protection:	Yes
Differential output	Yes
Gain, mV/μA	100÷150
DC output offset voltage, V	<1,0
Output load, W	1000
Output signal leading/trailing edge (0.1 ¸ 0.9), ns	8÷12
I_{noise} for detector capacitance: *CD = 0,* r.m.s. nA *CD* = 40 pF, r.m.s. nA *CD* = 1800 pF r.m.s. nA *CD* = 5000 pF r.m.s. nA	 63÷110 96 315 572
Dynamic range for signals of both polarities, dB	48

Channel-to-channel cross-talk, dB	<–40
Voltage supply, V	± (2,8÷3,2)
Dissipated power at ±3 V supply, mW/channel	64
Channels per chip	8

The oscillograms of the Ampl-8.51 output signals within the boundaries of the technological spread of the circuit elements parameters are shown in Figure 4.1 - the simulation is performed for the so-called fast, typical and slow models of circuit elements. In these figures, fast models are represented by brown lines, typical models - by green lines, and slow models - by red lines.

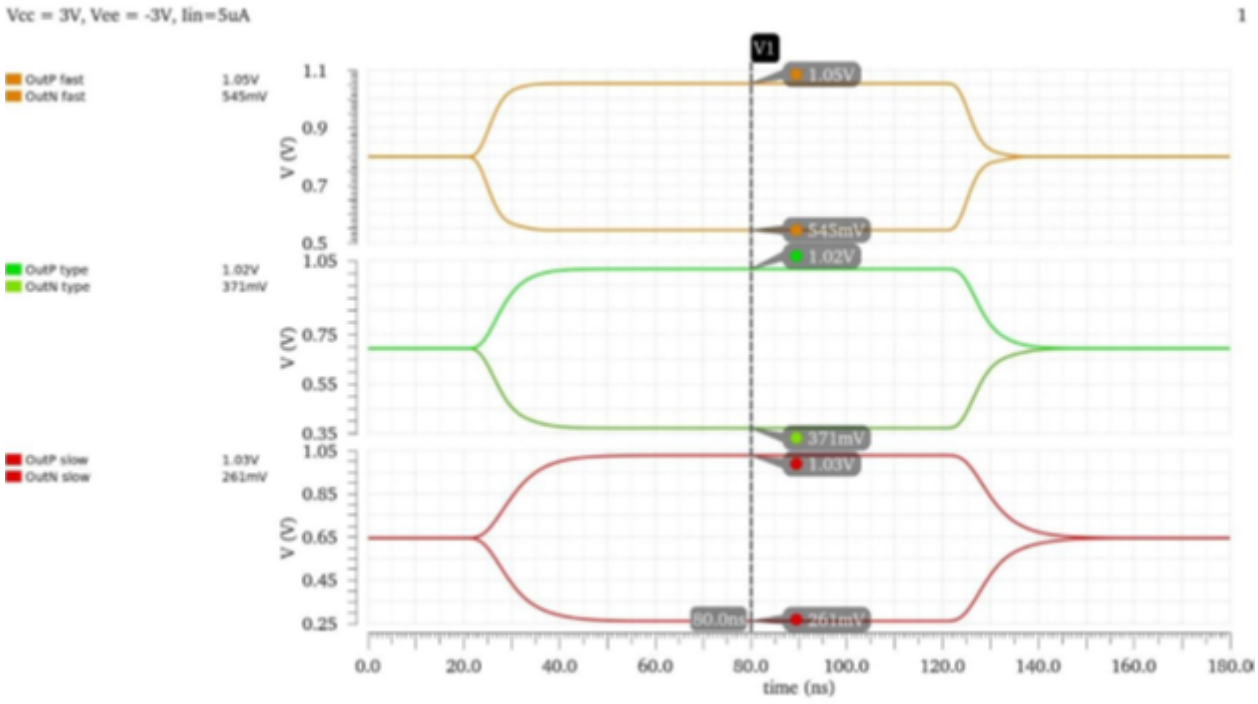

Fig.4.1 Ampl-8.51 output signals, Iin=5 μA

Figure 4.2 presents the plots of Ampl-8.51 input impedance frequency response. At a frequency of 30 MHz, the value of the input resistance will vary within 3.32 ÷ 8.7 Ohm due to technological spread in the values of the circuit elements. At a frequency of 10 MHz, the value of the input impedance remains within 0.9 ÷ 2.2 Ohm, and at low frequencies it does not exceed 0.25 Ohm.

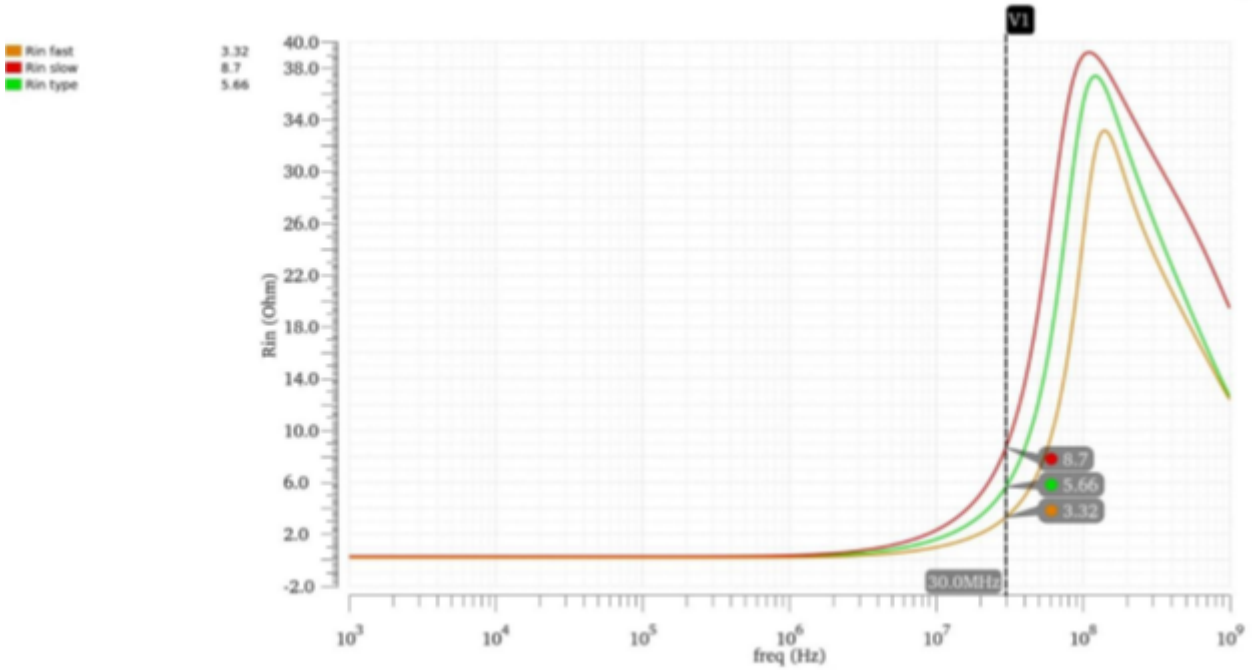

Fig.4.2 Ampl-8.51 input impedance frequency response

The presented simulation results of the Ampl-8.51 with the Rush cascade show that the main parameters of the developed integrated circuits correspond to the requirements of the technical specifications for typical values of the parameters of the circuit elements and retain the operating values within the technological spread of the circuit elements parameters.

Topology of the Ampl-8.51 and the AISIC itself have been made using the BJT-JFET technology by the Research & Production Corporation “Integral” (Minsk, Belarus).

First tests of the manufactured chip showed that this iteration has two general problems - low operating stability (self-excitations) and imbalance of differential output offset. According to preliminary examination these problems are due to the following mistakes in microchip topology (circuit peculiarities were not taken into account):

- inadequate power bus and traces width (R≠0, V drop)

- series power connections (not star type) in the circuit parts most sensitive to power

- complimentary parts of diff. circuit powered from different power bus points (operation point floats)

- the same power bus for input current amplifier and following diff. amplifier, power traces are mixed (input senses current jerks of output circuit -> self-excitations)

- common input ground (input amps’ sense neighbors -> self-excitations)

To minimize described negative effects 1st and 8th amplifier channels were disconnected from common ground and power bus (applied to 4 chips). Separated channels restore output baseline and operate without self-excitations, giving a chance to check general amplifier parameters. General parameters of Ampl-8.51 individual channels were measured, and its ability to provide strip signal readout was checked, test stand is shown in Fig. 4.3.

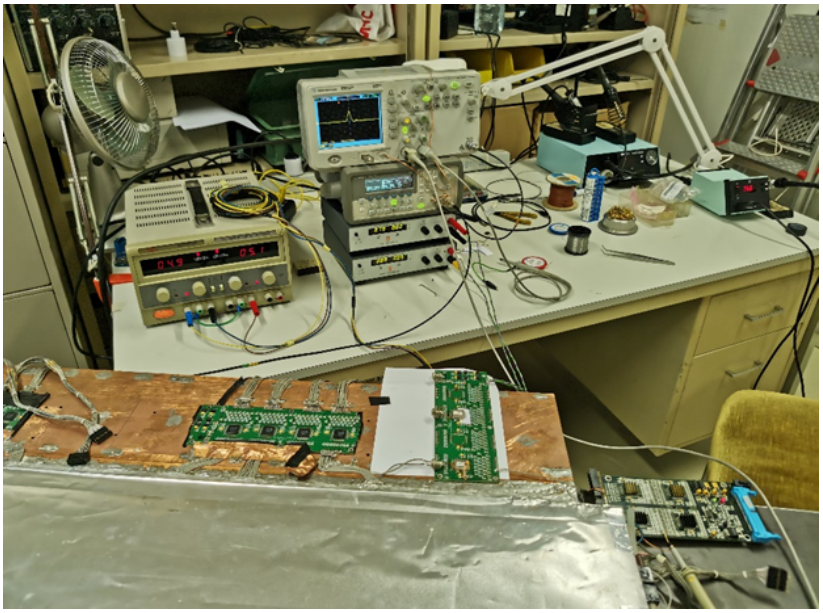

Fig. 4.2 Ampl-8.51 single channel tests.

Measured single channel parameters (see table 4.2) perfectly match the technical request.

Anyway, we still need to achieve a combined 8channel stable operation of the amplifier. We will try to apply all possible necessary corrections to metal layers of existing chips (with unfinished metallization) to fulfill the task.

Table 4.2 Ampl-8.51 single channel parameters

Input impedance (30MHz)	**5,4 Ohm**
Gain	**131 mV/μA**
Rise time/fall time	**9,2 ns**
Inoise (CD= 1,8nF)	**550 nA**
Dynamic range (CD= 0nF)	**~ 47 dB**
Dissipated power	**63 mW/ch**

5. Digital front-end electronics

The digital electronics being created for the Muon System is based on the use of FPGA chips. The prototype of the digital 192-channel MFDM module (see Fig. 4.30 (d)) (Muon FPGA Digital Module) that we have developed includes a XC7A200T chip of the Xilinx Artix 7 family. This unit is functionally, mechanically, in data format and DAQ interface, compatible with the previously developed MWDB (Muon Wall Digital Board) unit [412] made on the basis of TDC F1 (ASIC) and successfully used for data readout from the Muon System of the COMPASS experiment (CERN). This approach allows both types of units to be used in the same readout system, thus making it possible for the new MFDBs cards to be tested under actual operating conditions.
The MFDM unit is made in the VME standard (6U, 2M) with the following technical parameters:

- the number of registered channels - 192;
- input signals levels - LVDS;
- discrimination of input signals from the detector is carried out in the range of (0 ÷ +3V);
- the unit operates in the latch mode;
- the maximum time interval for digitizing input signals ~ 9 μs;
- discreteness of digitizing the time interval (bin size) - (4-5) ns;
- the unit is connected to the data acquisition system (DAQ) via the HotLink interface;
- data transfer from the module to the DAQ starts with an external Trigger signal.

The unit includes three electronic boards (Fig.4.31): motherboard, mezzanine card, and interface card. The motherboard accepts 96 LVDS signals from the analog electronics through 3 high-density connec- tors, converts them to LVTTL levels and writes to the FPGA, and also communicates with two other boards. The mezzanine card also accepts 96 LVDS signals through 3 connectors, converts them to LVTTL levels and transmits through the 120-pin board-to-board connector to the motherboard. The in- terface card is designed to connect the MFDM module with the DAQ via the HotLink interface (RJ45 connector), to download the firmware to the FPGA from a local computer, as well as to download the firmware via the RS-485 interface (RJ45 connector) from a remote computer. Interface card is installed from the backside of the VME crate through the P2 connector.

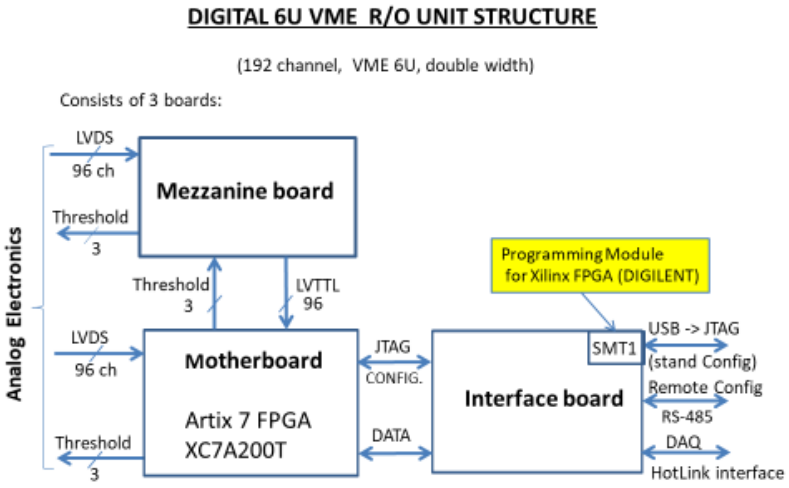

Figure 4.31: Block-diagram of the MFDM module.

Tests of the MFDM unit performed at CERN with the Muon System prototype (250 MDT detectors, 4000 readout channels), on cosmic gave encourage results. Fig. 3 shows the structure of a stand-alone data acquisition system is based on GeSIca and a multiplexer (MUX) units from COMPASS DAQ, in which two MWDBs (F1 TDC / ASIC) were replaced by two MFDM modules (FPGA) in order to verify performance the latter.

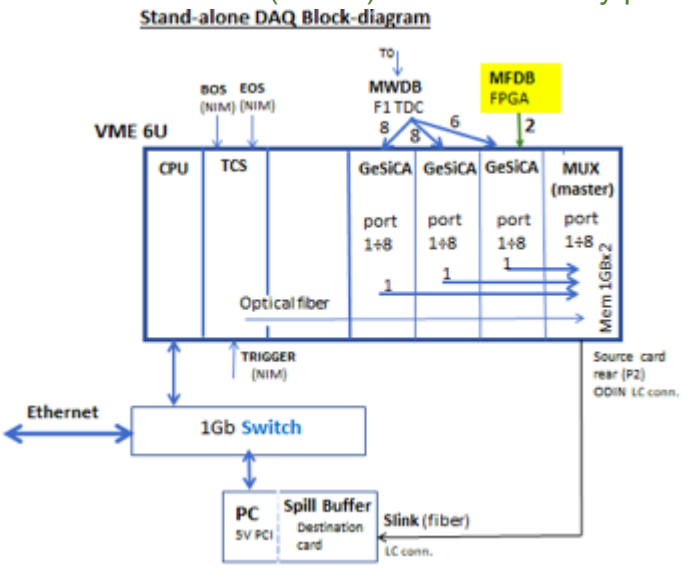

Fig. 3 Stand-alone readout system

Figure 4 displays tracks and time spectra obtained from the tests, using only MWDB (F1 TDC) units (a) in one case, and two MFDMs (FPGA) (b) instead of two MWDBs (planes # 17,18) in the other. In both cases, the obtained results were the same - in planes # 17,18 the triggered wires are in correct position on the track, the time spectra

also coincide with small deviations due to the peculiarities of TDC F1 operation in the latch mode.

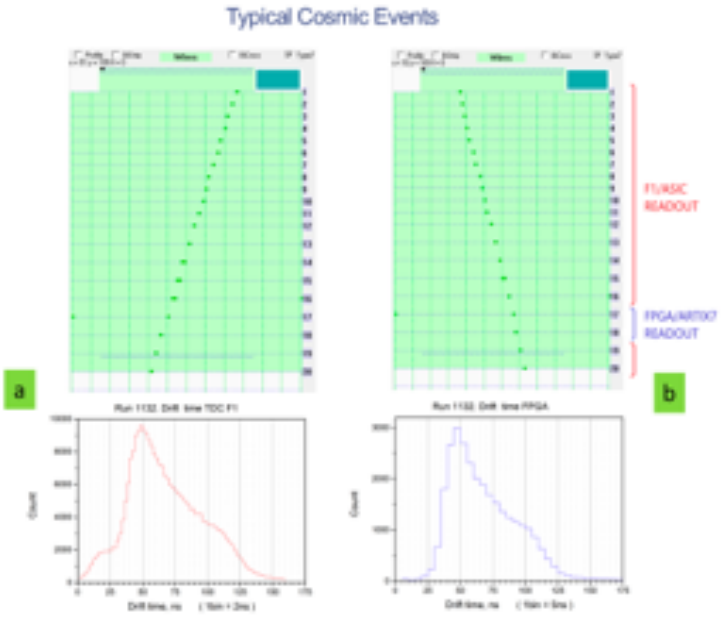

Fig. 4 FPGA digital readout test

The further tests will be conducted with a prototype of the SPD range system (~ 1200 channels of wire and strip readout) at the Nuclotron test beam area. At the first stage of working with the prototype of a muon system the standalone readout system described above will be used. Further on MFDM HotLink interface is meant to be replaced with an optical interface.

At the present time the final version of SPD DAQ has not been chosen yet, several options are being considered.

One of the options is oriented towards DAQ structure of COMPASS/AMBER experiment. According to this concept FPGA-based block HDmx (data handling multiplexer) (VME 6U, 2M) is used as a concentrator of first level (Fig. 5) This block contains 15 optical ports (UCF protocol) to connect with FEE electronics; one optical output port (Slink), and also several services interfaces: JTAG for downloading firmware program into HDmx FPGA: IPbus for connection via Ethernet and a TCS channel for connection with the Trigger Control System. Through the output port HDmx concentrator connects with the second level concentrator HDsw.

Fig. 5 Compass FPGA–based MUX unit

In another option of DAQ structure connection between FEE and first level concentrator DAQ is carried out through serial local electrical links (e-link). Each e-link consists of 4 connection lines (LVDS/SLVS): Reference Clock from the DAQ; Control signals from DAQ ; Hit-data from FEE; Slow control bidirectional line. The first three signals are transmitted through high-speed differential lines. Slow control signals (data) are transmitted via the I2C interface. Communication between the first and second level concentrators uses optical link designed for the total bandwidth of e-link lines.

Within the scope of R&D development of digital electronics for the muon system an interface cards will be created with an option of connecting MFDM unit to DAQ through either an optical channel or e-link lines.

A general view of the data flow structure for the Muon System is shown in Fig.4.32.

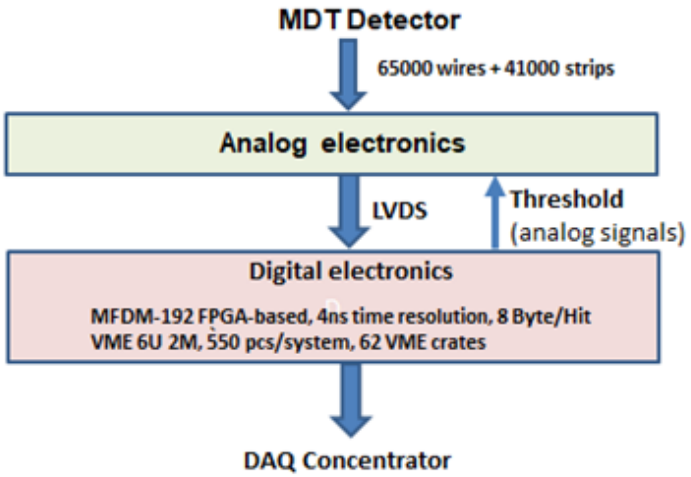

Figure 4.32: Data flow diagram – from the RS to the DAQ.

6. Prototyping

The evaluation of the main parameters of the proposed Range System is being performed with big pro- totype installed at CERN within the PANDA program. The prototype (see Fig.4.33) has a total weight of about 10 tons (steel absorber and detectors with electronics) and comprises 250 MDT detectors with 4000 readout channels (2000 for the wires and 2000 for the strips, 1 cm wide). It has both samplings (3 cm and 6 cm) present in the system (Barrel and End Caps), thus providing an opportunity for direct calibration of the response to muons, pions, protons, and neutrons.

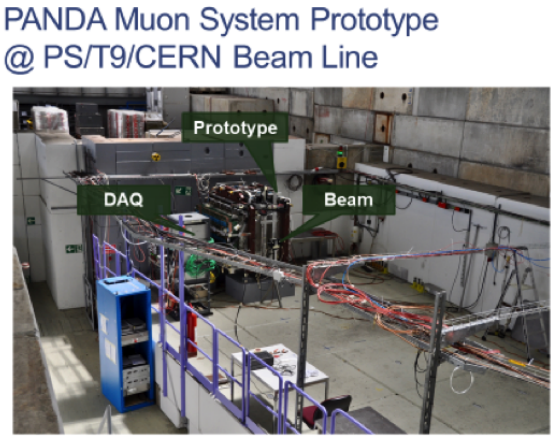

Figure 4.33: Range System prototype (10 ton, 4000 readout channels) at CERN.

Fig.4.34 gives the examples of the prototype response to different particles. The patterns demonstrate excellent PID abilities of the Range System. The data were taken during the May and August runs of 2018 at the T9/PS/CERN test beam. The beam particles hit the prototype from the top of the picture. The beam momentum for all the particles is 5.0 GeV/c. Neutrons were generated by a proton beam on a carbon target placed in the very vicinity of the first detecting layer. The points on the pictures represent
hit wires, thus giving the impression of a typical device response with an accuracy ~ 1 cm.

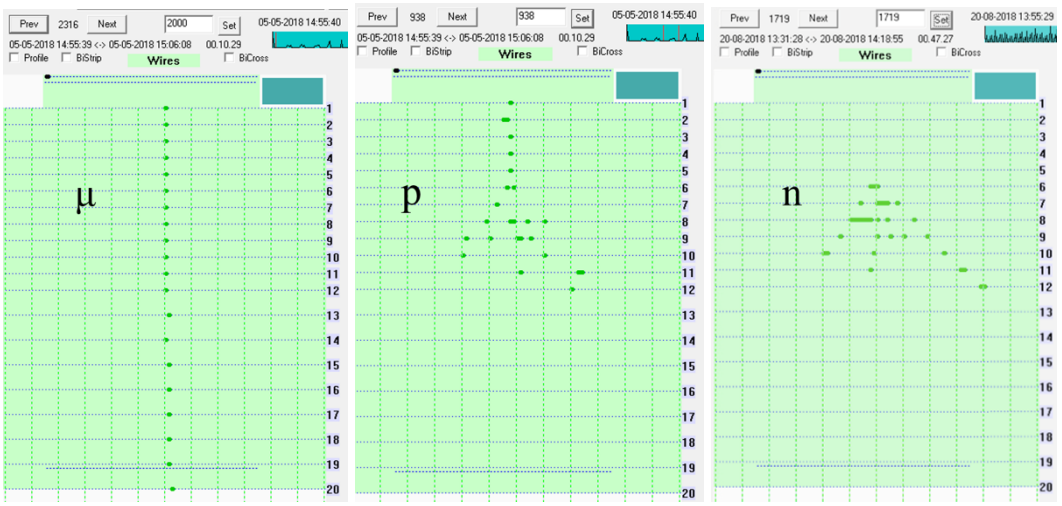

(a) (b) (c)

Figure 4.34: Demonstration of PID abilities: patterns for - (a) muon, (b) proton and (c) neutron.

7. Simulations and Performance

The performance of the SPD Range (Muon) System was evaluated with the help of Monte Carlo simulations of the detector within the SpdRoot framework as well as R&D program conducted with the RS Prototype on test beams (see Section 6). The studies include system response to the passage of particles with different energies, the efficiency of muon/hadron separation, testing the pattern recognition algorithm, and tuning the parameters of Monte Carlo simulation using experimental data.

After creating a description of the SPD Range System within the SpdRoot framework, based on engineering drawings, the full simulation of the entire detector became possible. The model of the RS prototype was also implemented within the SpdRoot package, which made possible direct comparison of the detector response to traversing particles.

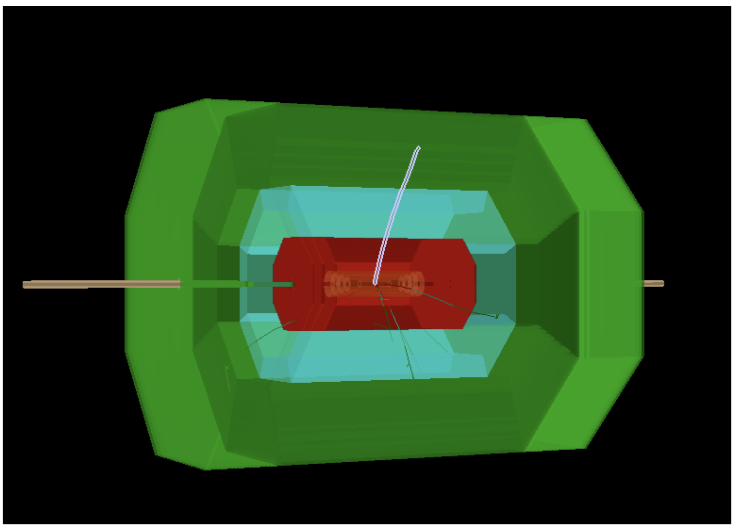

Fig. 7.1: 3D geometry model of the Range (Muon) System (green) implemented in the SpdRoot framework.

7.1 Detector Model

Preliminary Range System model was created and simulated using Geant4 and encapsulated within the SpdRoot framework. It consists of a barrel and two end-caps with equal thickness $\sim 4\lambda_I$. MC-point is created by Geant4 in a sensitive detector volume when a particle traverses through it.

7.1.1 Digitization tuning

Digitization is used while converting MC-points into hits (detector signal). The procedure is based on at least one of two requirements:

Cut 1: minimum passage in active volume ≥ 1cm;

Cut 2: minimum energy deposited in active volume ≥ 1 KeV.

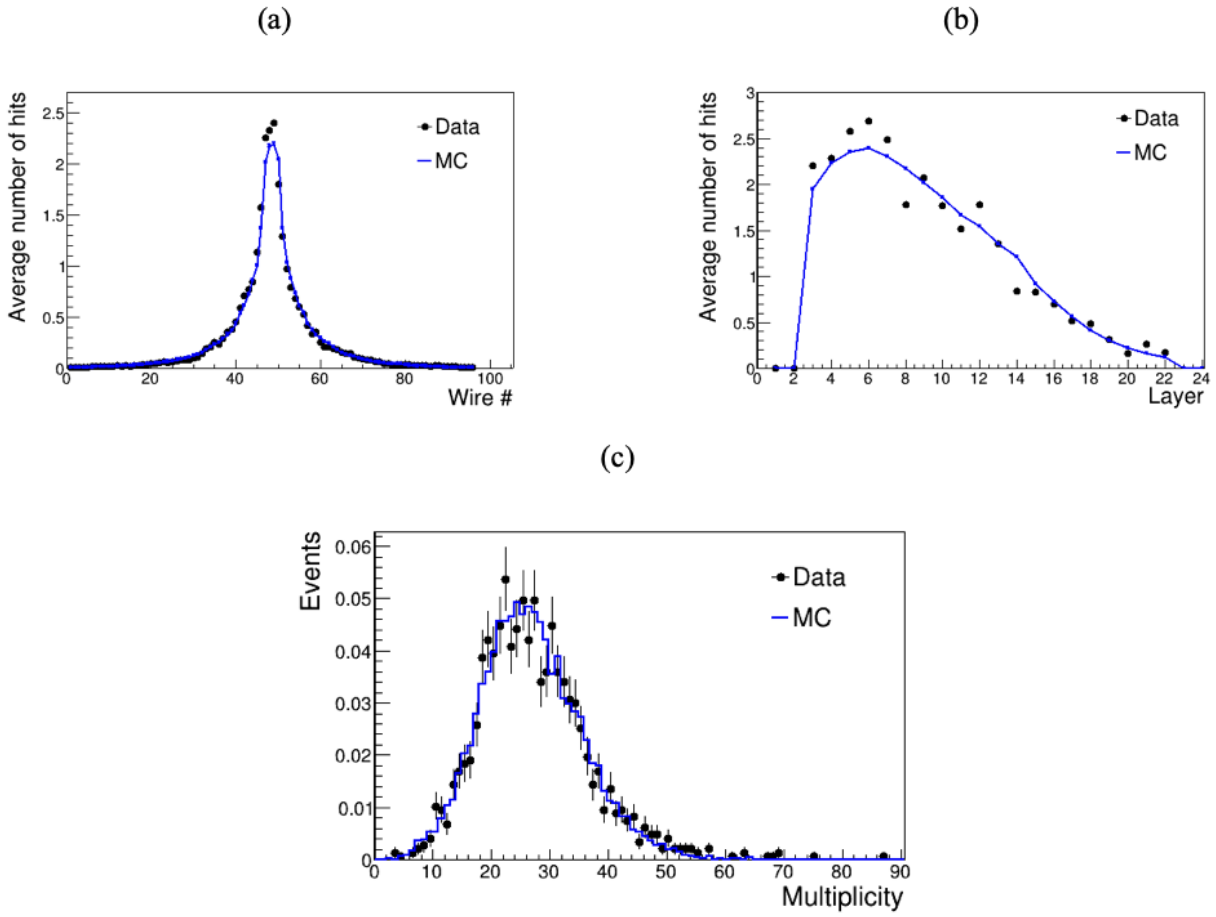

Fig 7.2: Calorimetric signal/response to the protons with momentum 6 GeV/c: (a) average hits per wire (all layers), (b) average hits per layer and (c) normalized hit multiplicity in an event.

7.2 PID Algorithms

One of the primary purposes of the Range (Muon) System is a reconstruction of charged particles traversing the RS and identification of muons and hadrons. Charged particles produce hits in the MDT detectors forming a hit profile in a layered structure of the Range System. The procedure is based on two-step processing the resulting hit profile: (a) forming clusters of hits by a clustering algorithm and (b) classification of obtained clusters as muons or hadrons. The main advantage of the described procedure is a relatively high processing speed compared to traditional track-reconstruction algorithms, since it exploits only the signals from Range System alone with no need of assigning tracks to those produced in the straw tracker.

7.2.1 Particle Reconstruction

[DBSCAN clustering algorithm description and performance figures to be inserted.]

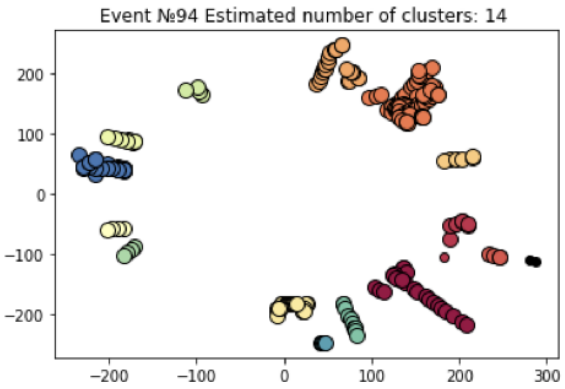

Figure 7.3: An example of clusters defined by the DBSCAN algorithm in a single J/psi->mumu event.

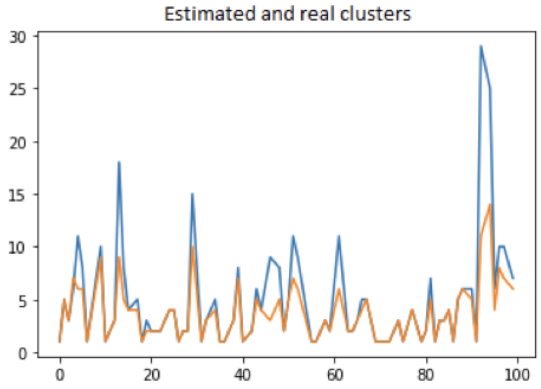

Figure 7.4: Number of true clusters (blue curve) and clusters found by DBSCAN algorithm (brown curve) in J/psi->mumu MC sample.

7.2.2 Muon/hadron separation

A hit profile in the Range System corresponding to a particular kind of particle with a certain momentum has a specific pattern. Low momentum hadrons (p < 1 GeV/c) almost indistinguishable from muons with the same momentum. The increasing energy of hadrons significantly changes the

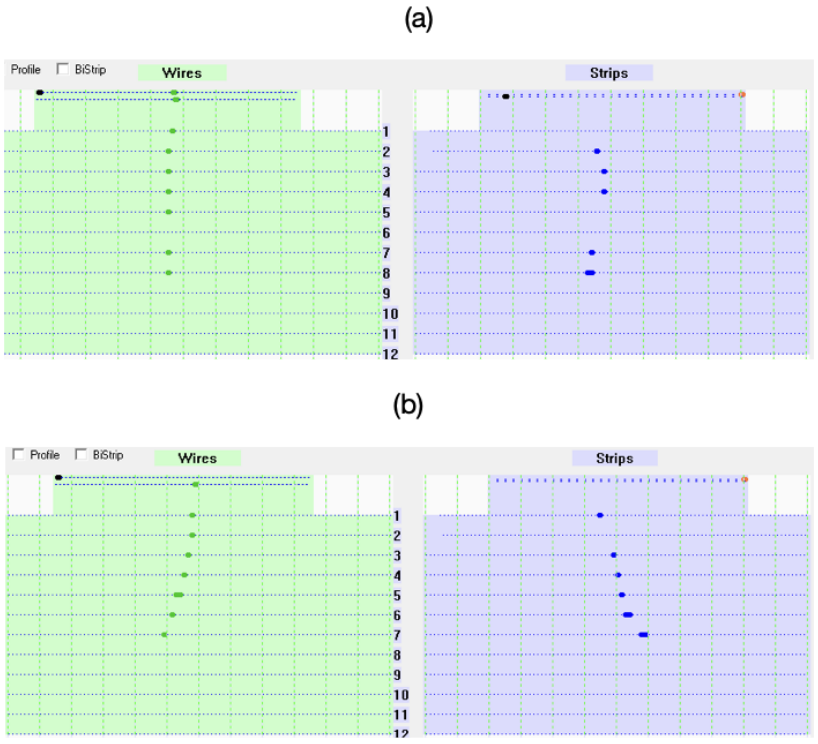

Figure 7.4: Comparison of wire (green) and strip (purple) profiles in

profile of hits, forming a cascade of secondary particles for hadrons with momentum up to 10 GeV/c.

(a)

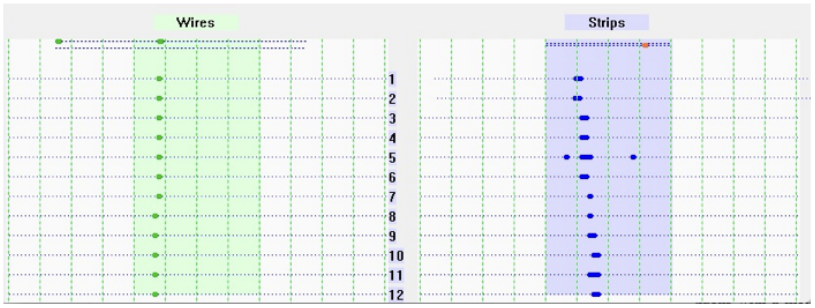

(b)

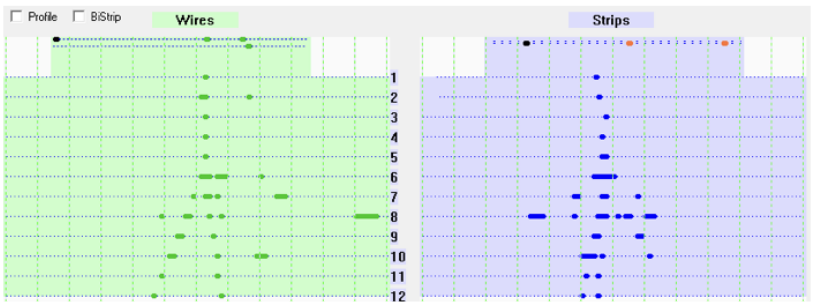

Figure 7.5: Comparison of wire (green) and strip (purple) hit profiles in the RS prototype for (a) muons and (b) pions with the same momentum 10 GeV/c.

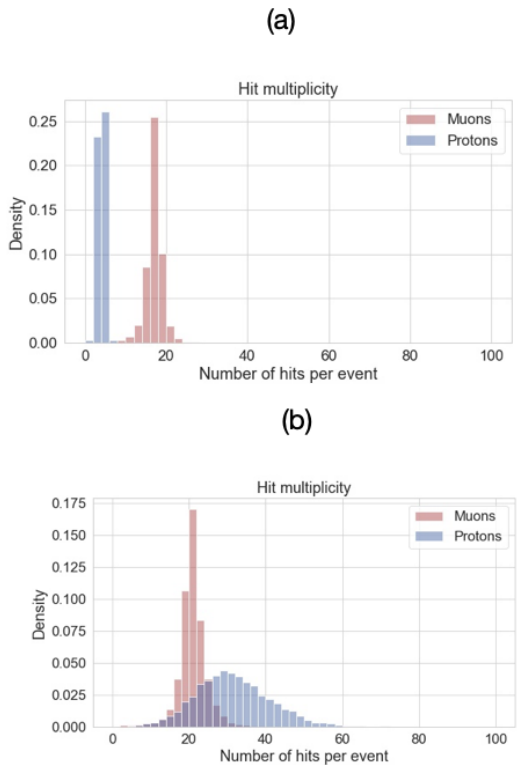

Figure 7.6: Normalized distributions of hit multiplicity per event for muons compared to protons with momentum (a) p = 1 GeV/c and (b) p = 6 GeV/c in SPD Range System (MC).

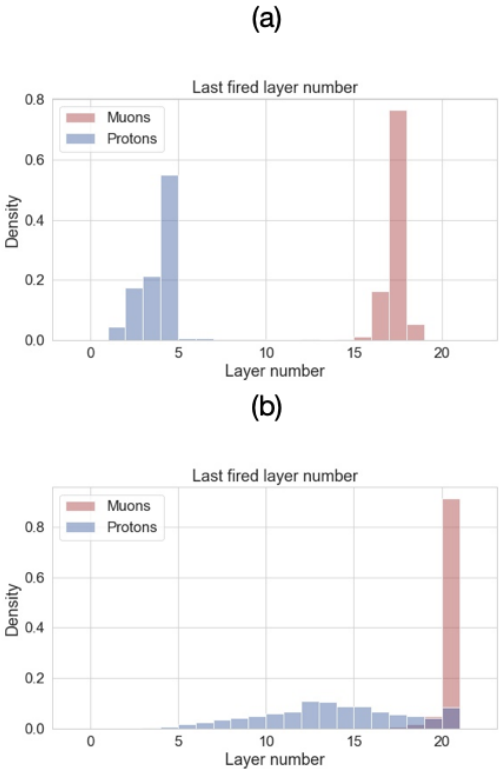

Figure 7.7: Normalized distributions of last fired layer number for muons compared to protons with momentum (a) p = 1 GeV/c and (b) p = 6 GeV/c in SPD Range System (MC).

Finding variables sensitive to differences in such patterns is directly related to the possibility of separation between muons and hadrons. It can be used as an input to various Machine Learning techniques.

As a starting point a Decision Tree classification algorithm is used to separate between signal (muon) and background (protons and pions) samples in Data and MC. The chosen technique is a well-known solution for binary classification (DecisionTreeClassifier from scikit-learn library). The main advantages of the algorithm are its robustness, transparency, and limited number of hyper-parameters for optimization. Events in both samples were labeled using time-of-flight detectors only. Later the Cerenkov counter tags will be used to fix the muons. The following variables are chosen as an input to the Decision Tree: hit multiplicity in an event, first and last fired layers, splitting layer number (the lowest number of a layer having ≥ 2 hits), and number of hits in the last layer. The normalized distributions of hit multiplicity per event and last fired layer number for muons compared to protons with momentum p = 1 GeV/c and p = 6 GeV/c obtained with SPD Range System (MC) are shown on Fig. 7.6

and Fig. 7.7. The hit multiplicity is found to be the most powerful discriminative variable while the last fired layer number also showed high importance for muon/hadron separation. The applied technique allows to differentiate between the classes with 95–97% accuracy for muons/pions and 96–99% for muons/protons. The analogous method was applied on RSP dataset and showed less accuracy of 93% for muons/protons separation mainly due to the impurity of the signal muon sample, since the events in data were labeled using TOF detectors only. Later the Cerenkov counter tags will be used to fix the muon data sample.

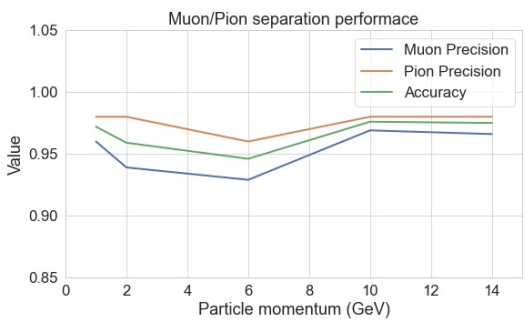

Figure 7.8: Muon/pion separation performance as a function of particle momentum.

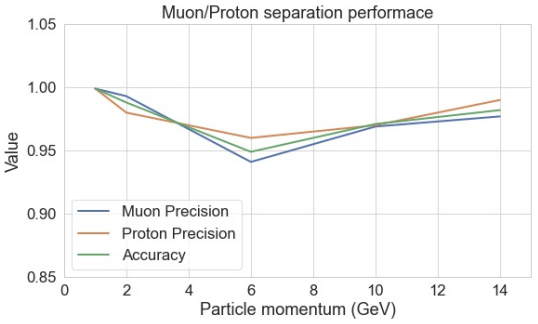

Figure 7.9: Muon/pion separation performance as a function of particle momentum.

7.6 Cost estimate

The preliminary cost estimate for the Range System is presented in Tab. 4.7.

Table 4.7: Cost estimate for the RS.

	Cost, M$
MDT detectors with strip boards	2.35
Analog front-end electronics (including cabling)	2.78
Digital front-end electronics (including VME crates and racks)	3.05

Yoke/absorber (without supporting structure and movement system)	6.00
Total	14.18

References:

[1] SPD/NICA CDR

[404] V. M. Abazov, G. D. Alexeev, Yu. I. Davydov, V. L. Malyshev, V. V. Tokmenin, and A. A. Piskun. Comparative analysis of the performance characteristics of mini-drift tubes with different design. *Instruments and Experimental Techniques*, 53(3):356–361, May 2010.

[405] V. M. Abazov, G. D. Alexeev, Yu. I. Davydov, V. L. Malyshev, A. A. Piskun, and V. V. Tok- menin. Coordinate accuracy of mini-drift tubes in detection of an induced signal. *Instruments and Experimental Techniques*, 53(5):648–652, Sep 2010.

[406] PANDA Collaboration. Technical Design Report for the: PANDA Muon System (AntiProton Annihilations at Darmstadt). Strong Interaction Studies with Antiprotons https://panda.gsi. de/publication/re-tdr-2012-003. September 2012.

[407] V. M. Abazov et al. The Muon system of the run II D0 detector. *Nucl. Instrum. Meth.*, A552:372– 398, 2005, physics/0503151.

[408] P. Abbon et al. The COMPASS experiment at CERN. *Nucl. Instrum. Meth.*, A577:455–518, 2007, hep-ex/0703049.

[409] G.D.Alekseev,M.A.Baturitsky,O.V.Dvornikov,A.I.Khokhlov,V.A.Mikhailov,I.A.Odnok- loubov, and V. V. Tokmenin. The eight-channel ASIC bipolar transresistance amplifier D0M AMPL-8.3. *Nucl. Instrum. Meth.*, A462:494–505, 2001.

[410] G.D Alexeev, M.A Baturitsky, O.V Dvornikov, V.A Mikhailov, I.A Odnokloubov, and V.V Tok- menin. The eight-channel fast comparator IC. *Nucl. Instrum. Meth.*, A423(1):157 – 162, 1999.

[411]G.D.Alekseev,M.A.Baturitsky,O.V.Dvornikov,A.I.Khokhlov,V.A.Mikhailov,I.A.Odn ok- loubov, A. A. Shishkin, V. V. Tokmenin, and S. F. Zhirikov. The D0 forward angle muon system front-end electronics design. *Nucl. Instrum. Meth.*, A473:269–282, 2001.

[412] G.D. Alekseev, A. Maggiora, and N.I. Zhuravlev. Digital Front-end Electronics for COMPASS Muon-Wall 1 Detector. *JINR Preprint*, E13-2005-37, 2005.

Appendix 1. Technical design of the Mini Drift Tubes (MDT) workshop (includes production and test areas)

1. Introduction

Mini drift tubes (MDT) (photo 1) are gaseous detectors manufactured from thin-walled (0.45mm thickness) 8-section aluminum profiles (1), with tungsten wires of a 50 microns' diameter stretched inside each section. The profile is placed in a plastic case (3) sealed with plastic end-plugs from both ends (4). The end-plugs have special openings designed for the input and output of the working gas, as well as for high voltage supply and detector signals readout.

It is planned to organize a full cycle for the serial production of a large number of MDT detectors with length dimensions reaching up to 4.5 m in building 73.

The production cycle implies the presence of the following premises: two procurement halls, washing room, assembly and test areas.

Technological process of MDT production

The preparation of the MDT plastic cases and AL profiles with the desired lengths, as well as perforation (penetration of holes for laying the bases) of profiles are made in the procurement area. Then cases are blurred with compressed air to remove the dust and moved to a separate rack in the assembly area. Ready profiles go to the washing room where they pass a 3 step washing procedure. At the first stage, the profiles are cleaned in hot water containing detergent powder at a temperature of about 60°C to remove possible grease stains and other contaminants. In the second and third stages, the profiles are rinsed in hot and distilled water, respectively.

The washed and dried profiles are stored on the racks in the second procurement hall. In a separate room, the selection, purging and washing of plastic parts (end-plugs, covers, bases, boards, support spacers) are carried out in a solution of ethyl alcohol with water; wires are soldered to active end-plugs and matching resistors to boards; installation and welding of bases into profiles is done; spacers are marked and laid into the profiles. Then the profiles are transferred to the assembly area.

Soldering of the 8 anode wires laid along the profile sections on the spacers is made using a semi-automatic winding machine. Then the spacers are welded on the brewing machine to fix them in certain places inside the profile. After that, the wires of the active end-plug are soldered to the boards installed in the profile. Then a plastic case muffled from one end by a passive end-plug is put on the profile.

After that, the testing cycle begins on special stands for the anode wire tension test and preliminary high voltage test. In the case of a positive test result, the second end of the case is muffled by the active end-plug and welded using a brewing machine. Then the ready tube is filled with the working gas and passes high-voltage training. The last stage of testing is gas tightness check.

Verified MDTs are stored on special racks.

2. The terms of reference provides for:

1) Partial reconstruction of building 73.

2) Allocation of manufacturing facility (previously used at the JINR OP) for the MDT mass-production and testing in the announced building

3) Fulfillment of requirements for production and auxiliary premises,workplaces, equipment, personnel required

- to ensure the safe conduct of work in the manufacture of products at all stages of the assembly and installation process;

- for the manufacture of products that meet the requirements.

The building plan is given in Appendix 1 and includes the following premises distinguished by type of work:

1st floor

Service and utility rooms:

Room 1, 1A - physicists room

Room 2 - warehouse;

Room 3 - service room;

Room 11 - computer room

Room 11A - service room

WC room - bathroom and shower

Industrial premises:

Room 4 – assembly room:

C - table for washing and preparation of plastic parts (end-plugs, bases, spacers, covers);

MC - assembly table for soldering wires to active end-plugs and putting on cambric;

Room 5 - procurement area No. 1:

Racks $5_{1,2}$ for profiles and plastic cases before processing;

Racks 5_3 - rack for finished products;

Electric hoist for 0.5 tons.

Room 6 - washing area:

1) B1, B2 and B3 - three baths for sequential washing of profiles. Baths B1 and B2 are filled with hot water (about 0.6m3) from the plumbing system and maintained at a temperature of about 60 ° C using electric heaters. Dimensions B1 and B2: 600x600x6000mm, B3: 400x400x6000mm. Bath B3 is filled with distilled water (about 0.4m3) at room temperature.

2) D - distiller. Overall dimensions: 700x700x2000mm

3) B4 - tank for checking the gas tightness of the manufactured MDT. Dimensions B4: 300x360x7000mm. Bath B4 is filled with distilled water (about 0.4m3).

4) B - a cylinder with N2 gas;

5) Czh6 - rack for preliminary drying of washed profiles.

Room 7 - procurement area No. 2:

1) installation of boards, bases, spacers;

2) Szh7 - rack for prepared profiles;

3) Ст1 and Ст2 - machines for profiles trimming and perforating;

4) St3 - machine for cutting of plastic cases

Room 8 - Assembly area:

1) C1 - machine 1 for wire winding;

2) C2 - machine 2 for spacers welding spacers;

3) C3 - workstation for soldering the wires of the active and-plugs to the boards;

4) C4 - machine 4 for welding of the end-plugs to the plastic cases;

5) Collection table. - mobile table for tube assembly;

6) B - tank with cooling water for machine tool 4;

7) Szh8 - a rack for MDTs prepared for testing.

Room 9 - area for testing of manufactured MDT:

1) Stand 1 - a stand for checking the tension of wires;

2) PC - personal computer (3 pcs.);

3) Stand 2 - a stand for testing of MDT for dark current;

4) Stand 3 - stand for high-voltage training of MDT with a working gas mixture of 30% CO_2 + 70% Ar;

5) Szh9 - rack for finished product.

Room 10:

1) GP - gas control panel;

2) Cylinders with CO_2 (1-2 pieces) and Ar (3-4 pieces);

3) Szh10 - rack.

2nd floor

Room 12: Scintillator site

Stand 4: Assembly, gluing, taking of scintillator samples optical characteristics

Szh12 - rack 12

3rd floor:

Meeting and relaxation room

3. Safety requirements

When performing the technical processes of assembly and installation of MDT, it is necessary to comply with the requirements for safety and prevention of the impact of the following factors:

- electric shock;

- explosion and fire safety;

- harmful effects of toxic and irritating substances;

1. To prevent electric shock, provide:

- protection of wiring insulation from mechanical damage;

- grounding of equipment cases, the live parts of which may be energized;

- fulfillment of the requirements of the current "PTE of electrical installations of consumers", "PTB during the operation of electrical installations of consumers", "PUE", approved by the Head of Energy Supervision, as well as instructions on safety of JINR;

- equipping all premises with an automatic fire alarm system.

2. To ensure explosion and fire safety, provide:

- rooms equipped with supply and exhaust ventilation in an explosive design and automatic fire alarms in accordance with GOST 12.4.021 and SN P2.04.91 for storage and spilling of flammable liquids, for preparing washing solutions, for carrying out cleaning operations;

- Spillage of flammable liquids using devices on pallets with sides not less than 50mm;

- containers for flammable liquids, made of unbreakable materials that exclude sparking and accumulation of static charge, with tightly closing lids for storage, use at workplaces, transportation, disposal of flammable liquids with the inscription “Flammable”; remove content at least once per shift;

- utilization and regeneration of flammable liquids and contaminated cleaning materials in accordance with OST 4GO 054.096.

3. To prevent the harmful effects of toxic and irritating substances, provide:

- supply and exhaust ventilation for assimilation of harmful substances below the maximum permissible in all rooms of the building 73;

- workstations for soldering wires with an exhaust hood in rooms 4 and 6;

- local exhaust ventilation at workplaces in rooms 4,6-9.

Hazards emitted in the production areas of building 73 during a work shift

№	Emitted hazards	Position of work place	Room №.	ПДК mg/m^3	Hazard toxicity class (GOST 12.1.007)

1	Vapors of solder POS 61 (for lead)	MC C1, C3, C4	7 8	0.100	1 class
2	Vapors of pine rosin	MC C1, C2	7 8	7.0	3 class
3	Ethyl alcohol	MC C1	7 8	100,0 50,0	4 class

4. To provide the following conditions at any time of the year in rooms 1.4-13:

- air temperature 20 ± 2 ° C

Base:

- OST 4 GO.091.202 - Assembly and assembly production. Organization of special areas and areas of specialized workshops and areas of the main production.

- OST 11.073.062 - 76 - Requirements and methods of protection against static electricity in the conditions of production and use.

Technical requirements

1. Antistatic protection

- All workplaces (assembly table (room 4), machines 1-4 (room 8), stands 1-4 (room 9) and machines 1-3 (room 7)) must have terminals and be grounded.

- Grounding of equipment and tools powered from the mains must be autonomous, in accordance with the "Rules for Electrical Installations".

- Foam rubber mats impregnated with an antistatic agent must be provided in front of the doors inside rooms 6, 7, 8, 9, 12. Mats should not interfere with door opening.

2. Power supply.

- Carry out the internal wiring of the electrical networks of the building in accordance with applicable rules and regulations. The power consumption of the simultaneously operating equipment is 50 kW, 380V, 50Hz.

- In the premises: 4,6 -9,11,12 design the physical grounding connection. Lay the bus at a distance of 20-30 cm from the floor level from an aluminum strip with a section (30x3 ÷ 4) mm along the contour of the premises.

"Physical earth":

- must have a resistance of 0.1 ohm;

- must not have connections to the protective grounding circuit;

- carried out by a separate bus and should not touch any metal structures.

Provide the supply of electricity and grounding to the equipment in accordance with the passports and PUE and power them through the euro sockets.

Power all workplaces through euro sockets in accordance with the specification, one outlet per workplace and one outlet per unit of desktop equipment. Stationary equipment is installed in accordance with the PUE.

Design general lighting of premises with gas-discharge lamps. Illumination for IIIb category of visual work (tab. 1 SNiP 11-4-79) in the combined lighting system in rooms 1-4, 10, 11, 11A, 13, and in other rooms 5-9, 12-300 lux.

Provide local lighting at all workplaces.

On the border of the balance sheet, provide for the installation of metering devices for the consumption of energy consumed.

3. Construction work

When carrying out a partial reconstruction of building 73, the following circumstances must be taken into account:

- to place in building 73 a section for the production of wire detectors that operated at the JINR OP;

- free movement of MDT and its elements up to 4,5m long between different areas (rooms);

- production of MDT is associated with the release of harmful substances vapors of rosin, POS61 solder, ethyl alcohol;

- the collection area must be isolated from the washing area with two sealed doors to prevent water vapor from entering the washing area;

- storage of finished products (MDT).

In accordance with this, it is necessary to perform the following work:

1) Remove partitions in rooms 6 and 8 from the floor to a height of 2m, in room 7 (in its inner part) completely, and in its section 7 from the floor to a height of 2m.

2) Make a doorway between rooms 5 and 6 (marked with the letters DP) instead of windows and put a sliding door.

3) Make openings in the wall between rooms 9 and 10 measuring 200x300mm for gas supply from the gas control panel to the MDT and between rooms 6 and 7 measuring 300x1000mm for moving the profiles (in both cases, the height of the openings from the floor is 1.4m).

4) Install sliding sealed doors in rooms 6, 7 and 9 from their inner sides (marked with the letters D).

5) Cover the walls in room 6 adjacent to the bathtubs with tiles up to a height of 1.2m.

6) Install the door in room 10 from the side of the corridor (marked with the letters D).

7) Build a vestibule in front of the gate to room 8.

8) Install a 0.5-ton electric hoist in room 5.

9) Install the door between rooms 5 and 9.

4. Water supply and sewerage

1. Restore water supply and sewerage in the same volume, i.e. in the same that existed before the accident.

2. Provide for the filling with water of the baths B1, B2, B3, B4 and the distiller D, installed in room 6, and the subsequent draining of water from them. To do this, you must provide eyeliner:

1) Hot water to two baths B1 and B2, each with a capacity of about 0.7m 3;

2) Cold water to a distiller with a capacity of 0.5m 3.

3) Distilled water from the distiller to baths B3 and B4, each with a capacity of 0.5m3.

3. Install sinks for hand washing in rooms 4, 6, 7, 8, 10, 13.

4. Provide for the drainage of water from the baths into the sewerage system.

5. Ventilation and heating

1. Provide for general exchange supply and exhaust, local ventilation in all production and utility rooms.

2. Provide for local exhaust ventilation to workplaces for hoods (1st floor):

1) In rooms 4 and 8 of harmful substances - vapors of rosin, ethyl alcohol and POS 61 solder during the entire work shift, installing ventilation ducts above machines C1 and C3 (room 8), as well as above the assembly table MS (room 4), where the wires will be soldered;

2) In the room there are 9 water vapors during the periods of cleaning the profiles;

3) In room 12 (2nd floor) vapors of synthetic adhesives, installing a ventilation duct above the work table.

3. In rooms 1, 4-10, 11-13, ensure a temperature of 20 ± 20C in any period of the year.

Notes

1. When carrying out a partial reconstruction of building 73, it is necessary to use the elements of the power supply system (grounding buses, electrical sockets) and the ventilation system, which are available in this building, as well as removed from the wire detectors section of the JINR OP.

2. The development of partitions in rooms 6, 8, 71 can be carried out incompletely, limiting the height from the floor to approximately 2 m.

Basis for MDT mass production workshop

(bld.73 of Laboratory of Neutron Physics, slide shows plan of 1-st floor from Technical Design on building reconstruction)

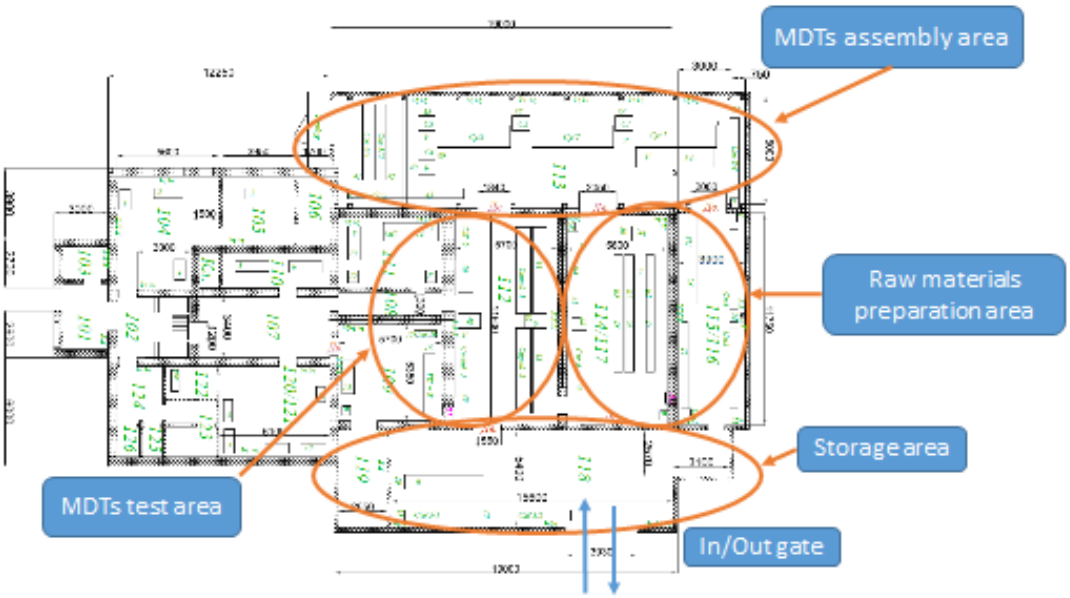

Plan of floors with equipment presents on Figs. 2 and 3

Appendix 1

Bld.73. Plan of 1st floor

Figure 2

Appendix 1

Bld. 73. Plan of 2 and 3 floor
и 3-го этажа

Figure 3

Appendix 2 (описание и план стенда стриповых плоскостей)

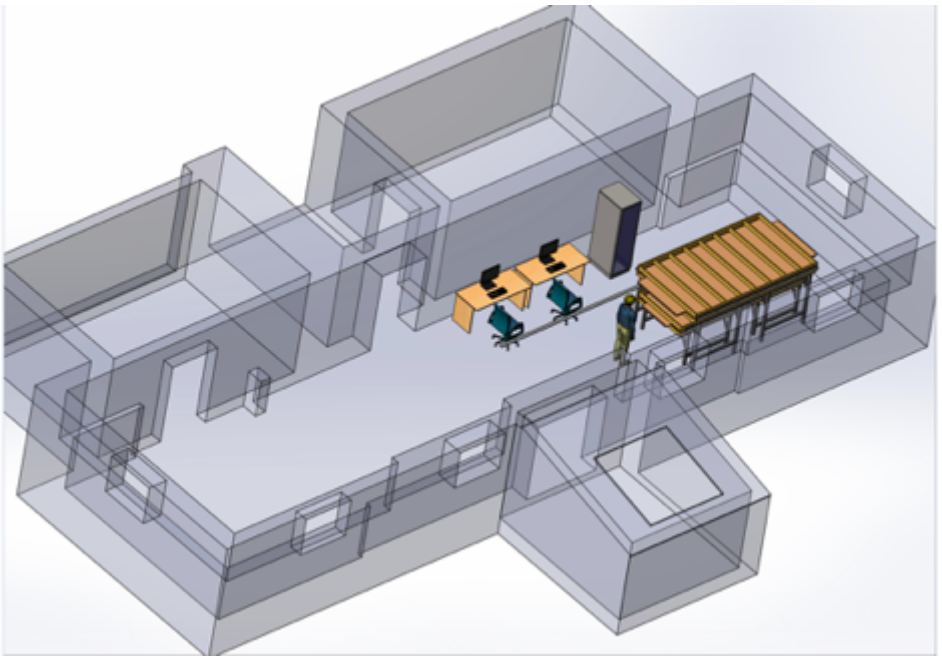

Fig. 1. Location of Stand for strip-boards testing.

Fig. 2. Half-stand for big strip-board testing.

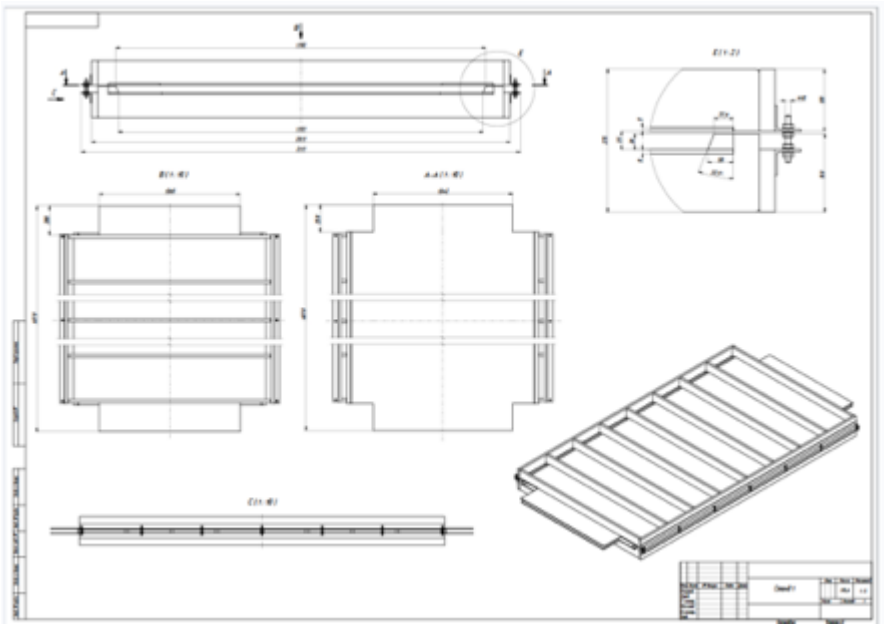

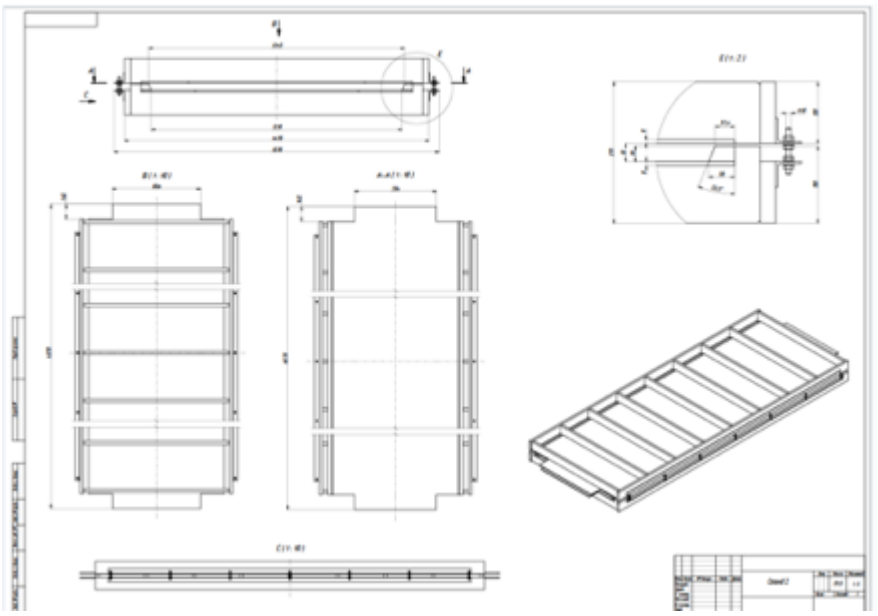

Additional pictures

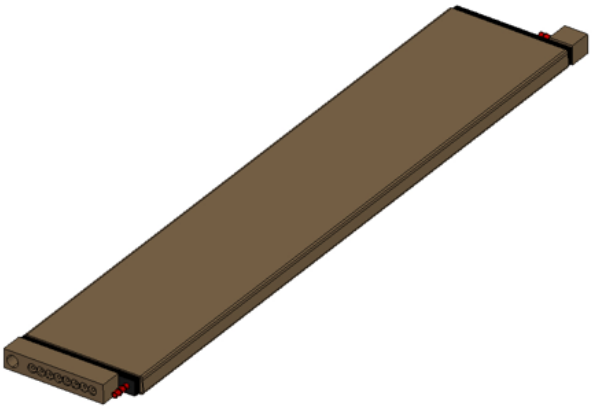

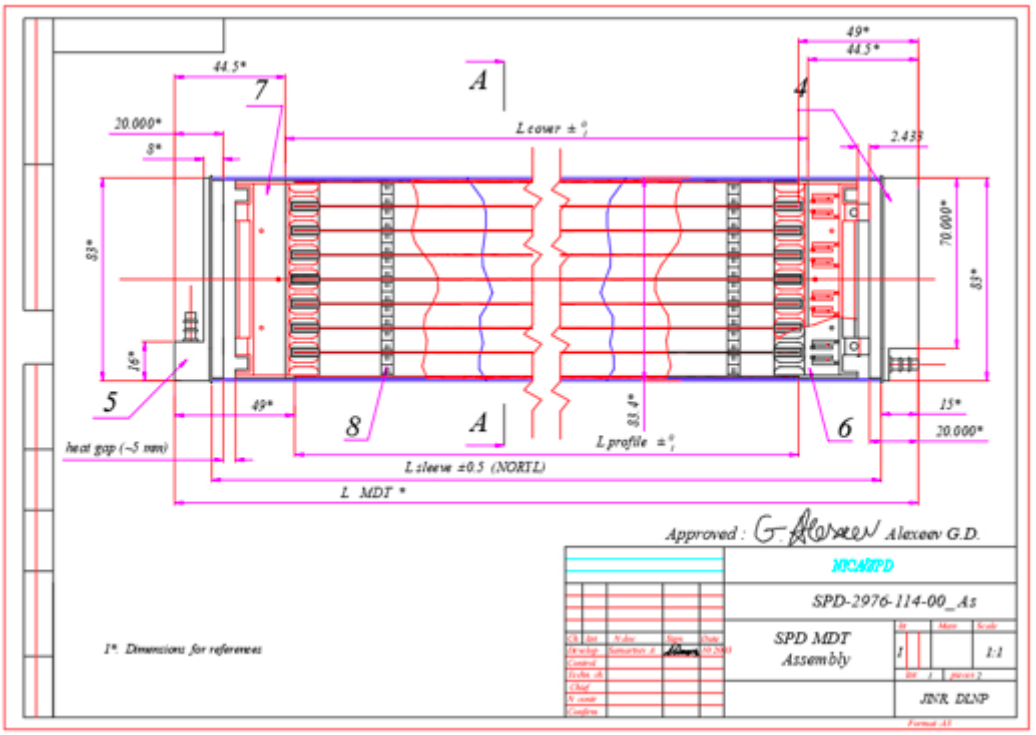

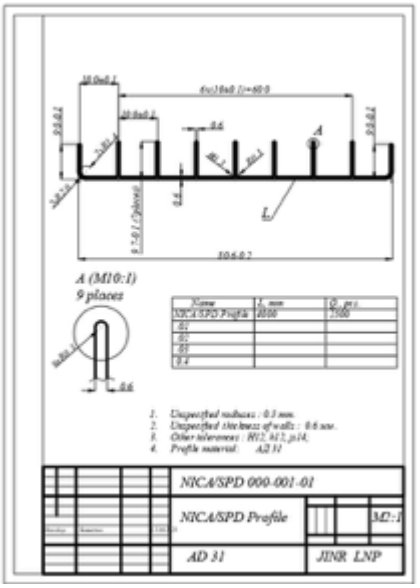
A (M10:1)
9 places
1. Unspecified radiuss : 0.3 mm.
2. Unspecified thickness of walls : 0.6 mm.
3. Other tolerances : H12, h12, js14.
4. Profile material : AD 31
NICA/SPD 000-001-01
NICA/SPD Profile
3D::1
AD 31
JINR LNP

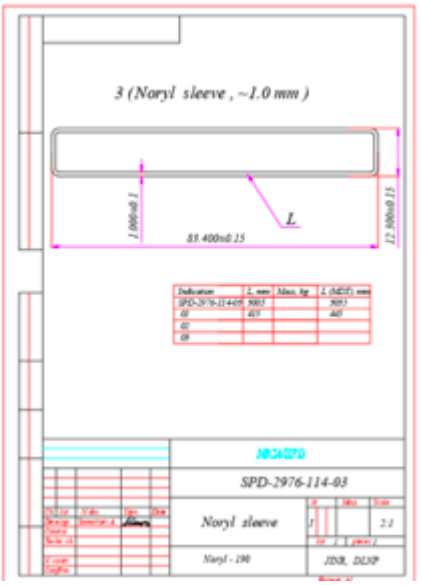
3 (Noryl sleeve , ~1.0 mm)
NICA/SPD
SPD-2976-114-03
Noryl sleeve
Noryl - 190
JINR, DLNP

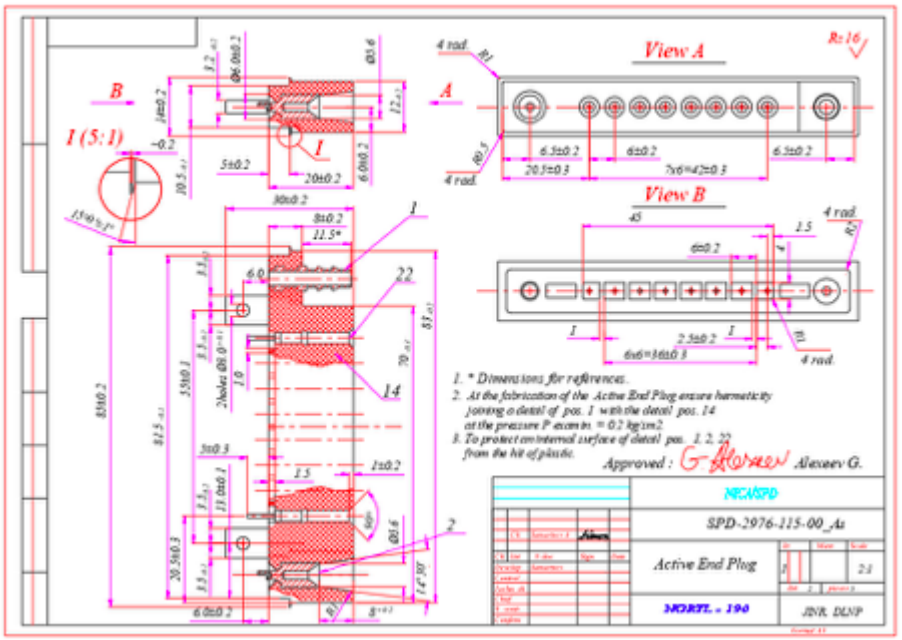
View A
View B
R=16
1. * Dimensions for references.
2. At the fabrication of the Active End Plug ensure hermeticity joining o detail of pos. 1 with the detail pos. 14 at the pressure P excess = 0.2 kg/cm2.
3. To protect on internal surface of detail pos. 1, 2, 22 from the hit of plastic.
Approved : Alexeev G.
NICA/SPD
SPD-2976-115-00_As
Active End Plug
MORTL. - 190
JINR, DLNP

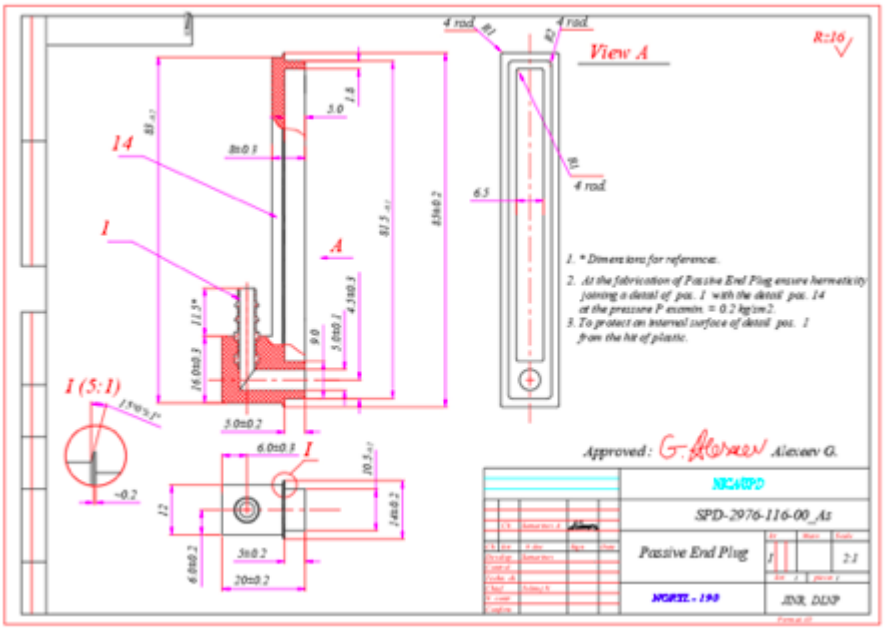
View A
R:16
I (5:1)
Approved: Alexeev G.
SPD-2976-116-00_As
Passive End Plug
JINR, DLNP

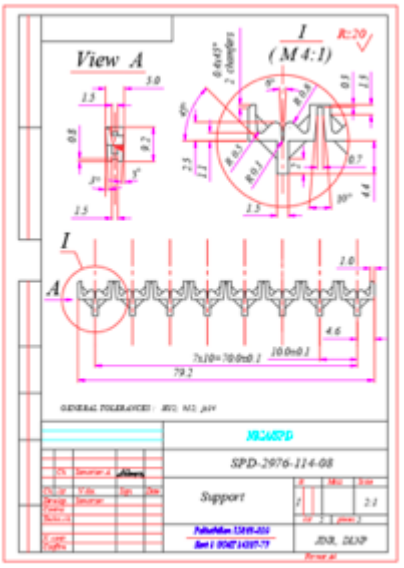
View A
I (M 4:1)
R:20
SPD-2976-114-08
Support
JINR, DLNP

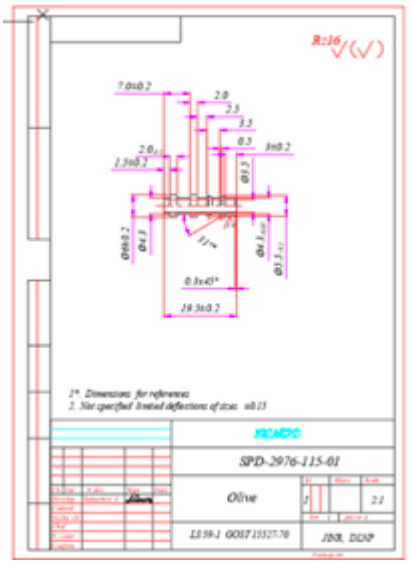
R:16
SPD-2976-115-01
Olive
JINR, DLNP

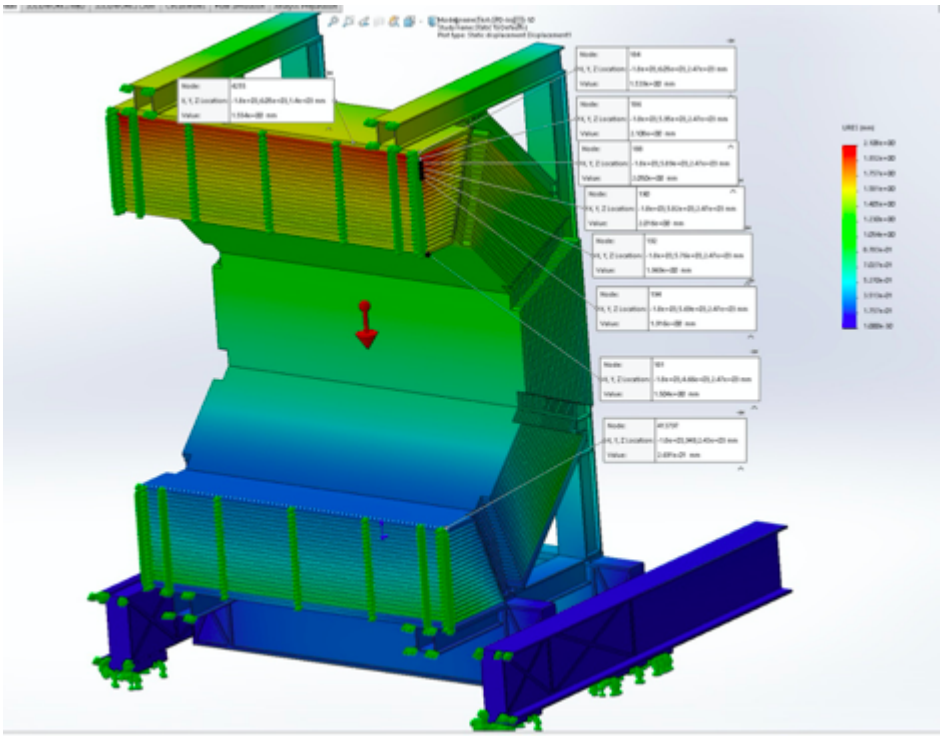

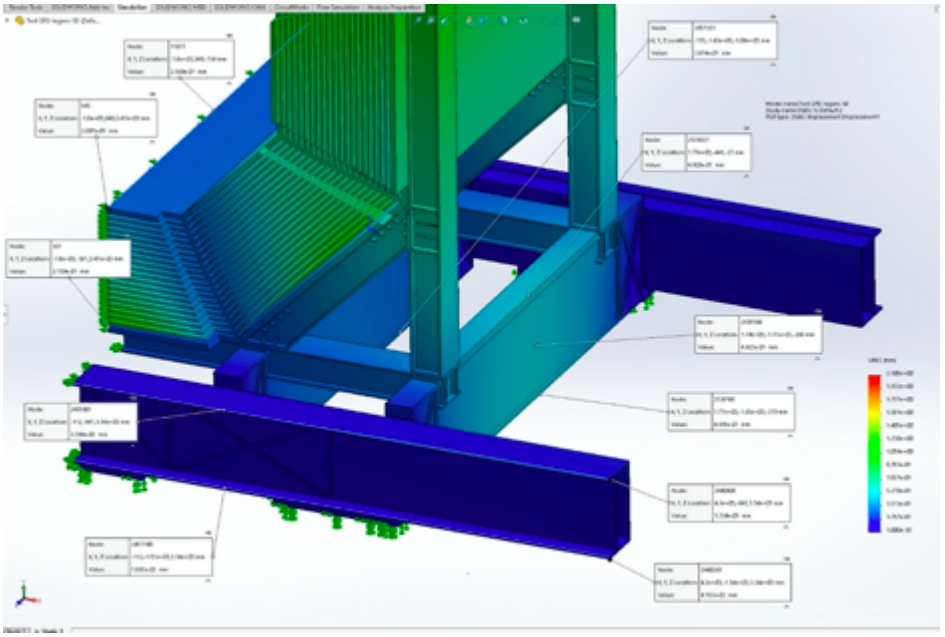

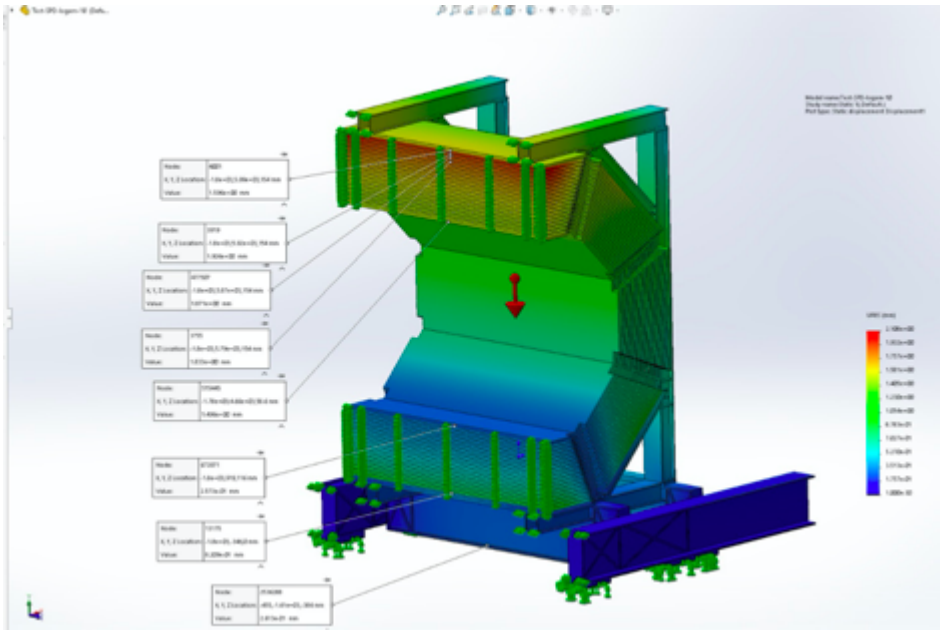

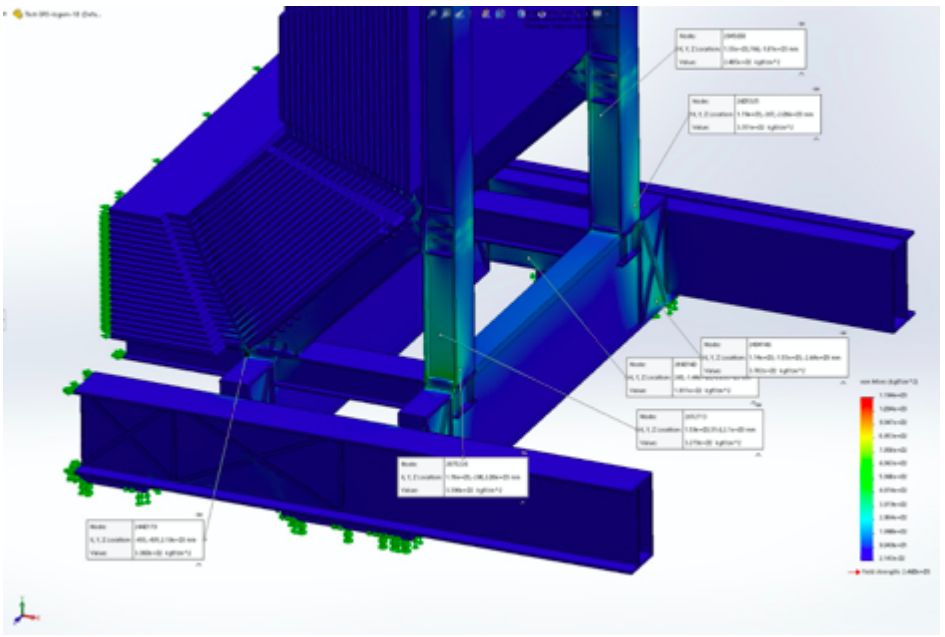

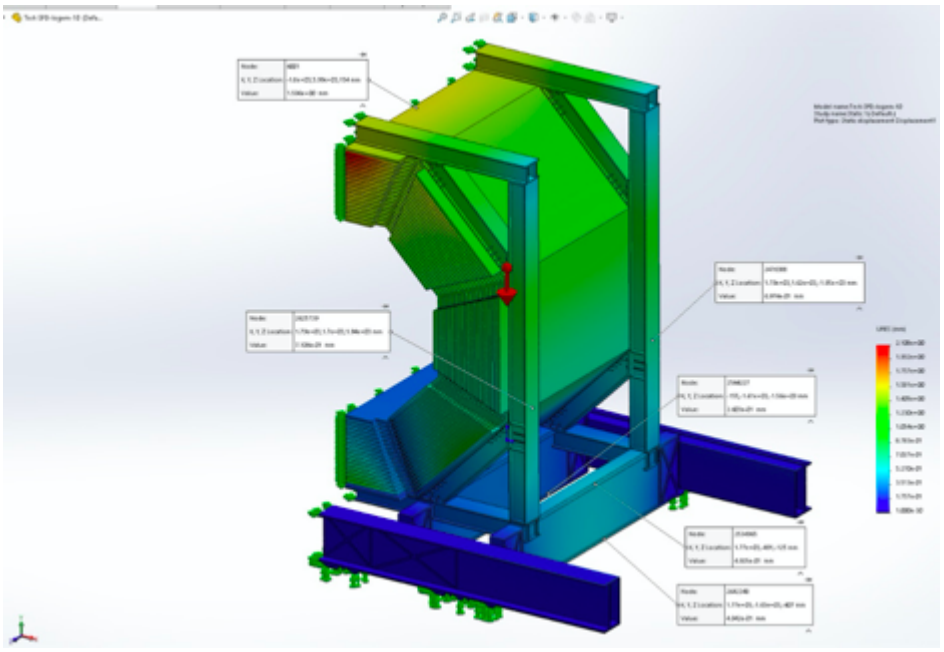

8.1 Time-of-flight system

The purpose of the time-of-flight (TOF) system is to discriminate between charged particles of different masses in the momentum range up to a few GeV/c. A short distance of 108 cm between the collision point and the TOF dictates the requirement for the time resolution of the TOF to be better than 70 ps. In view of the uncertainty related to the length of the interaction region (about 60 cm), the time t_0 which can be assigned to the collision vertex will only be on the order of 1 ns, so it is useless for identification purposes. Therefore the particle identification (together with the t_0 determination) can only be done for multi-track events, where several particles emerged from a same primary vertex hit active elements of the TOF. A certain mass hypothesis will have to be applied in this procedure. For details of this analysis see Section 1.4 of Chapter 9. In addition to the particle identification, the detector will also provide a start time to the straw drift tubes.

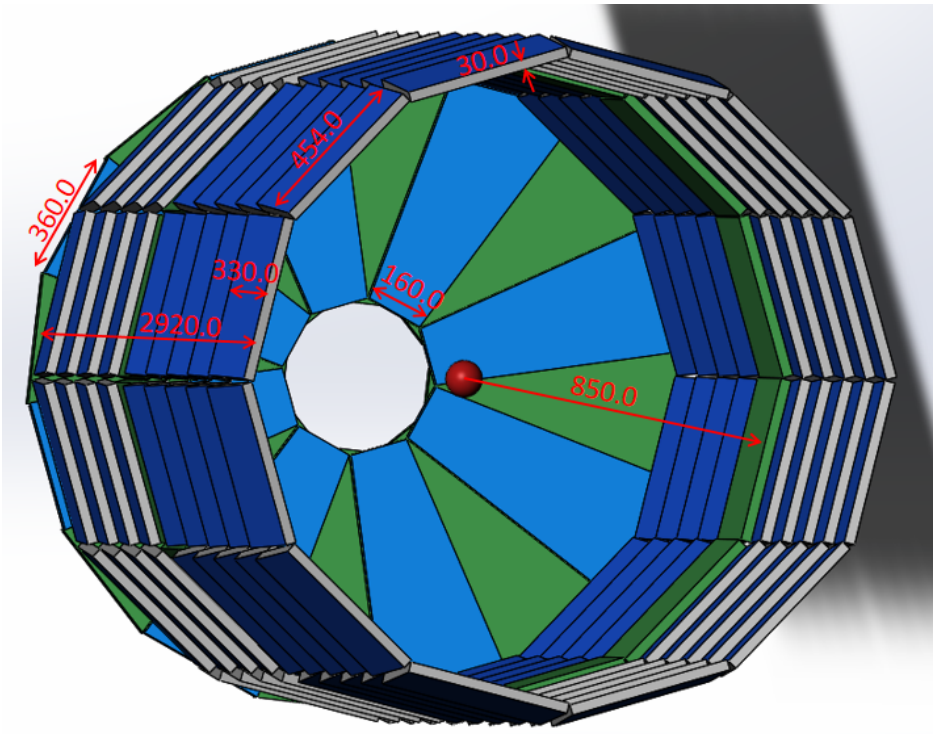

Figure 4.35: The multigap Timing Resistive Plate Chamber, mRPC is considered for PID system . Barrel and one of two end-cap parts are shown.

The TOF system will consists of a barrel and two end-cap parts with an overall active area of 27.1$m^{2.}$ The charge particle rate that detector will have to withstand is 0.1 kHz/cm^2 for the barrel. The rate increases rapidly when moving closer to the beam axis. Thus, for the TOF elements located in the end-caps 20 cm off the beam axis, the rate of about 1 kHz/cm^2 is expected (see Fig. 9.3 for details). MRPC technology is being considered for the detector which is shown in Fig. 4.35.

The multigap Timing Resistive Plate Chamber. It is a stack of resistive glass plates with high voltage applied to external surfaces and the pickup electrodes are located inside the chamber. A fast signal induced on the pickup electrodes by an electron avalanche is further transported to FEE located nearby. In order to increase the speed of gas exchange and reduce the gas consuming, we designed a new self-sealed MRPC. The schematic cross-section of the MRPC is shown in Fig. 4.36 [1]. In order get good time resolution (better than 40ps), a four stack 24-gaps MRPC will be used in SPD. The number of MRPC for barrel and endcap TOF, and number of corresponding readout channels are all shown in the table. It can be seen the whole TOF consists of 216 MRPCs and 8832 readout channels.

Table 1.1 Main parameters of the TOF system.

		Number of detectors	Number of readout strips	Sensitive area, m^2	Number of FEE cards	Number of FEE channels
Barrel	$MRPC_B$	1	24	0.14	3	48
	$Module_B$	10	240	1.4	30	480
	$Total_B$	120	2880	16.8	360	5760
End-cap	$MRPC_E$	1	16	0.06	2	32
	$Module_E$	3	48	0.18	6	96
	$Total_E$	96	1536	5.8	192	3072
Total		216	4416	22.6	552	8832

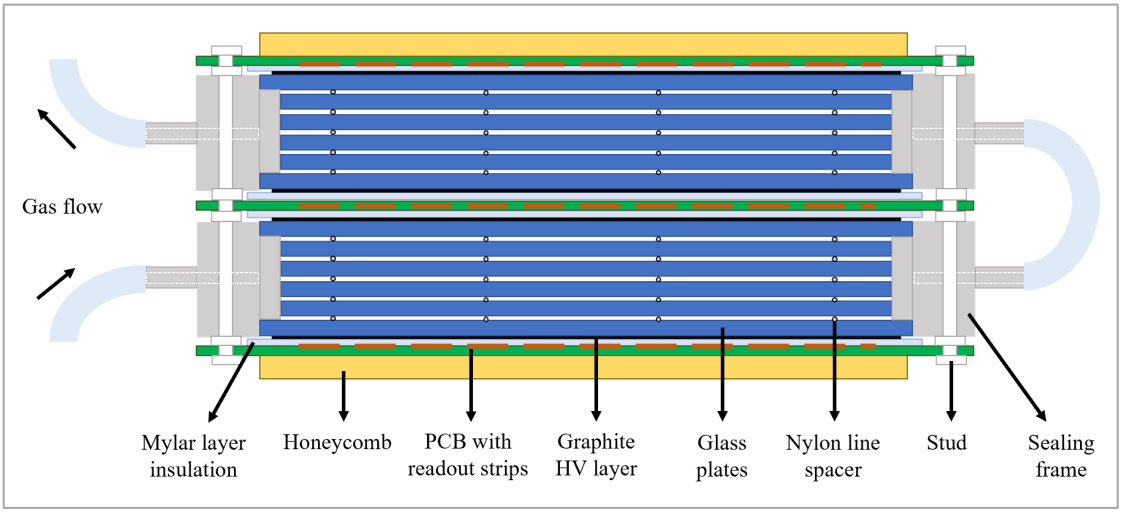

Figure 4.36: The schematic view of self-sealed MRPC

8.1.1 ToF-system based on the MRPC

The required time resolution for SPD is better than 70 ps while the efficiency of particle registration at high rate (few kHz/cm2) should be above 98%. Based the experience of building similar systems in such experiments as ALICE [402], HARP [403], STAR [404], PHENIX [405] and BM@N [406], a glass multi-gap Resistive Plate Chamber could be used as base time detector. For example, the ToF-700 wall in the BM@N experiment, placed at a distance of 8 m from the target, provides one the p/K separation up to 3 GeV/c and p/K separation up to 5 GeV/c under the assumption that the time resolution of the start timing detector is <40 ps. As we know, the time gitter of MRPC should be correlated with width of gas gap. In order to study the intrinsic time resolution of MRPC, a 32-gap MRPC with 0.128mm of gas gap was developed. The structure is shown in Figure 4.37 [2]. 6 readout strips with 1 cm pitch are configured on the PCB sheets. Five PCBs are required in this design. The cathode and anode signals are transmitted through differential cables. During the preliminary cosmic ray test, the high-performance Analog Frontend Electronics (AFE) and the Lecroy oscilloscope (10GHz pulse sampling) were used. The crossing time of a signal is determined when setting a fixed threshold and it is related to the amplitude of the signal. The time spectrum of the difference of two MRPC is shown in Figure 4.38. It can be seen the time resolution of each MRPC is 16.4ps.

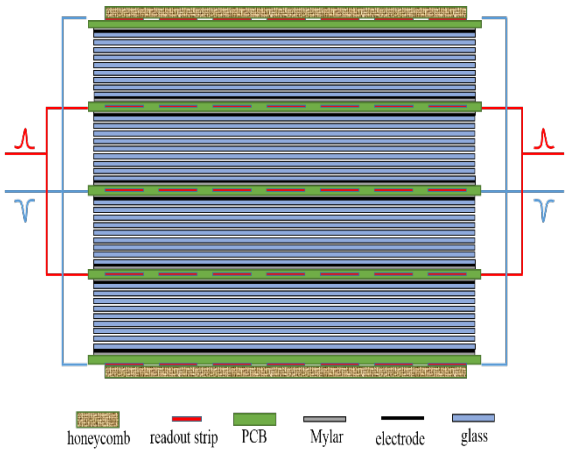

Figure 4.37 Schematic picture of the 32-gap MRPC

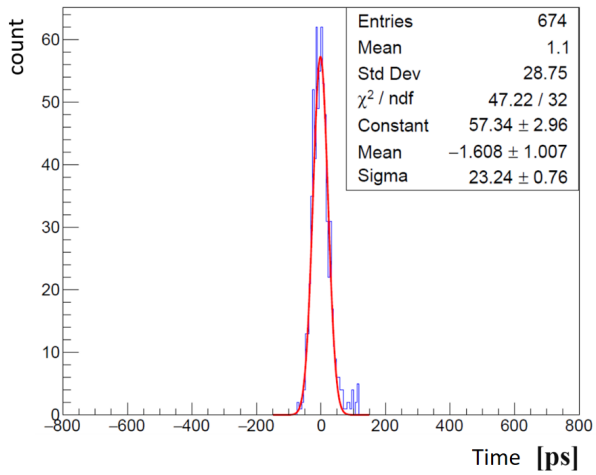

Figure 4.38 The time distribution and resolution results of the cosmic test.

8.1.2 Advantage of self-sealed MRPC

The choice of the working gas mixture for MRPCs has always been an important topic. It should allow the MRPC detector to perform successfully and stably for different purposes, and however, be eco-friendly. This indicates that the gas mixture should have a low ozone depletion power (ODP) and global warming potential (GWP). The tetrafluoroethane currently used in MRPCs is ozone friendly but with a GWP about 1430 (the reference GWP of CO_2 is 1). Therefore, a lot of research has gone into looking for possible replacements. Among the possibilities, HFO-1234ze with a GWP of 6 is one of the most popular candidates and tests of gas mixtures based on it are ongoing.

Another reasonable approach is to reduce gas consumption or recycle gas. The CSR external target experiment (CEE) in Lanzhou, China, will adopt a sealed technology of MRPC to construct the ToF system. The MRPC detector, shown in Figure 4.36, is sealed by gluing an integral 3D-printed frame and the outermost electrodes together. It can operate stably with a gas flux of 4 ml/min, which is extremely low compared to that when MRPCs placed in a sealed box.

8.1.3 TOF related electronics

A very important part of the high performance time-of-flight system is readout electronics. For the full exploitation of the excellent timing properties of the Multigap Resistive Plate Chamber, front-end electronics with special characteristics is needed. The signals from MRPCs must be amplified as fast as possible without lossless. Leading times of the signal must be digitized and measured with accuracy much better than the time resolution of the detector. Readout electronics for the MPD-TOF will consist of the front-end electronics (FEE) and data acquisition system (DAQ).

In order to maximize the time performance of MRPC, the FEE should be with high band width and low time jitter, the time digital should be also with low jitter. So the readout of MRPC can be done with the following two technology [3].

8.1.3.1 Fast amplifier + pulse shape analyzer

As we know, the time jitter of high sampling rate pulse shape analyzer is very low, for example the time jitter of DRS4 is usually less than 5ps. The time jitter of high band width fast amplifier is also low. The schematic diagram of USTC fast amplifier is shown in Figure 4.39. It consists of eight channels and the time jitter is around 4ps. The schematic diagram of DRS4 based pulse shape digitizer is shown in Figure 4.40.

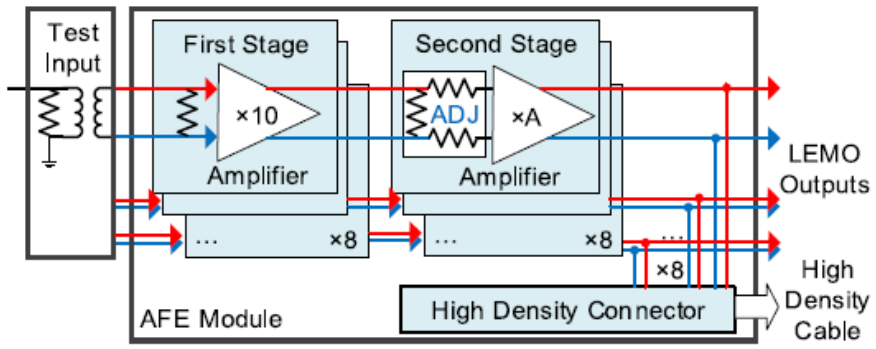

Figure 4.39 The skematic diagram of USTC fast amplifier

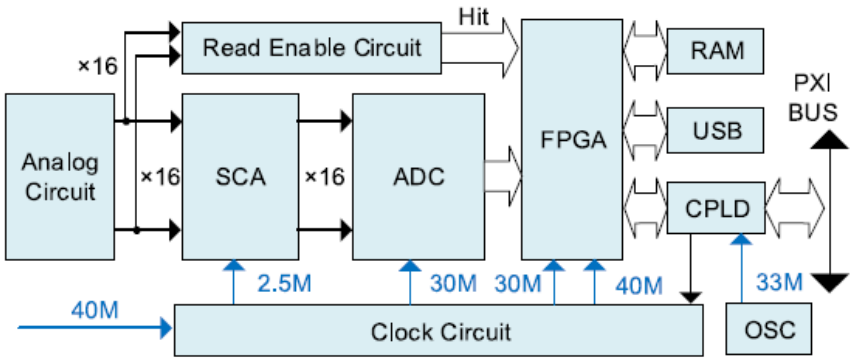

Figure 4.40 The schematic diagram of pulse shape digitizer

8.1.3.2 Fast amplifier and discriminator + TDC

Another soultion of TOF readout is fast amplifier and discriminator + TDC. This technology like used in the TOF ALICE. Such electronics is commercial and convenient for our TOF system. Typical amplifier are NINO ASIC and PADI ASIC. The NINO combines a fast amplifier, discriminator and stretcher.The NINO ASIC had to satisfy the following requirements: differential input; optimized to operate with 30-100 pF input capacitance; LVDS differential output; output pulse width dependent on the charge of the input signal;fast amplifier to minimize timejitter (a peaking time less than 1 ns); threshold of discriminator adjustable in the range 10 –100 fC; eight channels per ASIC.

Main features of the NINO ASIC are shown in Table 8.1.

Table 8.1 NINO ASIC specifications table.

Parameter	Value
Number of channels	8
Peaking time	1 ns
Supply voltage	2.5 V
Power consumption	27 mW/ch
Input signal range	30 fC – 2 pC
Noise (with detector)	< (2.5 – 5)×10^3 e- rms
Discriminator threshold	10 fC to 100 fC
Differential input impedance	40 Ω < Z_{in}< 75 Ω
Timing precision	<10ps jitter
Outputs	LVDS

The LVDS output from amplifier has to be sent to TDC to get the arriving time of particle. TDC digitize the leading edge and trailing edge of LVDS signal. The digram of FPGA TDC can be shown in Figure 4.41.

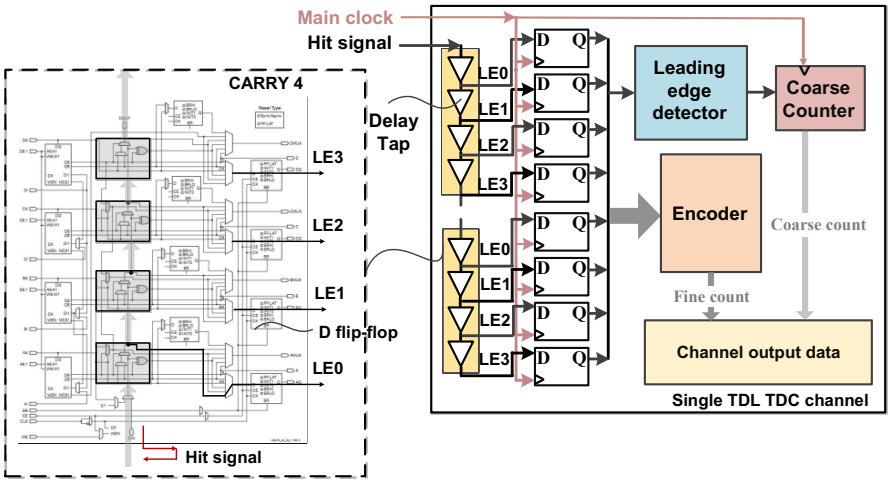

Figure 4.41 The skematic diagram of FPGA TDC

References

1. Botan Wang, Xiaolong Chen, Yi Wang, et al. Appl. Sci. **2021**, 11, 4722. https://doi.org/10.3390/app11114722
2. Yi Wang and Yancheng Yu. Appl. Sci. 2021, 11, 111. https://dx.doi.org/10.3390/app11010111
3. Jinxin Liu, Lei Zhao*, Liujiang Yan, Zhenyan Li, Shubin Liu, Qi An, "Design of a prototype readout electronics with a few picosecond time resolution for MRPC detectors", Nuclear Inst. and Methods in Physics Research, A, Vol. 925, May 2019, pp. 53-59.
4. J Wang, L Zhao.et a;. IEEE Trans.Nucl.Sci. 58 (2011) 2011-2018

Time of Flight System for SPD

List of authors: A.Semak, E.Ladygin, S.Nagorniy

1 ToF-system based on a MRPC

The newest SPD detector has to have a good time-of-flight (TOF) system. The purpose of the TOF system is to do π/K and K/p separation in the momentum range up to a few GeV/c. The radius of the TOF barrel is 108 cm only. This size dictates the requirement for the time resolution of the TOF to be better than 60 ps. This time resolution allows to separate π/K and K/p up to about 1.2 GeV/c and 2.2 GeV/c respectively.

MC calculations show that in the barrel part of the TOF the charged particle flux is about 100 Hz/cm^2. The particle flux in the end-cap part rapidly increase up to 1 kHz/cm^2 when approaching to the ion pipe. It must be taken into account that the actual radiation flux are always higher. Such conditions make it possible to build a TOF system based on the traditional MRPK with floating electrodes. For example [1], a 12 gaps MRPC made of 0.55 mm glass allows to obtain a time resolution of 60 ps and a efficiency above 98% at a background particle flux of 500 Hz/cm^2. However, due to a spread in the performance of individual MRPCs and front-end electronics the resolution of the TOF system is always worse than that of a separate chamber. Therefore, for SPD, it is proposed to use an MRPC with an independently distributed potential over gas gaps. (It is similar to how it is done for a multi-gap ceramic PPC) As will be shown in the sub-section 4, a high time resolution of about 30 ps can be achieved for these detector. To ensure the best rate capability MRPCs should be made of thinner glasses.

2 Layout of MRPC TOF

Overall dimensions of one MRPC are 480×415×16 mm. The detector is composed of 192 chambers: 144 and 24 chambers for the barrel and each end-cap respectively. Adjacent MRPCs will be positioned in such a way to create an overlap of 1 strip at the edge of the active area. The MRPC thickness is about 0.09 of radiation length (X_0) excluding chamber frame.

Each MRPC equipped with 16 readout strips. Strips are 20 mm wide and 400 mm long. The strip pitch is 21 mm. Taking into account expected event rate is about 3 MHz and the barrel charge particle rate is ~100 Hz/cm^2, for a single event, the strip double hit probability can be 0.003. This value could be sufficiently low for the DAQ system.

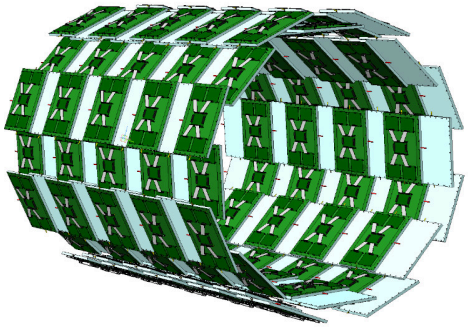

Fig. 1a: barrel TOF layout

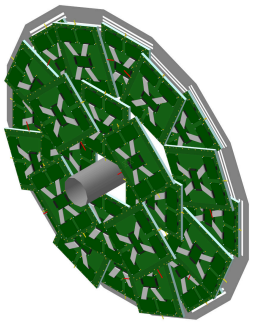

Fig. 1b: end-cap TOF layout

Figure 1 shows the possible arrangement of MRPCs in the TOF detector. The barrel consist of 16 overlapping rows of MRPCs. Each row contained 9 chambers. Each end-cap wall consist of 24 MRPCs.

3 MRPC's design and assembling.

In order to increase the high-speed performance of MRPC is decided to make new chamber using of glass plates with 0.33 mm thick. This should reduce the time of charge dissipation inside a glass. The thinner electrodes allows for the higher rate capability. This last condition is the most critical for the successful application of the TOF system. The schematic cross section of a MRPC is shown in figure 2. It is consists of two identical gas gaps stacks with anode strip readout plate in between. In a 10-gap MRPC all electrodes are at a fixed potential from an external HV source. Using such structures we expect to increase high-speed performance more than 1 kHz/cm^2 with time resolution better than 30 ps.

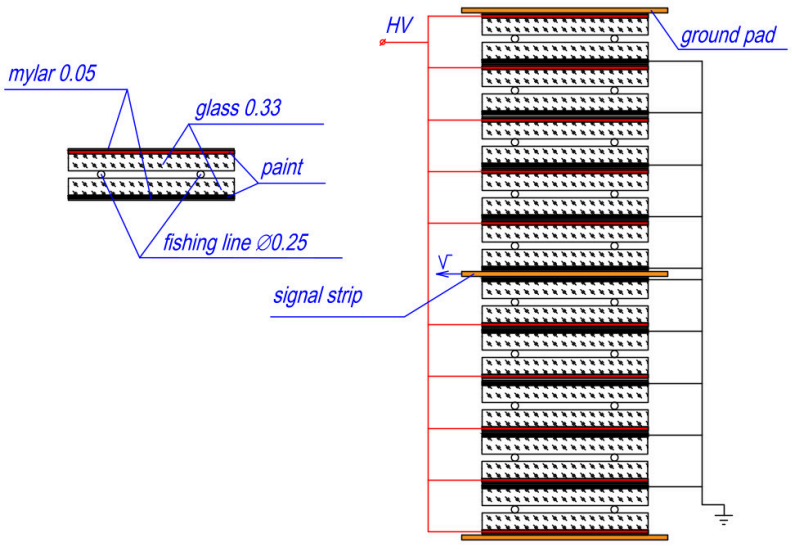

Fig. 2: the schematic cross-section of the new MRPC.

Each stack is formed by 10 glass plates with the $3x10^{12}$ Ω×cm bulk resistivity. The gas gap in between glasses is 0.25 mm. The gap is fixed by spacers which is a usual fishing-line. Fishing-lines ran directly through the RPC working area. Graphite conductive coating with surface resistivity of ~1 M/square is painted to outer surfaces of glass plates to distribute the high voltage and its separate ground.

The anode readout strips plate is a one-sided printed PCB with the thickness of 0.1 mm. The thickness of the PCB copper is 35 microns. Signals are taken from the both ends of anode strips. The entire MRPC assembly is put into a gas-tight box. The bottom of the box is made of a double side PCB (motherboard) with a thickness of 2.5 mm. The side frame of the box is made of a aluminum profile. The top of the box is closed by a 1.5 mm aluminum lid.

Figure 3 shows four stage of the assembling. The left photo show the box with one glass and fishing lines. In the middle photo there is one stack of gaps covered by the strip PCB. In the right photo there is almost assembled chamber. It is without an aluminum lid yet. There is copper ground pad on the top. The last photo shows how the fishing lines are mounted.

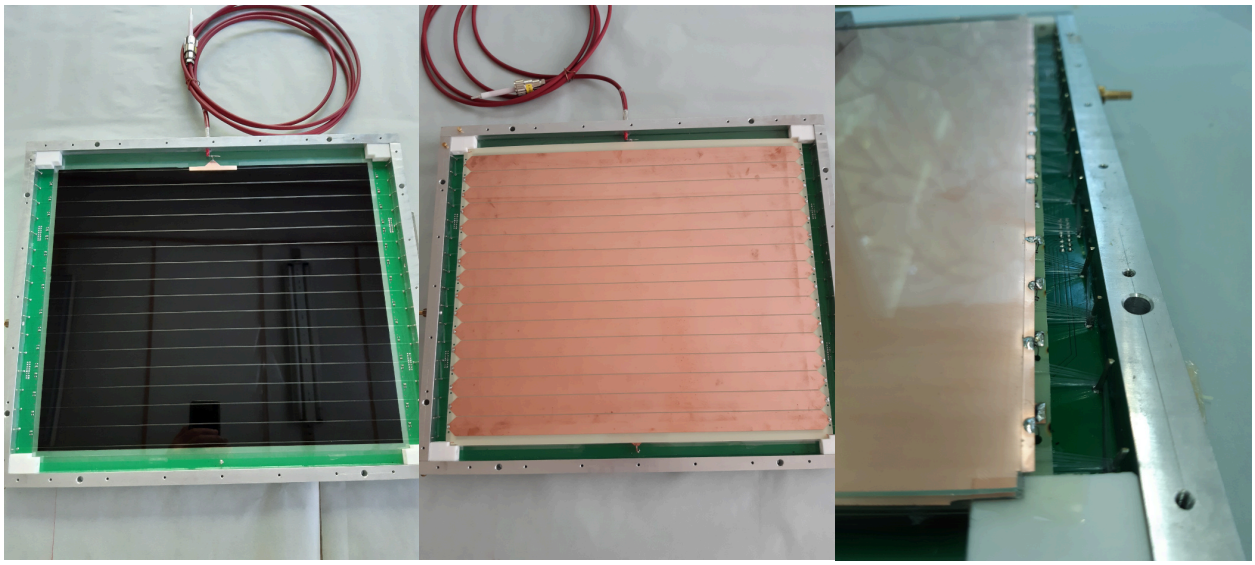

Fig. 3: an assembling of the MRPC module is shown in few steps.

4 MRPC prototypes test results.

During 2019 -2020 MRPC prototypes were investigated. A series of measurements were carried out both with cosmic rays and with a muon beam at the IHEP U-70 PS. The prototypes were made of glass with a thickness of 0.55 mm. They were equipped with strips 10 mm wide and 150 mm long. Otherwise, their structure is similar to that described in the sub-section 3. The advantage of the ‘fixed potential’ construction over the floating electrodes MRPC is shown in figure 4. The ‘fixed potential’ construction exhibits the weaker resolution dependence on the applied voltage. The full operating voltage in the last case is 5 times less. The best values of

resolution reach about 45 ps. This result was obtained with cosmic rays. During the data processing, the TOT method was used. That is correction of the chamber response time by the width of the detected signal.

Figure 5 shows the time resolution and efficiency of two chambers measured with a muon beam with a good statistical accuracy. A time resolution of about 45 ps and an efficiency of above 99% were obtained.

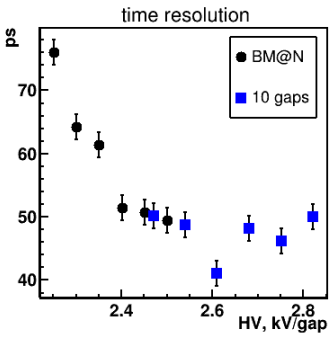

Fig. 4a.

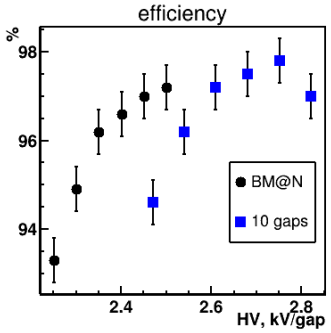

Fig. 4b.

Cosmic test results: the time resolution (a) and efficiency (b) for BM@N and 10 gaps MRPCs. The BM@N MRPC has the 0.22 mm gas gap. 10 gaps MRPC has the 0.25 mm gas gap.

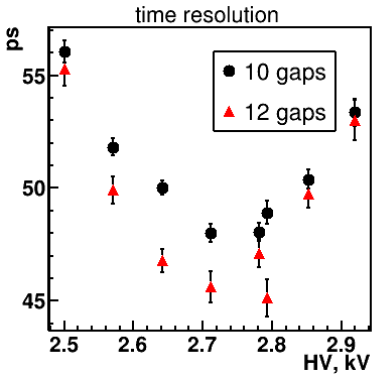

Fig 5a.

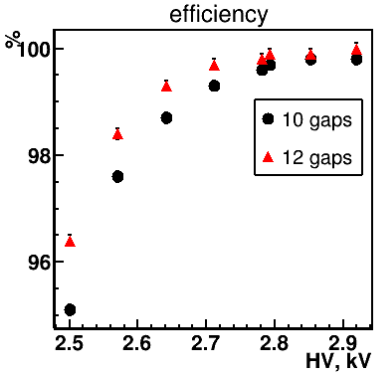

Fig. 5b.

Beam test results: the time resolution (a) and efficiency (b) for 10 and 12 gaps MRPCs. All MRPCs have the 0.25 mm gas gap.

An alternative to the TOT method can be the constant fraction (CF) method. Its essence is to determine the appearance time of the signal by using a transformation of its leading edge. In order to correct the leading time the TOT method uses the trailing edge of the signal which is influenced by secondary processes in the gas discharge. Therefore, the CF method should be more accurate. In our case, it is not supposed to use the classic CFD solution. Initially, the signal from the MRPC strip must be amplified. The slew rate of the amplified signal will be definitely slower than that of the input signal. After amplification the signal is fed to the CF transformer. The delay for the transformer is selected from the experimental data. The task of the method is to find the zero crossing time.

Figure 6 shows two examples of a waveform after the CF transformer. Figures 6a and 6b corresponds to a 200 ps and 250 ps delay respectively. Wave forms obtained using a Tektronix DPO4104b oscilloscope. The oscilloscope time step is 200 ps. A prototype of a PADI amplifier developed at GSI was used as a pre-amplifier.

By associating the zero crossing point with the MRPC response time, a distribution of the difference between the response times of two chambers when the same particle passes through can be obtained. The resulting histograms are shown in figure 7. The narrowest distribution corresponds to a delay of 250 ps and has a sigma of 43 ps. This sigma corresponds to the time resolution of each of chambers about 30 ps. These data were obtained at an operating voltage of 2.75 kV. All presented data are taken for TFE/*i*-C4H10/SF6 = 85/10/5 gas mixture.

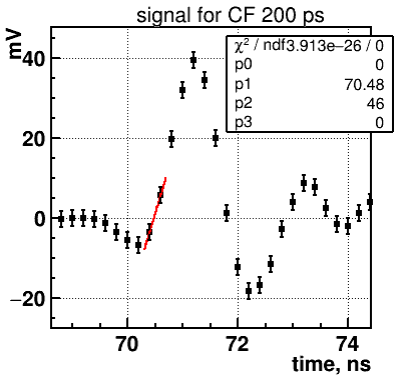

Fig. 6a.

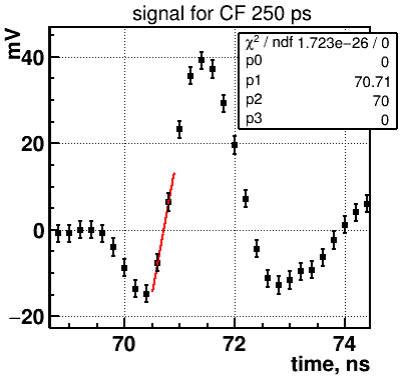

Fig. 6b.

Wave forms of MRPC signal after CF transformation with 200 ps (a) and 250 ps (b) delay and multiplication factor of 2.

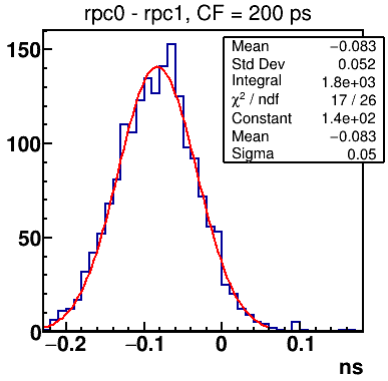

Fig. 7a.

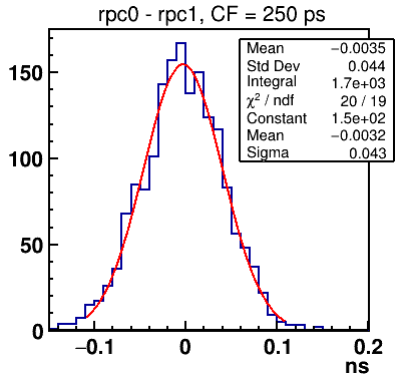

Fig. 7b.

Response time difference of 10 and 12 gaps MRPCs for 200 ps (a) and 250 ps (b) CF delays.

With the CF method the value of the time resolution of 10 gaps MRPC has been improved to 30 ps.

5 FEE for MRPC's

A number of FEE channels for the TOF are 6144. To obtain the best time resolution, it is proposed to use the specially adapted for MRPC signals the CF method. In order to simplify the implementation of the CF method, it is assumed to use a two threshold discriminator. Triggering this discriminator creates two time marks (t_1 and t_2) for the low and high thresholds. A offline

processing of this marks allow to calculate the MRPC response time (t_0 that is ‘zero crossing’) by the formula:

$$t_0 = \frac{k \cdot t_1 - t_2}{k-1} + const \quad ,$$

where ‘k’ is the ratio of high and low values of the threshold and the ‘const’ is a arbitrary time shift. The parameter ‘k’ must be set with the high accuracy by the circuitry solution.

The CF FEE channel consist of a fast amplifier (~ 1GHz bound width), CF transformer and two threshold discriminator. Each FEE board has 8 analog inputs and 16 LVDS outputs. The figure 8 represent the placement of the electronics on the MRPC module. The number 1 denotes the MRPC itself. The CF front-end board is designated by number 2. Each chamber is equipped with mounted on the motherboard four CF front-end boards. CF boards are connected by short cables with one TDC. TDC is also mounted on the module. The desired TDC time quanta should be 10 ps.

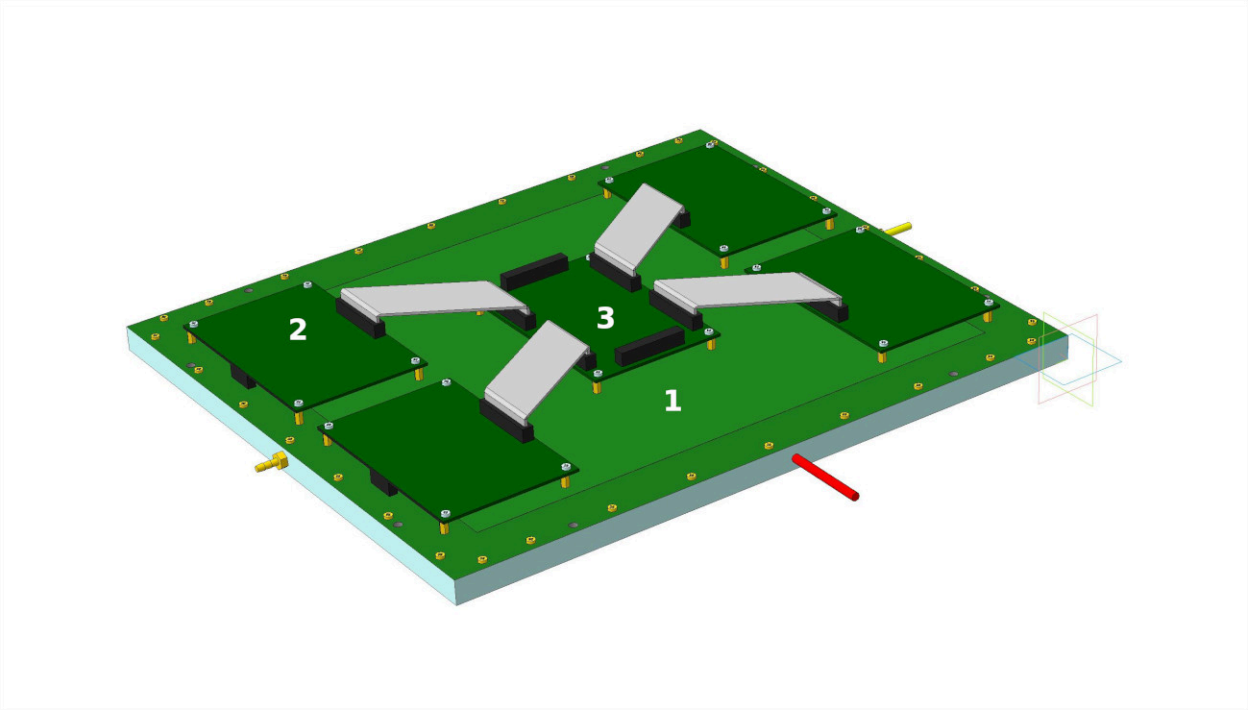

Fig. 8: the schematic layout of MRPC equipped with FEE. Mark 1 is MRPC, 2 is two threshold CF discriminator and 3 is TDC.

References.

[1] N.A. Kuzmin et al., Nuclear Inst. and Methods in Physics Research, A 916 (2019) 190–194.

1 Beam-beam counters

Two Beam-Beam Counters (BBCs) are planned to be located just in front of the PID system in the end-cups of the SPD setup [1]. The detector should consist of two parts: the inner and the outer one, which are based on different technologies. Schematic view of the SPD Beam-Beam Counter is given in Fig.1. The inner part of the BBC will use fast segmented MicroChannel Plate (MCP) detectors and should operate inside the beam pipe, while the BBC outer part will be produced from fast plastic scintillator tiles.

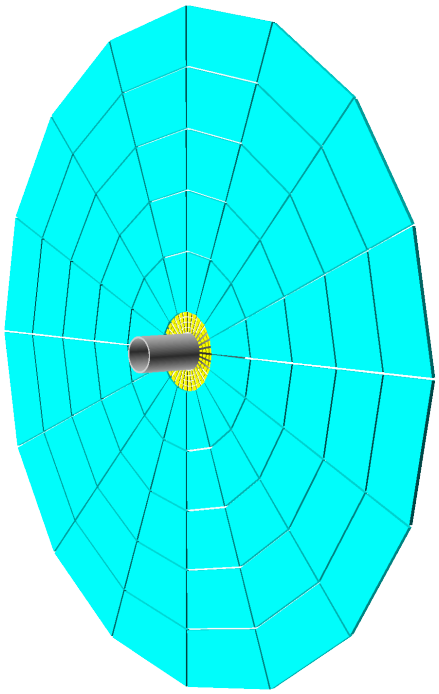

Figure 1: Schematic view of the SPD Beam-Beam Counter with the inner and the outer parts.

The inner part covers the acceptance 30÷60 mrad and should be separated into 4 layers consisting of 32 azimuthal sectors. The outer part covering the polar angles between 60 and 500 mrad will be divided into 5 or 6 concentric layers with 16 azimuthal sectors in the each of them. The final granularity is the matter of further optimization for the entire energy range of collisions at SPD. The concept of the BBC is shown in Fig.2. The magenta part represents the MCP detector while the internal layer of the outer part is shown in red.

The main goals of the Beam-Beam Counters are: i) the local polarimetry at SPD basing on the measurements of the azimuthal asymmetries in the inclusive production of charged particles in the collisions of transversely polarized proton beams, ii) the monitoring of beam collisions and iii) participation in the precise determination of the collision time t_0 for events in which other detectors can not be used for that (for instance in case of elastic scattering).

Another important goal of the BBCs is fast preselection of different types of events for monitoring purposes. The Monte Carlo simulation shows that in the p-p collisions at $\sqrt{s}$=27 GeV at least one BBC should have a signal in 79% of events (51% of events has a signal in the both BBCs). However, for the hard processes, in 97% of events the

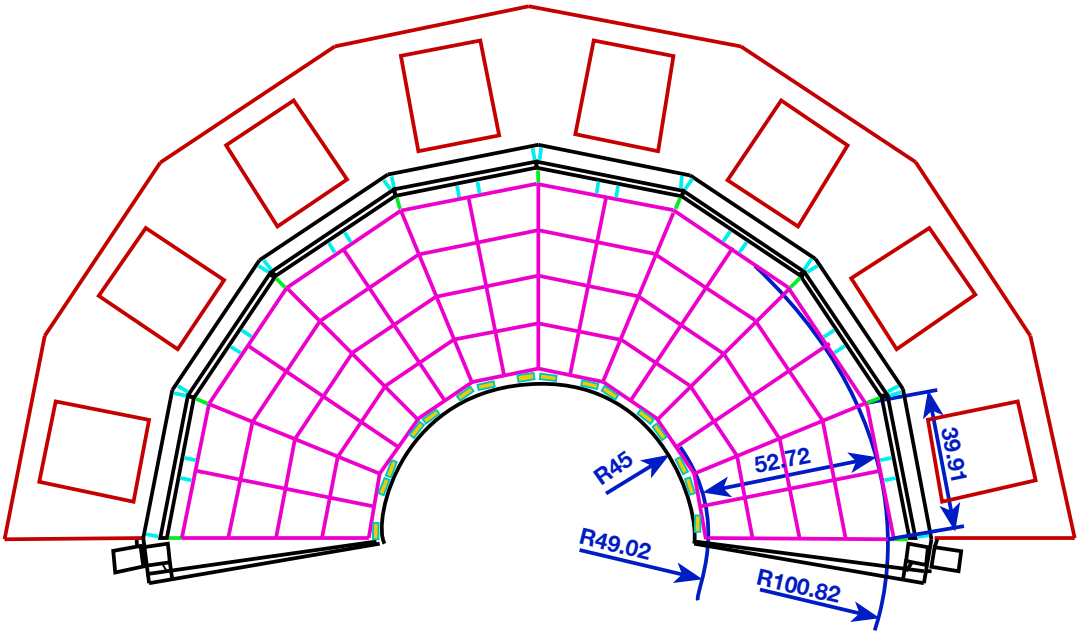

Figure 2: Beam-Beam Counter: azimuthal and polar angle segmentation [**?**]. All dimensions are in millimeters.

only one BBC will be hit, while hits for both counters could be expected in 68% of cases. Therefore, the requirement of the BBC signals allows one to preselect hard processes.

1.1 Inner part of the BBC: MCP

The concept of the MCP-based Fast Beam-Beam Collision (FBBC) monitor is described in details in [**?**]. Two ring beam-beam collision detectors (FBBC-left and FBBC-right) could be located inside the vacuum beam line together with two 2D position-sensitive beam imaging detectors (BPMs) (see Fig. 3). The FBBC uses the concept of the isochronous multi-pad fast readout and the precise timing determination of short ($\sim$1 ns) MCP signals. Individual fast readout of pads is being also considered. New MCPs with the improved characteristics, such as small diameter (8μm) channels, low resistivity (100$\div$500 MΩ), high gain ($\sim 10^7$), short fast rise-time ($\sim$0.8ns) signals, could be used.

Fig.4 shows a typical MCP signal from the detector prototype. The colliding beams pass through the central opening of the MCP, and the outer edges of the MCP capture secondary particles flying a definite distance from the interaction point. The signals are recorded at the sectorized cathode and their arrival times are digitized along with the multiplicity information. The main feature of the new MCP is a high secondary emission coefficient and fast fronts of the output signal. The new MCPs have a fast leading edge and high gain.

The feasibility of the event-by-event monitoring of the beam-beam interactions at NICA is confirmed both by the previous developments of the UHF-UHV technology and by the beam tests (at JINR and CERN) [**?**, **?**, **?**] of the prototype detectors and electronics, as well as by the in-lab tests of new 8-channel MCPs with the improved characteristics.

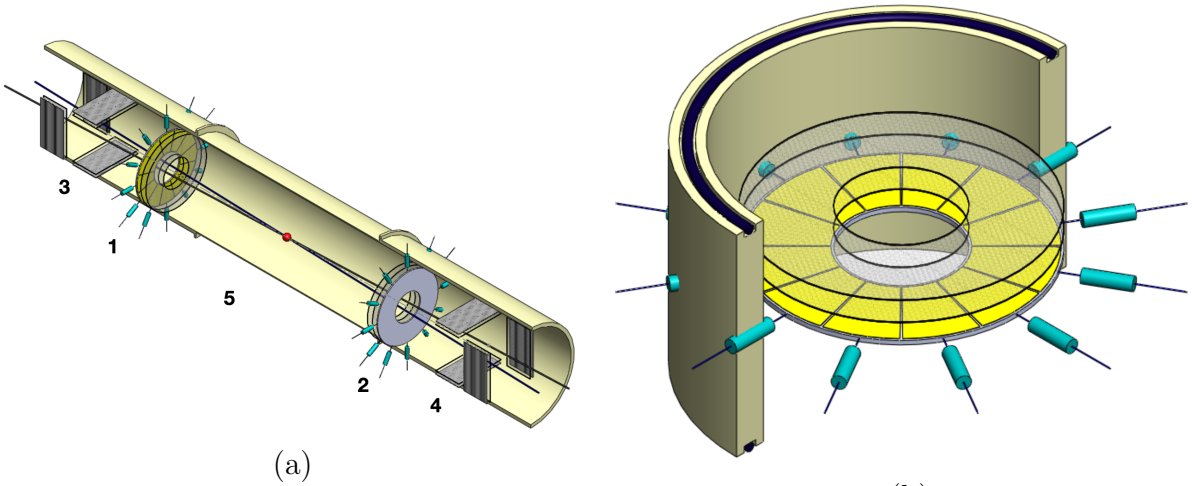

(a) (b)

Figure 3: (a) Possible layout: the Fast Beam-Beam Collision (FBBC [**?**]) monitor composed of MCP discs (1 and 2) in combination with the Beam Position devices (BPM) (3 and 4) are situated symmetrically to the Interaction Point (5) inside the vacuum beam pipe of the NICA collider. (b) Compact module of the Fast Beam-Beam Collision Monitor (FBBC) based on circular MCPs. Sector cathode readout pads and two MCP setups are embedded into a separate flange with a hermetic 50-Ω signal and HV feedthroughs (the latter are not shown).

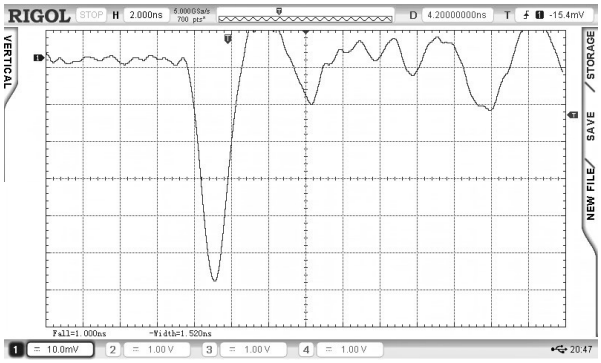

Figure 4: A typical MCP signal the detector prototype.

1.2 Outer part of the BBC: scintillation tiles

The scintillation part of the BBC will consist of tiles viewed by the SiPMs. The measurement of the signal amplitude is required for time-walk correction to improve the time resolution.

1.2.1 First R& D results for FEE

With a single-channel prototype of the detector we will be able to measure the amplitude using the developed FEE based on the Time-over-Threshold (ToT) technique. This technique is a well-known method that allows us to measure the energy deposited in the material by reconstructing the given property of the output current pulse the total charge

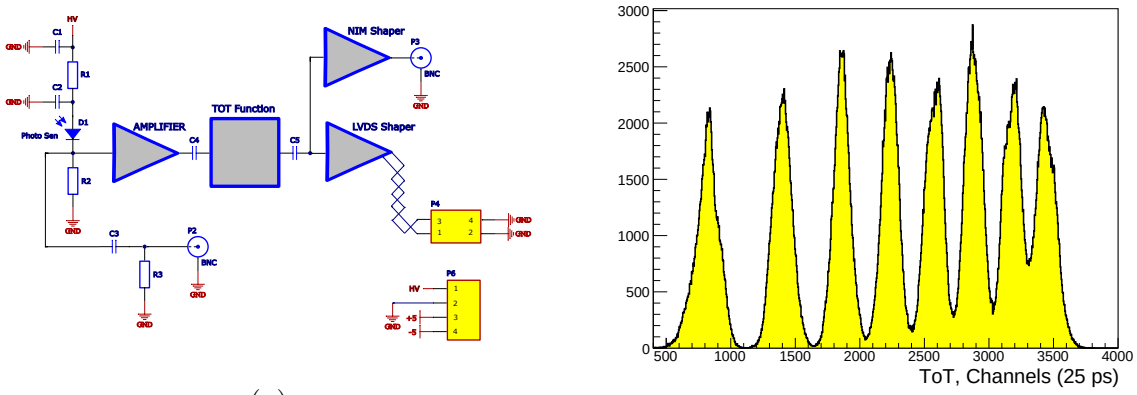

(a) (b)

Figure 5: (a) Schematic view of the front-end electronics with a ToT function, (b) Distribution of the ToT for LED signal.

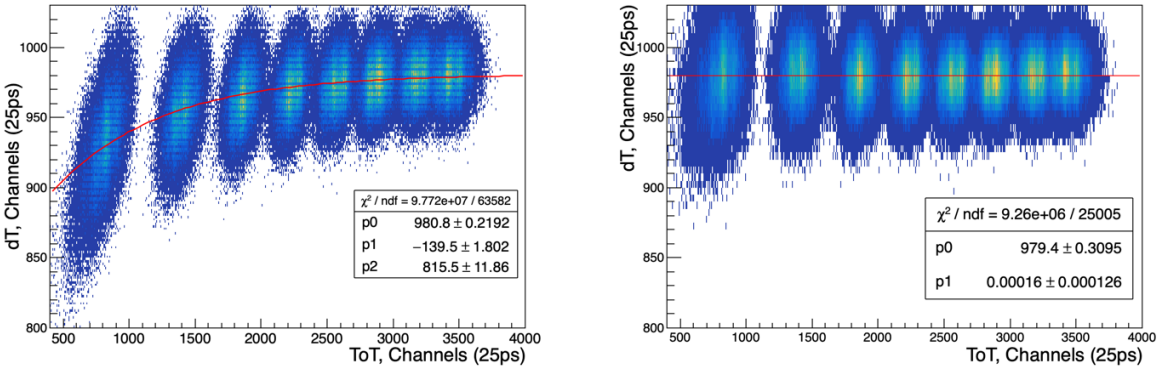

(a) (b)

Figure 6: (a) dT $(T_{SiPM1} - T_{SiPM2})$ correlation on the ToT. (b) Result after the time-walk correction for the dT $(T_{SiPM1} - T_{SiPM2})$ correlation on the ToT.

collected, the pulse amplitude, etc. The ToT method converts the signal pulse height into a digital value in the early stage of the FEE, which greatly simplifies the system in comparison to analog detectors with serial readout through ADCs. The measurement of the ToT is composed of two measurements of time for the signal going above (leading) and returning below (trailing) the given threshold. The first version of the prototype includes a power supply and electronics (Fig.5(a)) made on a separate PCB. This PCB is used for each cell of the SiPM. The power supply for the SiPM provides a voltage of up to 65 V with an individual channel adjustment within 0-10 V, manual tuning, and a built-in voltmeter for the voltage monitoring It is possible to connect eight cells simultaneously. The amplifiers used for that do not change the leading edge of the signal. This allows us to get a time stamp of the event. Afterwards, the signal is integrated and transmitted to the comparator.

The response of the Hamamatsu S12572-010P SiPM [2] with the FEE to the LED has been studied. The electrical signal from a LEMO output of the LED was used as a trigger. The illumination was performed by uniform light in a light-isolated box. In

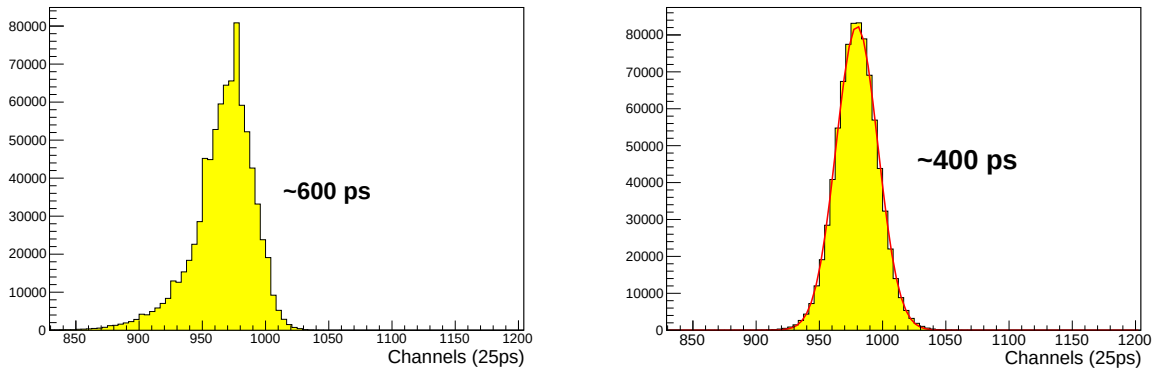

(a) (b)

Figure 7: (a) dT ($T_{SiPM1} - T_{SiPM2}$). (b) Result after the time-walk correction for the dT ($T_{SiPM1} - T_{SiPM2}$).

addition to the ToT information (Fig.5(b)), the time stamp of the event for each SiPM cell was investigated. The distribution (Fig.6(a)) shows the correlation of these values and that the signal in the region of small amplitudes comes later in time. This is due to signal latency (the so-called time-walking effect). This delay occurs due to the difference between the time when a photon or a charged particle passes through the detecting element and the time when the electronics registers this signal. This leads to deterioration in the time resolution. After performing the correction (see Fig.6(b)), the time-walking effect has been removed [3].

The time resolution was defined as the RMS and was approximately 600 ps. Taking into account the non-Gaussian waveform (Fig.7(a)) and the fact that the time resolution is not the maximum allowed for this type of the detector, the time-walk correction has been applied. The most important result of the correction was a time resolution of approximately 400 ps (Fig.7(b)), which is 1.5 times better than the resolution before the correction.

Therefore, the first version of the front-end electronics based on the Time- over-Threshold method was tested with LED. After the time-walk correction, the time resolution improved up to 400 ps. Taking into account the SiPM suboptimal for precise time measurements, the result was promising. Further development of the FEE with a ToT function allows to use standard TDCs for timing measurements.

1.2.2 Description of the detector prototype and test equipment

Since the concept of the BBC outer part is highly granular scintillation tiles with SiPM readout (SiPM), a prototype of a scintillation detector was developed (see Fig.8) with 2 different types of FEE. Both types are based on Hamamatsu SiPM readout (S12572-010P) [2].

The initial version of the prototype detector includes a 40-cm plastic scintillator and ten channels of electronics (right panel in Fig.8). In order to increase the light collection, the scintillator is wrapped in a mylar film. Holes are made in the film on the upper face of the scintillator for studies related to the position of the source of calibrated light pulses (LED): in the center; in increments of 5 cm in both directions; and several additional

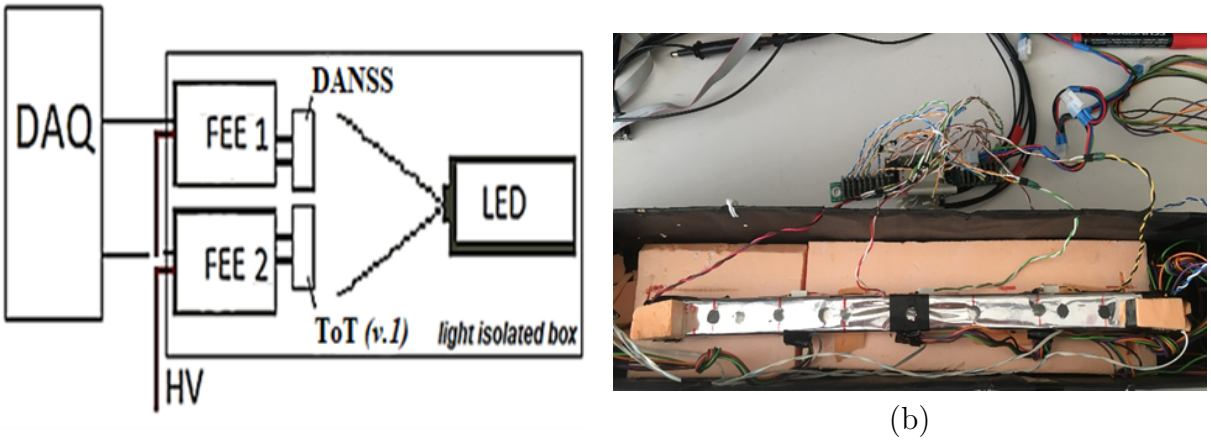

(a) (b)

Figure 8: Schematic view of tests without a scintillator (a); prototype view (b).

holes on each side. Along the side face there is a similar version of electronics with SiPM in the holes: in the center; and in increments of 10 cm in both directions. At the ends of the scintillator, one channel of each electronics option was located. In the case of electronics with the ToT function, the second version of the boards was used. This version is characterized by comparator stability and extended operating range.

Testing of the electronics (right panel in Fig.8) and the prototype detector was carried out in a light-insulating box, where the temperature during the measurements was 27.1±0.4 ^{o}C. As a light source, an LED was used, made in the form of a separate board with a synchropulse from the LEMO output [4]. This synchropulse was used as a trigger for a VME-based data acquisition system [5]. The system included the FVME-V2.0 controller, digitizing modules TQDC16 and TDC32 and the trigger module TMWR [6]. The data collected was processed in the ROOT software package.

1.2.3 FEE used for detector prototype

First type of the used electronics for the detector prototype SiPM readout is the second release of the FEE based on the ToT method described above. The single-channel electronics are made on a 4×2.5 cm^2 printed circuit board shown in Fig.9(a). As it was described above the ToT method itself consists of two time measurements - the passage of a negative signal below (leading) and the return above (trailing) a given threshold, and allows to measure the charge along the width of the electric pulse. In addition, amplifiers were used that did not change the leading edge of the signal. The signal after the amplifier is integrated and transmitted to the comparator, from where it is output to the reading electronics via the LVDS interface. Thus, thanks to the developed electronics board, we have the opportunity to get a timestamp of the event and measure the charge. The power is supplied by a power supply (PS) with the possibility of simultaneous connection of up to eight channels of electronics. The PS contains a push-button interface, a display and a built-in voltmeter. The bias voltage consists of a constant (38/52/67 V) and a part adjustable for each channel (in the range from 0 V to +10 V).

Another FEE option for a prototype detector was the electronics produced by the ITEP group for the DANSS experiment [7]. It has a multi-channel platform created

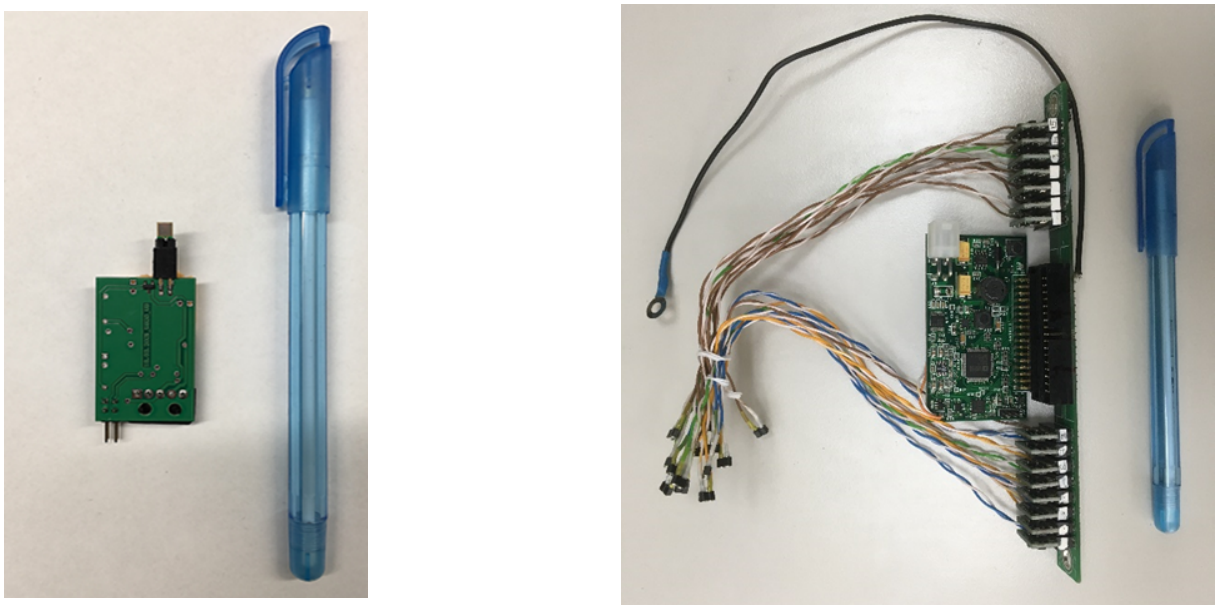

(a) (b)

Figure 9: Single- channel FEE with ToT method board (a); 15-channels FEE board from DANSS experiment [7] (b).

from several printed circuit boards. The first board provides power and communication with the PC via RS-232, and is connected via IDC-34 to a common board on which 15 electronics boards are installed. Power is supplied in a wider range, and consists of a constant (10-65 V) and a bias voltage adjustable for each channel (±10 V). Each 1.7×1.9 cm^2 board contains an offset voltage output for SiPM and an input for the signal. The signal passes through the amplifier and is then output via the IDC-34 connector to the reading electronics. The picture of the 15-channels FEE board [7] is shown in Fig.9(b).

1.2.4 Test results

The SiPM response from a light source for two of electronics was investigated in the presence and absence of a scintillator. Histograms of the time difference at different amplitudes of the LED were obtained and analyzed. Earlier, when testing the first version of electronics with the ToT function [1], it was revealed that the signal in the region of small amplitudes arrives later in time. This is due to the delay of the signal, often called the "time-walking" effect. This effect occurs due to the difference in the moment of time when a photon or a charged particle passes through the detecting element and the moment of time when the electronics register this signal. This leads to a deterioration of the time resolution. In this regard, the method of correction of time spectra described in [3] was proposed.

The proposed correction is relevant when comparing time spectra in the presence and absence of a scintillator. Figs 10 and 11 show the difference in the arrival times of the $T_{SiPM1} - T_{SiPM2}$ signals for the SiPMs placed at the prototype endcups after applying the correction. The distributions were approximated by the Gaussian function, and the time resolution was determined as a parameter of the sigma(σ) Gaussian function. It can be seen from the figures that in the presence or absence of plastic for two types of electronics,

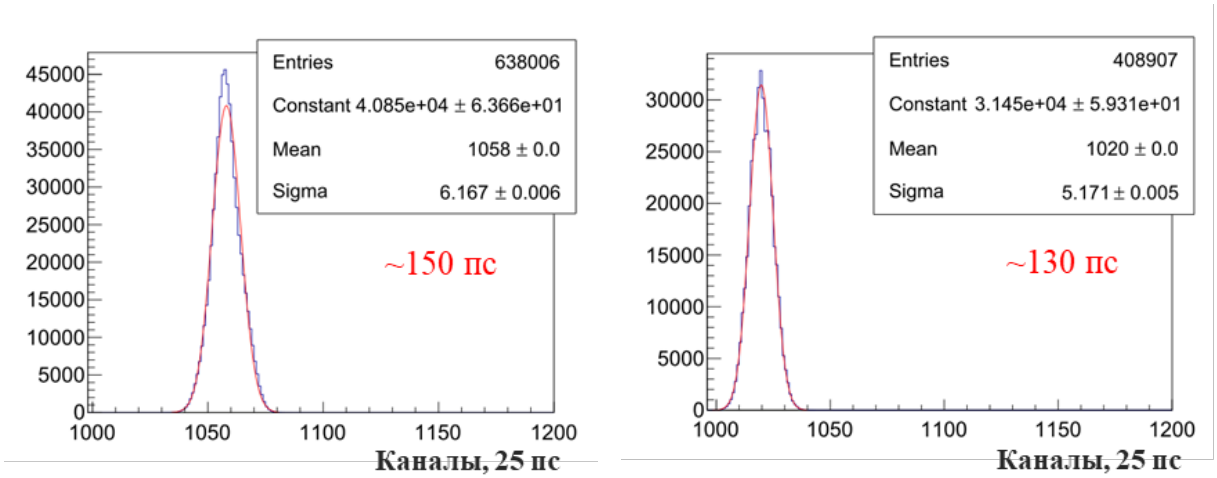

(a) (b)

Figure 10: T_{SiPM1} - T_{SiPM2} histogram after "time-walking" correction for tests of the FEE with the ToT function [8] in the case of: absence of a scintillator (a); presence of a scintillator (a)

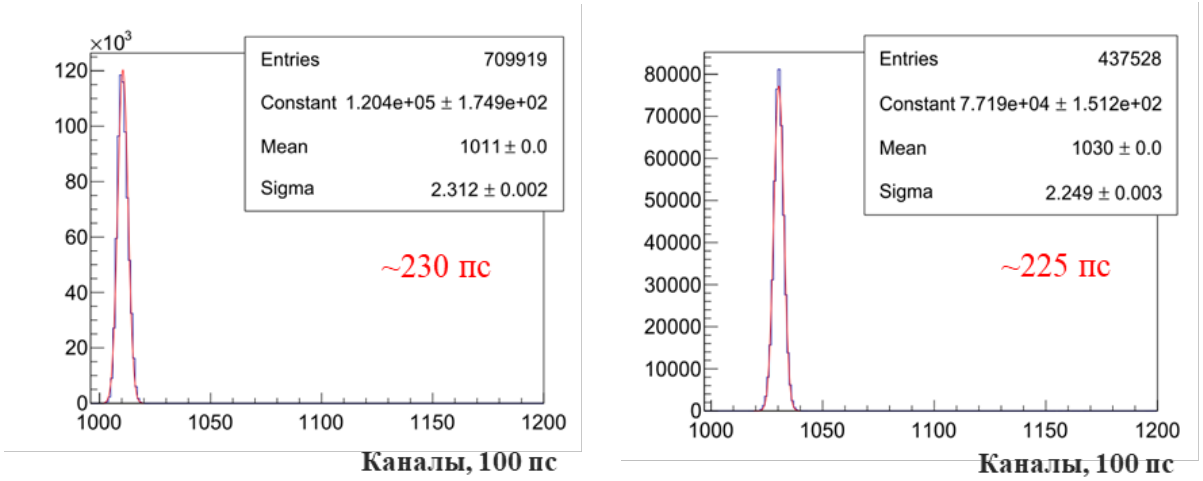

(a) (b)

Figure 11: T_{SiPM1} - T_{SiPM2} histogram after "time-walking" correction for tests of the DANSS exepriment FEE [7] in the case of: absence of a scintillator (a); presence of a scintillator (a)

the time resolution is almost invariable. When comparing the front-end electronics with the ToT function and the DANSS experiment, the time resolution was approximately 130 ps and 225 ps, respectively.

Therefore, the developed second version of the front-end electronics with the ToT function demonstrated good performance during LED tests. Two options of the FEE: with the ToT function and the electronics of the DANSS experiment with SiPM readout manufactured by Hamamatsu (S12572-010P) have been tested. The difference in time resolution for both FEE options was found approximately 40%. A prototype of a scintillation detector was manufactured and tested. The proposed prototype is an important

stage for the development of the BBC subsystem. Given the suboptimality of the SiPM used for accurate time measurements, the result is promising.

References

[1] V.M.Abazov et al., Conceptual design of the Spin Physics Detector, e-Print: 2102.00442 [hep-ex].

[2] Hamamatsu S12572-010P Datasheet,

http://www.hamamatsu.com/jp/en/S12572-010P.html

[3] A.V.Tishevskiy et al., Development of the scintillation detector prototypes with SiPM readout for SPD at NICA, J.Phys.Conf.Ser. 1690 (2020) 1, 012051.

[4] http://hvsys.ru/images/data/news/2_small_1368802824.pdf

[5] A.Yu.Isupov, VME-based DAQ system for the Deuteron Spin Structure setup at the Nuclotron, EPJ Web Conf. 204 (2019) 10003.

[6] https://afi.jinr.ru

[7] I.G.Alekseev et al., DANSS: Detector of the reactor AntiNeutrino based on Solid Scintillator, JINST 11 (2016) 11, P11011; e-Print: 1606.02896 [physics.ins-det].

[8] A.V.Tishevskiy et al., Scintillation detector prototype for Beam-Beam Counter at NICA SPD, In Proceedings of the LXXI-st International conference "NUCLEUS 2021. Nuclear physics and elementary particle physics. Nuclear physics technologies", 20-25 September, 2021, St.Petersburg, Russian Federation.

Micromegas vertex detector for SPD

Aims

According to construction plan, at first stage SPD will operate without silicon vertex detector. This will hit momentum resolution and tracking efficiency substantially. We propose to build relatively simple and cheap vertex detector based on Micromegas technology, which will be used first 2-3 years of SPD operation and will be replaced by MAPS vertex tracker later.

Summarizing, the idea of Micromegas vertex detector (MVD) is to improve momentum resolution and tracking efficiency of main tracking system during first period of data taking, while the main requirement is total cost below 10% of one for silicon vertex detector. MVD will not provide precise secondary vertex reconstruction for long-living particle decay identification and track reconstruction in far forward region.

Principle of operation

Micromesh Gaseous structure(Micromegas), proposed by G.Charpack and Y.Giamatris [1], is a parallel plate counter with dedicated ionization and a amplification gaps separated by fine

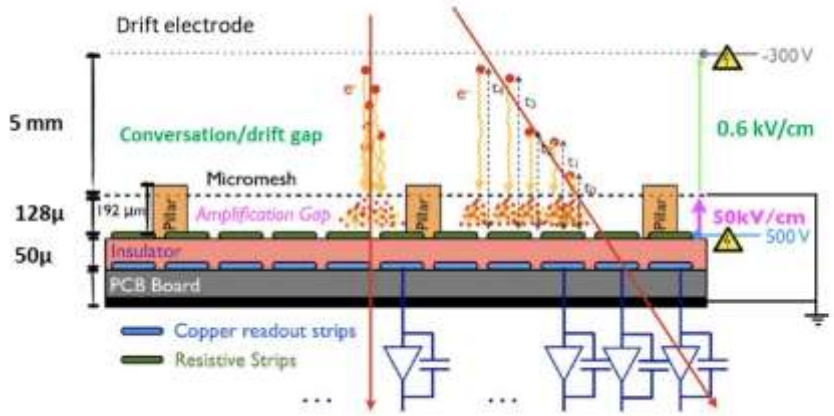

Figure 1. Micromegas detector scheme and operation principles.

mesh(fig. 1,a). Typical thickness of ionization gap is 3-5 mm with drift field applied about 600 V/cm, while amplification gap is about 120µ thick and amplification field exceeds 30kV/cm. High uniformity of amplification gap and, hence, amplification field is ensured by regularly spaced isolation pillars. High-energy particle crossing detector volume produces primary electron-ion pair in conversation gap. Electrons of primary ionization moves toward mesh and pass through it. Due to very high field tension difference between drift and amplification gaps, mesh transparency for primary electrons is about 99%. In amplification gap electron starts avalanche, resulting in final signal about 10^4 electrons. Most of electrons and ions in avalanche are produced near anode, so ions passes almost full amplification voltage before being collected on mesh and produce dominant contribution to signal. Ion collection time for single-cluster avalanche is about 150ns.

To get good space resolution anode plane should be segmented. Usually readout electrodes are shaped as a narrow strips with typical pitch 0.35 - 0.5 mm.

As well as any parallel plate counter, micromegas detector is vulnerable to spark discharge. If avalanche charge exceeds Raethars limit (10^5 – 10^6 electrons depending on gas mixture) avalanche transforms to streamer followed by spark. Fluctuations of primary ionization is very high: for 5mm gas gap and Ar - based mixture we can expect to find primary ionization cluster with charge above 100 e^- for approximately 3% of tracks, while the most probable value is 1 e^- per cluster. It means, that periodical sparks is unavoidable. To fight negative influence of discharges on detector maximum flux capacity special double-layer structure of readout electrodes may be used, as it is shown on fig.1. The "top" or "high voltage" strips are made of material with high resistivity and serve to create high-tension electric field in amplification gap. The second layer, copper "pickup" strips collect signal initially induced on HV strip and transport it to amplifier. Due to high resistivity in case of spark only small part of HV strip (up to few mm) discharged, while almost full detector area remains active. This principle is planned to be used in SPD micromegas vertex detector.

Hit reconstruction and accuracy

Even perpendicular track usually result in signals induced on several neighbor strips, "signal cluster". For track angles, close to 90° standard "charge centroid" method works perfectly. In this method hit coordinate is calculated according next formula: $x = \frac{\sum A_i x_i}{\sum A_i}$, where A_i is signal amplitude, x_i is strip coordinate and summing is done over all strips in cluster. Compass experience [2] demonstrates that space resolution better then 100μ may be routinely achieved for perpendicular track. For inclined tracks charge centroid method is accuracy is much worse. In this case so-called "micro-TPC" algorithm is much more suitable. In this method drift time information for every strip signal is used to reconstruct distance from primary ionization cluster to mesh. Accuracy vs incoming track angle dependence for centroid and μ-TPC methods obtained at beamtest of ATLAS MM prototype is shown on fig.2. As it may

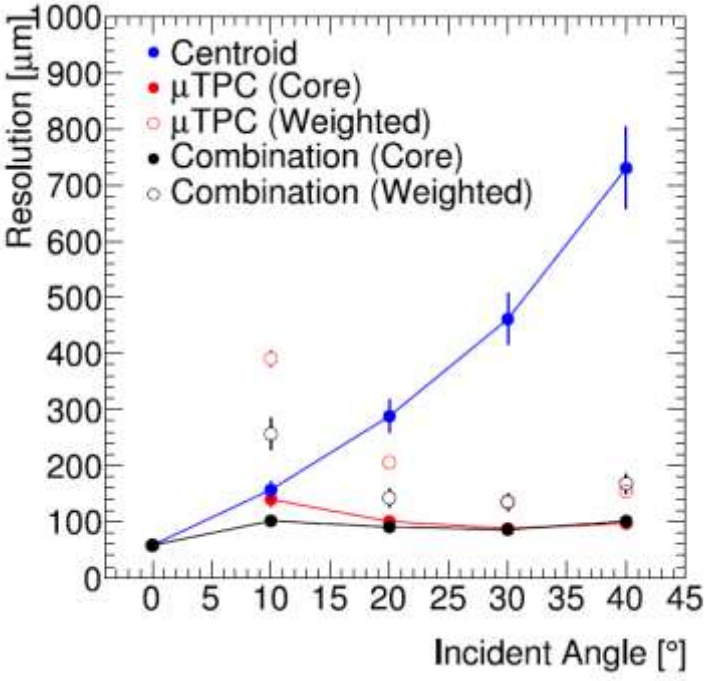

Figure 2. Dependence of space resolution on incoming track angle for charge centroid and μTPC hit reconstruction methods. Beamtest results of ATLAS micromegas prototype chambers. Plot is used with kindly permission of ATLAS muon group

be seen, combination of charge centroid and μ-TPC methods provide accuracy 100-150μ for incoming track angle from 0° to approximately 45°. Unfortunately, μ-TPC method normally require better signal to noise ratio and, hence, higher gas gain.

For SPD experiment all tracks are almost perpendicular to detector plane, but as MM operate in magnetic fields, non-zero Lorenz angle result in drift line inclined respect to electric field direction. For the hit reconstruction algorithms tracks looks like “effectively inclined” (fig.3). Lorentz angle for drift

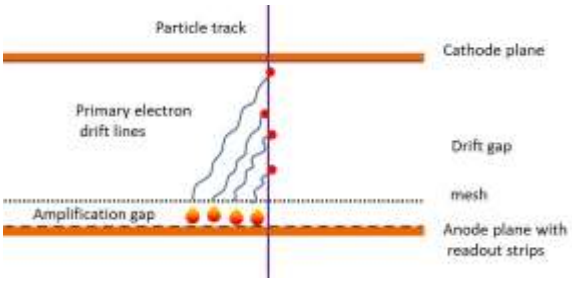

Figure 3. Drift lines of primary ionization electron for micromegas operation in magnetic field

field 600 V/cm and magnetic field of 1 Ts for several gas mixtures is given in table 1. There are several options to get good space resolution for MM operation in reasonable magnetic field:

1. Use micro-TPC algorithm for hit reconstruction. This option requires stable MM operation at relatively high gas gain $\boldsymbol{G \approx 10^4}$.
2. Operate MM with increased drift field to reduce Lorentz angle. Reliability of this approach was demonstrated by CLAS12 collaboration [Clas12], who get resolution about 150μ with MM tracker working in 5Ts magnetic field. The disadvantage of this solution is reduced effective mesh transparency and detector efficiency.
3. Choose gas mixture with very low Lorentz angle. Possible candidates are mixtures like CO_2-Ar-iC_4H_{10}(70-20-10) with expected Lorentz angle about 5^o-7^o. Unfortunately these mixtures are rather slow in weak fields and were never used for MM operation, so additional R&D is necessary.

This moment option 1 is a mainstream, but options 2 or 3, or some combination is not excluded too. Neither options need hardware modification; final decision may be done safely after additional tests.

Bulk micromegas technology

There are several methods to build micromegas detector. We propose to use bulk Micromegas technology [bulk] to build SPD vertex detector. In this method readout pcb, amplification gap and mesh produced as an entire module using photolithography. Production procedure include following steps:

1. Pcb with readout strips is laminated with photoresist material. The thickness of photoresist define amplification gap of micromegas detector.
2. Steel mesh pre-tensioned on temporary frame is applied over pcb and photoresist and fixed by additional photoresist layer
3. Photoresist is exposed by UV light through photo mask.
4. Unexposed photoresist are removed by chemical etching. Exposed photoresist form edge zone and pillars.

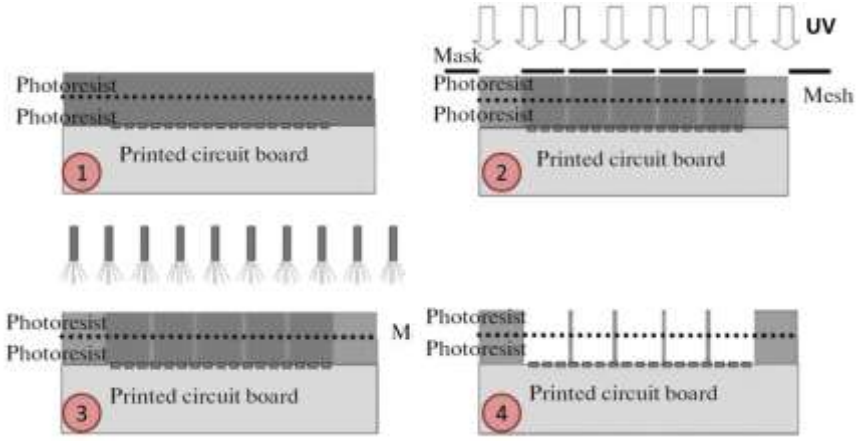

Figure 4. Main bulk micromegas production steps. 1- readout pcb lamination with photoresist and fixation of pre-tensioned mesh; 2-exposition of photoresist to UV light through mask corresponding to desired pillar pattern; 3-etching of unexposed photoresist; 4-finished bulk micromegas module (without anode plane)

Production procedure is illustrated on fig.4. As a final step cathode plane should be fixed at the distance of few mm from mesh, to form ionization gap. Bulk technology is simple, reliable and cheap, allow to use commercially-available materials and equipment and to build rather big detectors. PCB with mesh may be bent to build cylindrical detector, multiple fixation points prevent appearing of mesh waves or folds. The main disadvantage of method is the absence of possibility to disassemble pcb + mesh module to fix possible problem. So production is "single attempt" procedure.

Detector layer layout and production procedure

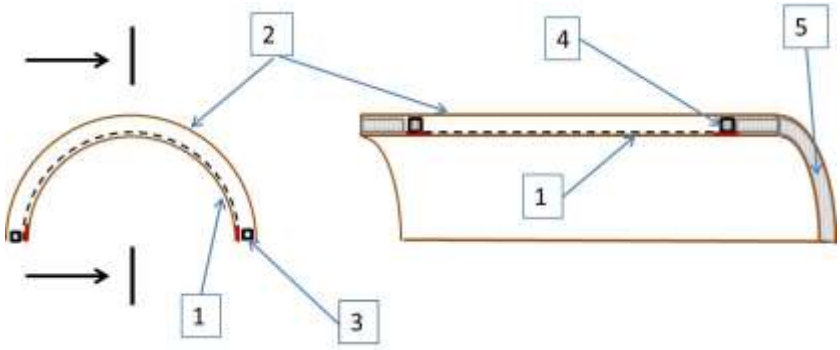

Figure 5. Simplified sketch of detector half-layer. Not in scale. Left: perpendicular cross-section. Right: longitudinal cross-section. 1 - readout board with mesh and amplification gap ; 2 -cathode board; 3 - carbon fiber longbeams; 4 - carbon fiber arcs; 5 – 3D printed plastic reinforcement. Passivated areas are shown by red color.

Every single MVD layer is independent 1- coordinate cylindrically-bended micromegas detector. As MVD inner diameter is smaller than vacuum tube flange diameter, it should be finally assembled around fixed beam pipe. Due to this reason every detector layer will consist of 2 independent half-cylindrical parts. Main steps of of half-cylindrical micromegas detector production are listed below:

1. Readout pcb + mesh module is produced using "bulk micromegas" technology.

2. “Bulk module” (readout pcb with fixed mesh) is bent on cylindrical template. Carbon composite longbeames is glued on long edge of pcb, and half-arcs are glued on end-face edge of active area.
3. Cathode pcb is glued on top of longbeams and arcs, forming drift gap and closing gas volume

While readout and cathode boards itself are very thing and flexible, after gluing detector layer is rigid enough be self-supporting due to its shape. Longbeams are empty inside and will be used as a gas distribution pipe. Total pcb length is approximately 50 mm bigger than active area. This extra space will be used to put signal and high voltage connector and for gas communication. To provide required durability of “commuinication” part of the layer it will be reinforced by 3-D printed plastic elements. Simplified sketch of layer layout is shown on fig. 5. Minimal layer radius is 50 mm; total material budget is about 0.4% of radiation length per layer. Micromegas design requires to have some dead area near detector edges for the mesh fixation. In our case this areas also used to place force elements (carbon fiber longbeams). We estimate minimal width of dead zone as 4-5 mm, what result in geometrical inefficiency about 6% for innermost detector level.

Front-End electronic

VMM-3 based Hybrid128 FE board developed by RD51 collaboration is planned to readout MVD. Boards are commercially available and have reasonable cost. Both signal amplitude and arriving time may be measured. Threshold, shaping time and gain are turntable and fit micromegas requirements well. “Neighbour logic” option allow to readout strip with no threshold, if neighboring strip have signal above nominal threshold. This option is rather useful for hit reconstruction with charge weighting. Board have 128 readout channels and compact physical dimension of 50x80 mm^2, which allows to place electronic within straw tracker at minimal distance from micromegas detector. Board is developed to work as a part of Scalable Readout System, what provide straightforward way to integrate readout to common SPD DAQ.

Limitation on MVD design

There are 2 main limitations on vertex detector design:

1. Maximum single detector active area is limited to $800 \times 600\ mm^2$ by available lithography equipment. Maximum PCB size is about$900 \times 600\ mm^2$. It apply requirement to split outer layers on 2 subdetectors along beam axis to get reasonable geometrical acceptance.
2. Existing front-end electronic based on VMM3 chip have some noise problem if readout electrode capacity substantially above 100 pF. As typical MM detector strip and flat cable capacity is about 100 pF/m, it very desirable to keep total length of readout strips and cables within 1m.

Vertex detector layout

General detector layout is shown on fig.6. Seven detector layers organized as 3 superlayers. Each superlayer consist of 3 or 2 layers with different strip orientation, rigidly connected together. Outer superlayer is divided on 2 parts along Z axis due to limit on maximum detector size. Dead area between two parts is 10mm. Layer summary is given in table 1. Front-end board placed in 4 disks about 10 cm from both end-face of detector. Detector signal connectors and FE board are connected by thing flat cable (not shown on the sketch).

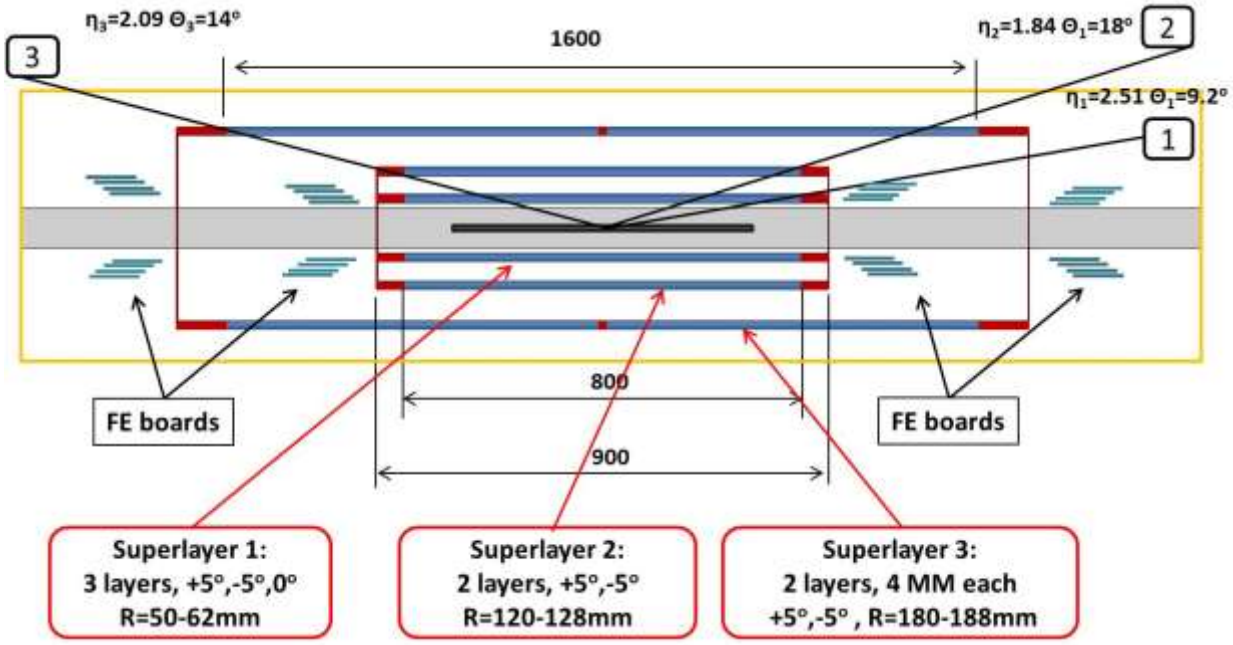

Figure 6. layout of micromegas vertex detector. Blue colors mark active area of superlayers. Dead areas are marked by red color. Inner border of straw tracker is shown by yellow line. Beam pipe is shaded by gray color, black area in the middle of beam pipe – beam crossing area

Table 1. Summary of vertex detector layers

Layer	Super-layer	Radius, mm	Strip length, mm	Strip angle	Pitch, mm	N chan	N boards	Geom. acceptance
1	1	50-54	800	$+0^{o}$	0.4	736	6	9^{o}-171^{o}
2		54-58	800	$+5^{o}$	0.4	794	8	
3	1	58-62	800	-5^{o}	0.4	1037	9	9^{o}-171^{o}
4	2	120-124	800	$+5^{o}$	0.55	1463	12	18^{o}-162^{o}
5		124-128	800	-5^{o}	0.55	1509	12	
6	3	180-184	2x800	$+5^{o}$	0.55	2x2150	36	13.3^{o}-166.7^{o}
7		184-188	2x800	-5^{o}	0.55	2x2195	36	

1. Giomataris, I., et al. (1996) Micromegas: a high-granularity, position-sensitive gaseous detector for high particle flux environments. Nucl. Instr. and Meth. A376, 29(1996)
2. Compass paper
3. [CLAS12] NIM A957(2020),12
4. [bulk] I. Giomataris, R. De Oliveira, S. Andriamonje, S. Aune, G. Charpak, P. Colas, G. Fanourakis, E. Ferrer, A. Giganon, Ph. Rebourgeard, and P. Salin, “Micromegas in a bulk,” Nucl. Instr. and Meth. A **560**, 405 (2006).

Chapter 12

Radiation environment

1 Radiation background in the detector

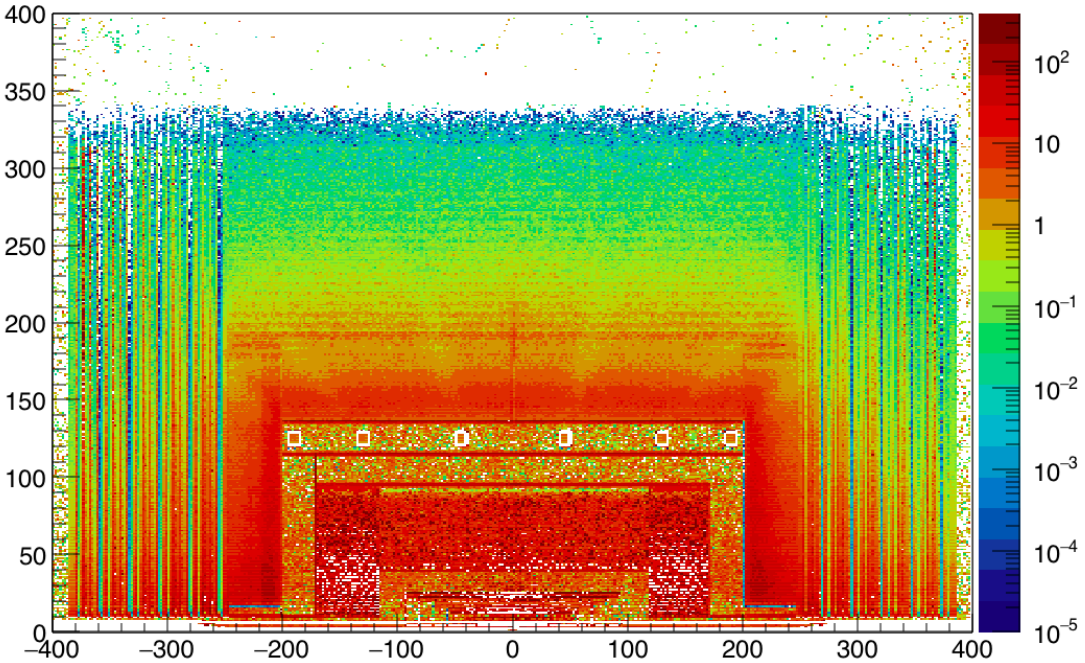

Figure 12.1: Dose, Gy/year

2 Radiation background in the experimental hall

Chapter 6

Detector control system

The SPD detector control system (DCS) is designed to control the basic operating modes of the detector parts and the detector as a whole, and to continuously monitor slowly changing parameters of the detector, engineering means which provide the detector operation, and the environment. The DCS is synchronized with the basic operating modes of the NICA accelerator complex by means of a synchronization subsystem shared between the DCS and the SPD DAQ. The DCS provides parameterization of the managed object (i.e. the SPD detector), implements algorithms for normalization, parameters measurement and control based on these parameters, and generates the necessary sets of abstractions and options for presenting these abstractions to the operator in an intuitive manner. Critical values of the parameters going beyond the predefined limits in predetermined situations cause emergency events and initiate procedures for handling such events, including the procedure for an automatical detector shutdown in order to prevent its damage. Parameter values are archived in a database for long-term monitoring of the detector operation and identify possible failures in the operation of the equipment and emergency situations. The configurations of the detector parameters saved in the database make it possible to start the detector promptly and use it with various preset parameters and in various operating modes in accordance with the requirements of a particular physics experiment. The DCS allows autonomous operation of each detector subsystem at the stage of the initial start-up as well as its periodic maintenance, calibration sessions, and planned upgrades. The number of parameters in the system is expected to be significant, therefore, it is assumed that the system should be extendable and flexibly configurable. Architectural and software solutions based on the event-driven model [**?**] and client-server and producer-consumer [**?**] interaction models should be preferred for communication, when building the general DCS and the control systems of each part of the detector. Centralized systems operating in the master-slave polling mode should be avoided.

1 DCS concept

Most of high-energy physics detectors include parts consisting of similar systems built from devices, sensors, and actuators with similar or identical functionality. This determines parameterization of the entire detector as a managed object. Such systems include:

1. high voltage (HV) power supply system for powering gas detectors and light (photon) sensors (PMT and SiPM);
2. low voltage (LV) power supplies for powering magnets, digital and analog electronics;
3. cryogenic systems;

4. gas supply and mixing systems;
5. vacuum systems;
6. front-end electronic LV powering control and temperature monitoring;
7. different cooling and temperature control systems;
8. DAQ system;
9. accelerator interface and synchronization;
10. general external electricity and water cooling stations, etc.

The SPD detector is no exception and includes almost all of these systems spread among different parts of the detector, as shown in the layout diagram, Fig. 6.1. Each part of the detector refers to one or more subsystems. The composition of the systems will be refined, as the individual parts of the detector are developed.

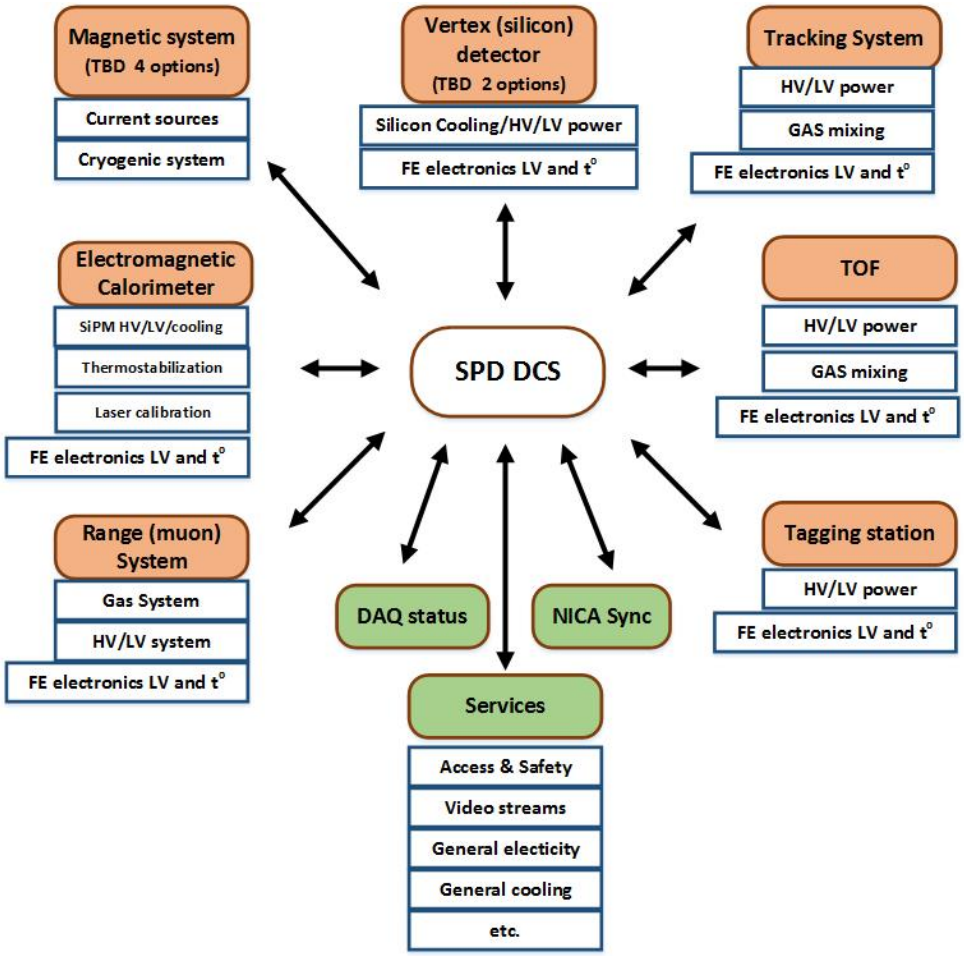

Figure 6.1: SPD detector control system layout.

All the systems can be similarly parameterized and shown to the operator in an intuitive presentation in order to simplify the operator's decision-making algorithm. However, the physical implementation at the hardware level of these elements may vary significantly in different parts of the SPD, because:

– the parts inherit the experience of their developers gained in previous experiments;

– hardware and software components are selected based on their cost and availability;

– parts of the detector are manufactured at different times.

Nevertheless, in order to optimize financial and human resources costs for the creation of the entire detector and the DCS, in particular, it is necessary to recommend the developers of the detector parts to strive for standardization of the used hardware and embedded software. This will significantly reduce the efforts put into developing, deploying, and operating the detector and will result in significant cost savings. To achieve these goals, at the stage of prototyping the detector systems it is advisable to work out not only the detector itself, the front-end electronics and the DAQ, but also the slow control systems. This work can be carried out in the beam test zone (BTZ), for which the BTZ slow control system must be made as similar to the final DCS version as possible.

2 DCS architecture

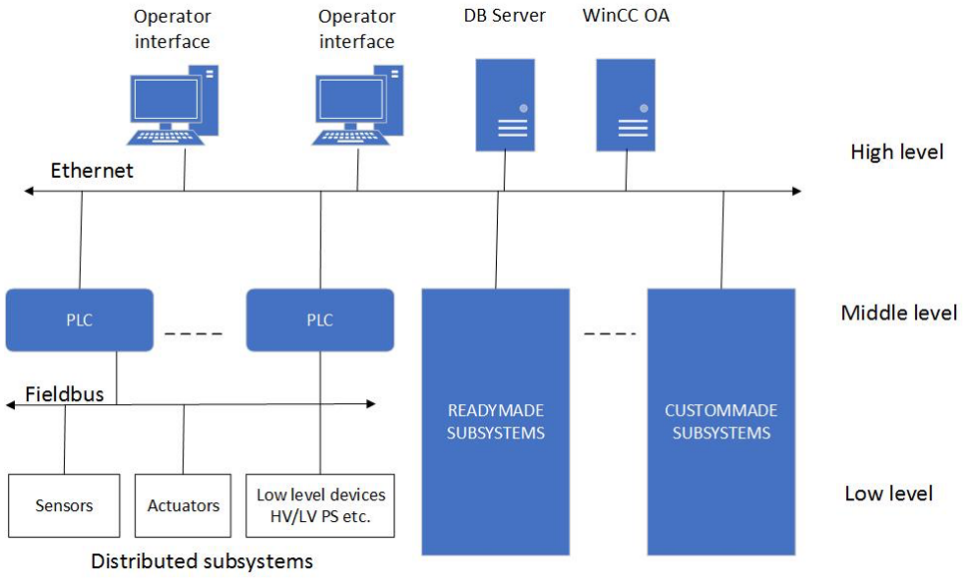

Figure 6.2: SPD detector control system architecture.

The detector control system is divided into three logical levels (Fig. 6.2). The lower level includes measurement channels built into the Front End Electronics (FEE) and Data Acquisition (DAQ) of the detector parts, various stand-alone sensors, I/O devices, and low and high voltage power supplies. The middle level is represented by programmable logic controllers and integrated ready-made and custom-made subsystems (vacuum posts, gas consoles, multichannel ready-made power subsystems, etc.). The interfaces to the FEE and DAQ that provide data for the detector control system are also on this level. The upper level is designed to provide a human-machine interface for operators, implement a database of detector parameters and configurations, communicate with the external world (accelerator, engineering support systems, access system, etc.), and implement macro-control algorithms common for the entire detector. All these levels are connected in a hierarchical network using fieldbuses between the first and the second level, for example, a CAN-bus with a CANopen protocol. An Ethernet LAN is used between the middle and the upper levels. At the top level, special software, such as SCADA (Supervisory Control And Data Acquisition), is used, which provides control, collection and storage of data in real time. It is

proposed to use the WinCC OA system common at CERN, as a SCADA system. We understand that for smooth and reliable communication with the control system of the Nuclotron, a gateway to the Tango Controls [**? ?**] system should be developed and deployed.

3 SCADA for the DCS

WinCC OA (ex PVSS-II) [**? ?**] is a commercial SCADA system. It is a software component constructor that allows one to use both preinstalled prototypes and templates, and software modules and system components developed in C. This system is actively used in many experiments at CERN and has support and safety certificates in the Russian Federation. The following properties make WinCC OA an attractive solution to be used in the DCS SPD:

- object-oriented approach built into the system ensures an efficient development process and the ability to flexibly expand the system;
- capability to create distributed systems - up to 2048 WinCC OA servers;
- scalability from a simple single-user system to a distributed redundant network system with $>$ 10 million tags (physical and synthetic parameters);
- platform independent system is available for Windows and Linux;
- event-driven system;
- hot standby and 2x2 redundancy (DRSystem), the required level of availability and reliability;
- wide range of drivers and options for communication OPC, OPC UA, S7, Modbus, IEC 60870-5-101/104,DNP3, XML, JSON, SOAP, ...;
- support by major manufacturers of electronic devices for building automation systems in high energy physics.

Each functional unit of the system that is software implemented as a separate process is called manager. A set of managers forms a system. Data exchange and communications between managers are done via TCP. The data is exchanged by means of passing events. The system allows parallelizing processes (managers) by running them on different computers with different OS. The system is scalable and balances the load on the control computers. The required managers start only if necessary and multiple instances may run simultaneously. Managers can be distributed across multiple computers/servers. The WinCC OA block diagram is shown in Figure 6.3. The main process is the Event Manager, it contains and manages the process image (current values of all process variables), receives and qualifies data (central message manager), distributes data across other managers, acts as a data server for others, manages users authorization, manages the generation and status of alarm messages. The Database Manager receives data from the Event Manager and handles it according to its own algorithm. The historical database can use either a proprietary database (HDB) or an Oracle DBMS (the Oracle Real Application Clusters configuration is also supported). Parallel archiving in Oracle and HDB databases is possible. It is also possible to record user-defined data and log system events and messages in an external relational database (MS SQL, MySQL, Oracle, etc).

The WinCC OA Report Manager supports different ways of generating reports:

- in Microsoft Excel format;

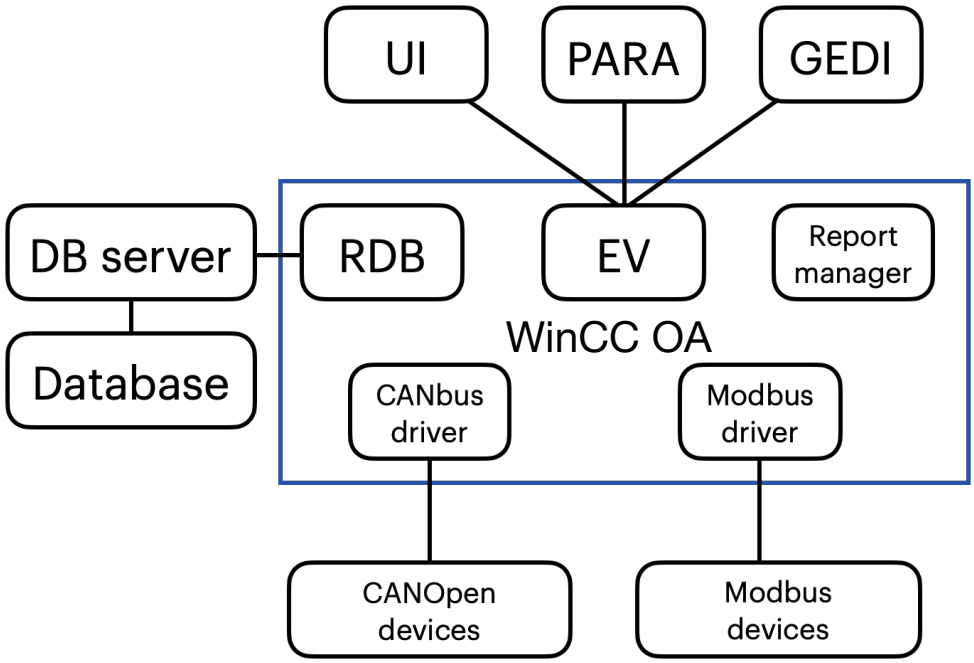

Figure 6.3: SCADA structural scheme of the WinCC OA software.

– in the *xml* format with the ability to display in any external tool for working with reports (Eclipse BIRT, Crystal Reports, SYMATIC Information Server etc.), SOAP (Simple Object Access Protocol) protocol is also supported.

Project development for the WinCC OA system is based on an object-oriented approach. In the WinCC OA data model, objects are represented as data points that characterize the image of a specific physical device or process. For each data point (called tag) element, properties and actions, such as signal processing (smoothing, setting limits, etc.), communication with external systems, archiving, generation of alarm messages (alarms), etc. can be defined in accordance to it. Typing and inheritance are supported, therefore arbitrary hierarchical data structures can be created. Similarly, the principles of inheritance and reusability are implemented for graphical objects. The WinCC OA IDE includes the PARA configuration editor and the GEDI graphical editor of the User Interface Manager (UI) (includes a data model editor, mass configuration tools, administration tools, an interface to version control systems, a debugger, etc.). Changes to data structures and graphics are applied without restarting the project. Writing custom scripts can be done using CONTROL++ (a programming language, the syntax of which is similar to C/C++). Such scripts can be both event handlers associated with the elements of the graphical interface, and data processing procedures. The system includes a standard graphical objects library; it can be extended by developing user objects or using the Qt Toolkit widgets. It is also possible to use the JavaScript libraries available on the market or included JavaScript scripts. Thanks to the open API (C++ / C# API), it is possible to create managers, drivers, widgets, and CONTROL++ extensions. A new set of tools is available for the concept of High Speed Programming implementation, which supports documentation build-up from the source code, unit testing and autocompletion of program structures.

It is also planned to provide data exchange between the WinCC OA and Tango Controls, which is used as the upper level of the Nuclotron control system. This can be implemented using standard OPC technologies with a client-server architecture, or it can be implemented using SQL tools as a common database for both SCADA systems used for the accelerator and the detector. The final choice of a suitable solution will be made at the stage of system implementation.

Chapter 1

Computing and Offline Software

1.1 Introduction

Expected event rate of the SPD experiment is about 3 MHz (pp collisions at $\sqrt{s} = 27$ GeV and 10^{32} cm^{-2}s^{-1} design luminosity). This is equivalent to the raw data rate of 20 GB/s or 200 PB/year, assuming the detector duty cycle is 0.3, while the signal-to-background ratio is expected to be in order of 10^{-5}. Taking into account the bunch crossing rate of 12.5 MHz, one may conclude that pile-up probability cannot be neglected.

The key challenge of the SPD computing is the fact, that no simple selection of physics events is possible at the hardware level, because the trigger decision would depend on measurement of momentum and vertex position, which requires tracking. Moreover, the free-running DAQ provides a continuous data stream, which requires a sophisticated unscrambling prior building individual events. That is the reason why any reliable hardware-based trigger system turns out to be over-complicated and the computing system will have to cope with the full amount of data supplied by the DAQ system. This makes a medium-scale setup of SPD a large-scale data factory (Fig. 1.1).

The continuous data reduction is a key point in the SPD computing. While simple operations like noise removal can be done yet by DAQ, it is an online filter that is aimed at fast partial reconstruction of events and data selection, thus being a kind of a software trigger. The goal of the online filter is to decrease the data rate at least by a factor of 20 so that the annual upgrowth of data including the simulated samples stays within 10 PB. Then, data are transferred to the Tier-1 facility, where full reconstruction takes place and the data is stored permanently. The data analysis and Monte-Carlo simulation will likely run at the remote computing centers (Tier-2s). Given the large data volume, a thorough optimization of the event model and performance of reconstruction and simulation algorithms are necessary.

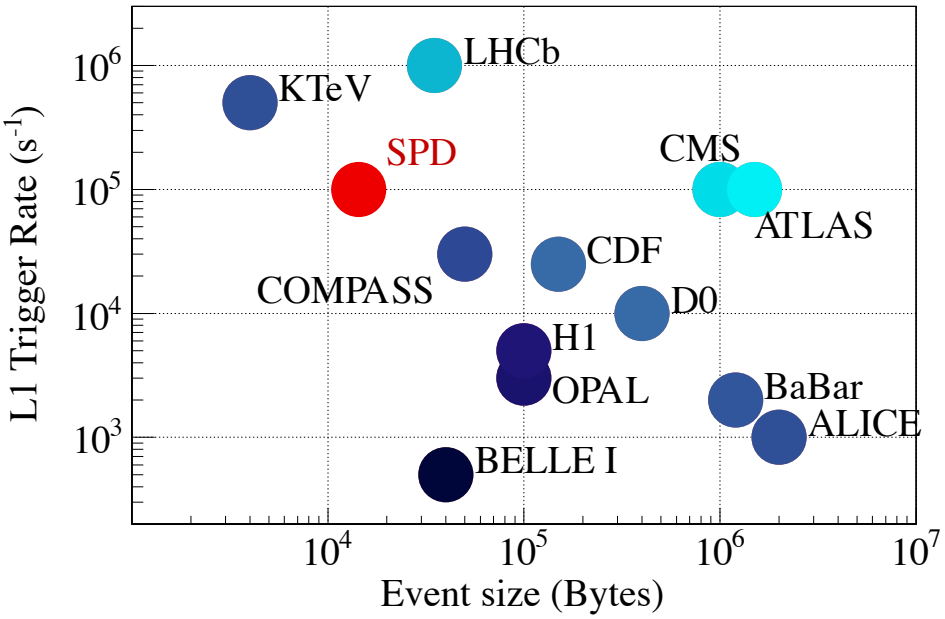

Figure 1.1: Expected event size and event rate of the SPD setup after the online filter compared with other experiments [1].

Table 1.1: The assumed event data sizes for various formats, the corresponding processing times and related operational parameters.

Item	Unit	Value
RAW event	kB	7
RECO event	kB	15
Time for Reconstruction (1 ev)	HepSPEC	100
Time for Simulation (1 ev)	HepSPEC	500
Event rate at maximum luminosity	Hz	3000
Event rate after online data filter	Hz	150
Operation time	seconds/day	50000
Operation time	days/year	200

1.2 SPD computing model

1.2.1 Input parameters

The assumptions of Table 1.1 are used to calculate the storage and computing resources. At present, all processing-time numbers are higher than assumed here.

1.2.2 Data flow and event data model

Data processing is supposed to be done in several stages. At the first stage, the data is fast reconstructed and events are built from continuous byte stream. This task will be performed online using a dedicated high-performance computing cluster (online data filter). After fast reconstruction, the events are selected according to a set of physical criteria to suppress the contribution from background processes. Then, the selected data are saved for long-term storage and subsequent full reconstruction. Full reconstruction differs from fast reconstruction by more accurate and complex algorithms that use information about the slow control system, calibration constants, and combined analysis of information from various subsystems, in particular, to identify particle types.

Two reconstruction cycles are foreseen. The first cycle includes reconstruction of some fraction of each run necessary to study the detector performance and derive calibration constants, followed by the second cycle of reconstruction of full data sample for physics analysis. Detector simulation will run in parallel. The amount of simulated data are expected to be comparable to the amount of selected experimental data. A large amount of data, the computing resources required for their processing and analysis within the framework of an international collaboration naturally require the construction and use of a distributed data storage and processing system.

1.2.3 Event building and filtering

The main goal of the SPD online filter is to reconstruct events from the continuous byte stream and to suppress the background by a factor of 20 or so. The input for the online filter are the raw data files. The format of these files are determined by the frontend electronics and the DAQ system. The result of the data processing at the online filter are a set of reconstructed events, containing also raw information for the more detailed offline reconstruction. HDF5 will be used as the output format for the online filter, to simplify data treatment by the offline computing system. Because of data reduction, it is likely that merging of several small output files to a bigger one will be necessary.

1.2.4 Offline data processing

Offline data processing includes offline reconstruction and MC simulation. Offline reconstruction starts with the output of the online filter. Detailed calibration and more precise algorithms will be used to refine the data sample and to improve the efficiency and precision of reconstruction of physics objects. Particle identification will be made at this stage as well. The output of the offline reconstruction will be stored in ROOT trees in RECO format, to allow direct use in a further physics analysis.

Simulation is necessary both for the data analysis and for the training of neural networks at the online filter. Tha latter should reproduce not only the event topology and kinematics, but also a time structure similar to the one in real data. The output of the simulation will be stored in the same format as for the reconstruction of the real data, except adding MC truth information.

1.2.5 User analysis

User analysis will be done using pre-selected RECO data or derived ROOT trees.

1.3 Online data filter

1.3.1 Introduction and requirements

The SPD online filter facility will be a high-throughput system which will include heterogeneous computing platforms similar to many high performance computing clusters. The computing nodes will be equipped with hardware acceleration. The software framework will provide the necessary abstraction so that common code can deliver the selected functionality on different platforms.

The main goal of the online filter is a fast reconstruction of the SPD events and suppression of the background ones at least by a factor of 50. This requires fast tracking and fast clustering in the electromagnetic calorimeter, followed by reconstruction of event

from a sequence of time slices and an event selection (software trigger). Several consecutive time slices shall be considered, tracker data unpacked and given for a fast tracking. The result of the fast track reconstruction is the number of tracks, an estimate of their momentum and an estimate of primary vertex (to distinguish between tracks belonging to different collisions). Using this outcome, the online filter should combine information from the time slices into events and add a trigger mark. The events shall be separated in several data streams using the trigger mark and an individual prescale factor for each stream is applied.

Besides the high-level event filtering and corresponding data reduction, the online filter will provide input for the run monitoring by the shift team and the data quality assessment, as well as local polarimetry.

1.3.2 Computing system

Fast reconstruction and filtering of data from an SPD detector cannot be performed on a single node. A specialized high-performance cluster is neccesary, which includes several data storage systems (for receiving detector data, for temporarily storing filtered data before transferring it to long-term storage, and for storing software and auxiliary data), a large number of identical working nodes for data processing and few servers performing management of this system and the movement of data in it (Fig. 1.2). To control the operation of the system, it is proposed to use auxiliary programs (pilots) that are constantly executed at each working node and exchange messages with the dispatcher server. Fast messaging system ZeroMQ or nanomsg will be used for communication. Depending on received messages, the pilot programs will initiate copying of new data from the storage system to the working node, call the program for fast reconstruction and filtering of data, and copy the processing result to the output buffer. In addition, pilots will be able to perform other, auxiliary operations, such as data merging, monitoring, etc. The data flow from the detector, which will reach values of the order of 20 GB / s, determines high requirements for the performance of data storage systems and for the speed of data processing algorithms.

1.3.3 Fast event reconstruction

Fast tracking and vertex reconstruction

The most important and complicated task in the data reconstruction chain is tracking. Traditional tracking algorithms, such as the combinatorial Kalman filter, are inherently sequential, which makes them rather slow and hard to parallelized on modern high-performance architectures (graphics processors). As a result, they do not scale well with the expected increase in the detector occupancy during the SPD data taking. This is especially important for the online event filter, which should be able to cope with the extremely high data rates and to fulfill the significant data reduction based on partial

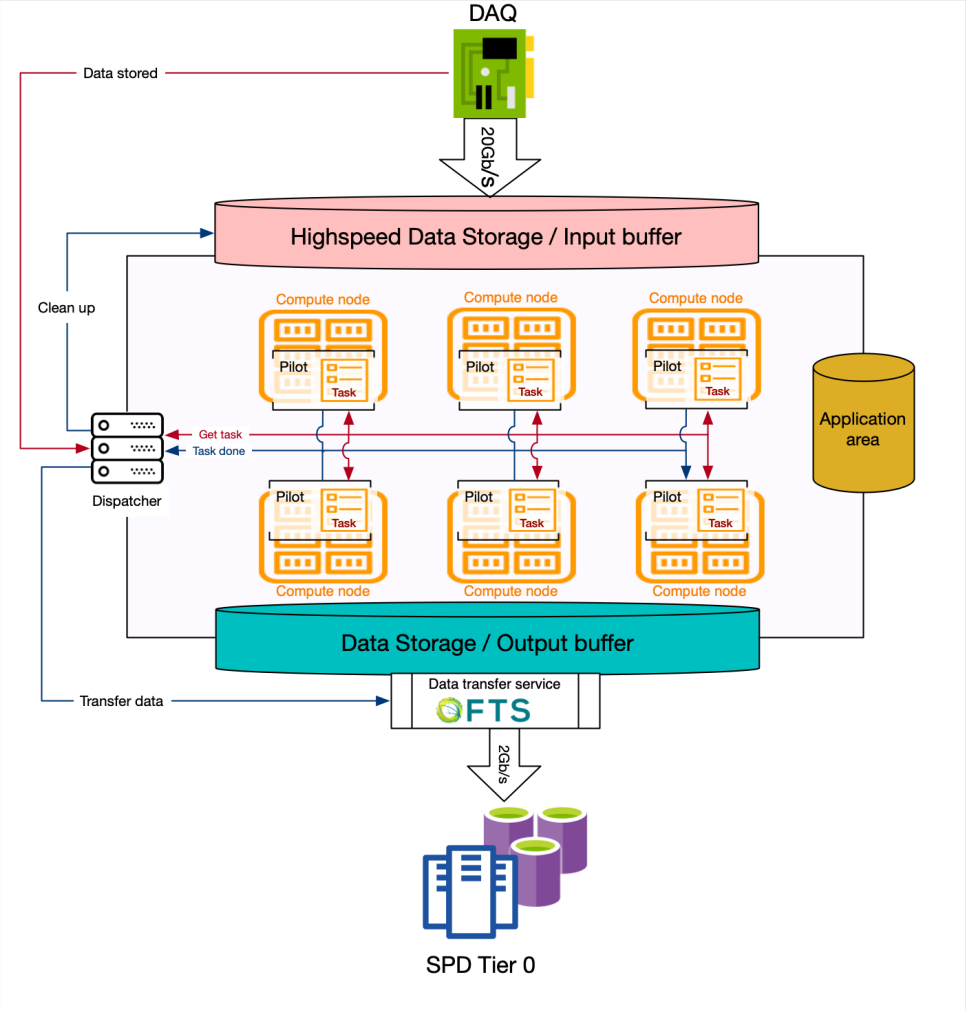

Figure 1.2: Design of the online data filtering system.

event reconstruction 'on the fly'. The parallel resources like multicore CPU and GPU farms will likely be used as a computing platform, which requires the algorithms, capable of the effective parallelization, to be developed, as well as the overall cluster simulation and optimization.

Machine learning algorithms are well suited for multi-track recognition problems because of their ability to reveal effective representations of multidimensional data through learning and to model complex dynamics through computationally regular transformations, that scale linearly with the size of input data and are easily distributed across CPU or GPU cores. Moreover, these algorithms are based on the linear algebra operations and can be parallelized well using standard ML packages. Two algorithms of track recognition in strip and pixel detectors are considered. The first algorithm, TrackNetv3, relies on the use of a recurrent neural network (RNN), which allows to combine track extrapolation with testing the hypothesis that a set of points belongs to a true track and is compatible with a smooth curve. That is, essentially reproduces the idea of a Kalman filter with the difference that the physical parameters describing the track are approximated by a neural network using synaptic weights determined during its training. The second approach, RDGraphNet, uses a graph network and allows to implement of a global search for tracks in an event, which is especially attractive when analyzing events with a large multiplicity. These approaches have already been successfully used for track recognition in the BM@N experiment at JINR and in the BESIII experiment at IHEP CAS in China [2, 3, 4, 5, 6]. These algorithms will be adapted to find and reconstruct particle tracks in SPD data from the vertex detector and the main straw tracker. The main difficulty is the adaptation of neural networks to recover tracks in drift detectors, which requires solving the "left-right" ambiguity. To prototype neural networks and study the quality of their work, the Ariadne software package [7] will be used.

ECAL clustering

Algorithms based on convolutional networks will be developed to search for clusters in the SPD electromagnetic calorimeter and to reconstruct π^0s.

RS clustering

To identify muons in a muon system, the convolutional neural network will be used. Another option is to apply a simpler gradient boosting algorithm on trees.

Event unscrambling

Data stream from the DAQ will be stored in files of about 4 GB. Each file will be processed independently from other ones. Data blocks corresponding to a certian duration of data taking (from 5 to 15 μs) will be used a reconstruction unit. Data from different subdetectors in each data block will be fed to a series of consecutive neural networks.

First, vertices and track seeds will be determined using vertex detector data. Tracks will be associated with vertices and bunch crossing time will be determined for each vertex. Then, tracks will be reconstructed using track seeds from the vertex detector. Hits in the straw tracker, which are not associated with any track, will be collected in a selected time window according to the bunch crossing time and attached to the events for possible use in the offline reconstruction. ECAL and RS hits will be reconstructed by other neural networks and associated with vertices according to the bunch crossing time. Raw data from other subdetectors will be attached to the events according to bunch crossing time. The block of information, associated with each vertex following the procedure described above will be called an event.

Online polarimetry

TBD

1.3.4 Implementation of machine learning algorithms

Training and validation

Training of neural networks will be based on a dedicated large sample of simulated data.

The caution is necessary, though, to avoid possible bias due to an inadequacy of the training data to the real ones, including possible machine background and the detector noise. A dedicated workflow that includes continuous learning and re-learning of neuron network, deployment of new versions of network and the continuous monitoring of the performance of the neural networks used in the online filter will be applied.

Integration to the online data filter

For the effective use of deep learning algorithms, besides the design of the neural networks and their training, it is necessary to solve a number of technical problems. First, open-source machine learning tools (TensorFlow, sklearn, PyTorch, etc.) tend to have python interfaces, making them difficult to use in real-time systems. To solve this problem, it is planned to choose a package that has an advanced C++ API, and also to separate the of network training (which can be implemented in any way) and its application. Secondly, there is a risk that the neural network will malfunction if the initial data is very different from the data that was used for training. In a physical experiment, these differences can be caused, for example,the background from the accelerator or by a change in the detector performance or noise. Therefore, it is required to foresee a procedure for monitoring the correct operation of neural networks. For this, it is proposed to process a certain fraction of data independently using classic algorithms and compare the result of their work with the result of the work of deep learning algorithms. In case of large differences, one should either mark the data as questionable or retrain the neural network to work in

new conditions. Third, the application itself for fast reconstruction and filtering of data is proposed to be implementedthe form of a framework in order to be able to flexibly customize the sequence and content of the data processing procedure.

1.3.5 Online data processing framework

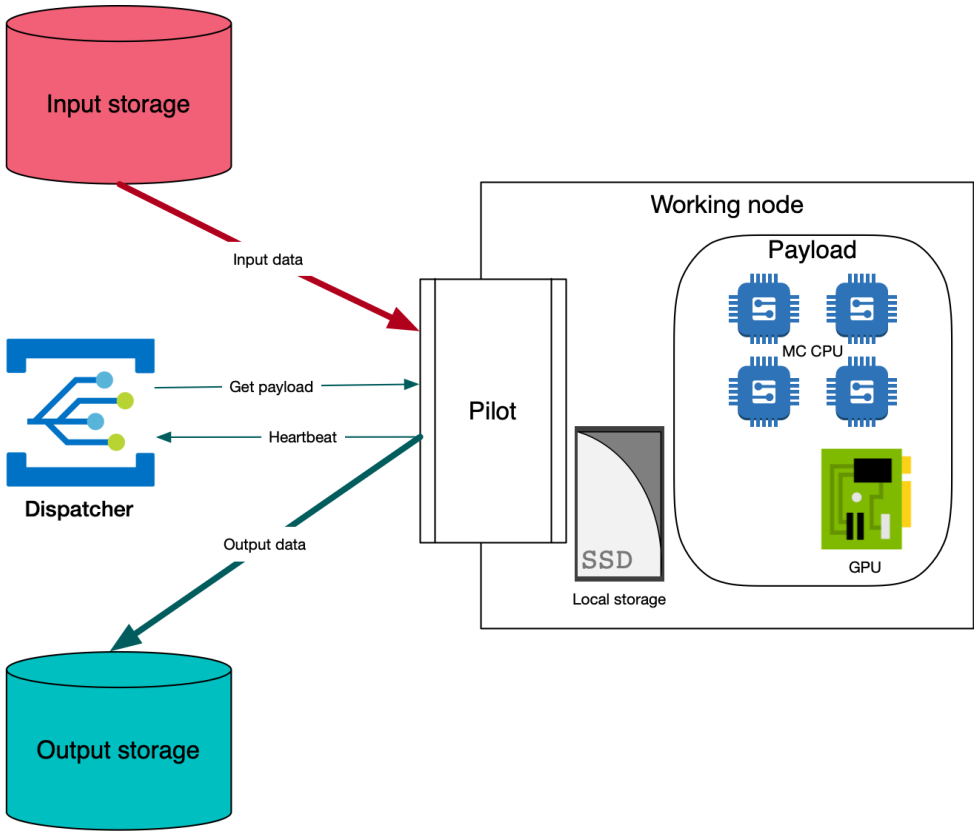

Figure 1.3: Operation of the online data processing framework at a selected working node.

1.3.6 Online monitoring and data quality assurance

1.4 Offline software

1.4.1 Introduction and requirements

Offline software is a toolkit for event reconstruction, Monte-Carlo simulation and data analysis. Linux is chosen as a base operating system.

Recent developments in computing hardware resulted in the rapid increase of potential processing capacity from increases in the core count of CPUs and wide CPU registers. Alternative processing architectures have become more commonplace. These range from the many-core architecture based on x86_64 compatible cores to numerous alternatives such as other CPU architectures (ARM, PowerPC) and special co-processors/accelerators: (GPUs, FPGA, etc). For GPUs, for instance, the processing model is very different, allowing a much greater fraction of the die to be dedicated to arithmetic calculations, but at a price in programming difficulty and memory handling for the developer that tends to be specific to each processor generation. Further developments may even see the use of FPGAs for more general-purpose tasks.

The effective use of these computing resources may provide a significant improvement in offline data processing. The development of the concurrent-capable software framework is needed to provide the offline software for Day-1 of the SPD detector operation, as well as a dedicated R&D effort to find proper solutions for the development of efficient cross-platform code.

1.4.2 Choice of the framework

SpdRoot

Currently, the offline software of the SPD experiment – SpdRoot – is derived from the FairRoot software [8] and it is capable of Monte Carlo simulation, event reconstruction, and data analysis and visualization. The SPD detector description is flexible and based on the ROOT geometry package.

A Gaudi-based framework

To take an advantage of modern computing hardware, the offline software should be capable to do it by taking advantage of concurrent programming techniques, such as vectorization and thread-based programming. This is the reason why another framework based on Key4Hep [9] is developed.

1.4.3 Detector description

TBD

1.4.4 Calibration and Alignment, Conditions

TBD

1.4.5 Simulation

Proton-proton collisions are simulated using a multipurpose generator Pythia8 [10]. Deuteron-deuteron collisions are simulated using a modern implementation of the FRITIOF model [11, 12], while UrQMD [13, 14] generator is used to simulate nucleus-nucleus interactions. Transportation of secondary particles through the material and magnetic field of the SPD setup and the simulation of detector response is provided by Geant4 toolkit [15, 16, 17].

1.4.6 Reconstruction

Track reconstruction uses GenFit toolkit [18] and KFparticle package [19] is used to reconstruct primary and secondary vertices.

1.4.7 Physics analysis tools

ROOT and Python-based tools (NumPy, SciPy, Pandas) are expected to be widely used.

A DIRAC [20] framework will be used to run user simulation at distributed computing resources.

1.4.8 Software infrastructure

A git-based infrastructure for the SPD software development already established at JINR [].

1.5 Computing system

The projected rate and amount of data produced by SPD prescribe to use high throughput computing solutions for the processing of collected data. It is the experience of a decade of the LHC computing that already developed a set of technologies mature enough for the building of distributed high-throughput computing systems for HEP.

1.5.1 Computing model

The 'online' part of computing systems for the SPD experiment, namely the online filter described above, is an integral part of experimental facilities, connected with the 'offline' part using a high throughput backbone network. The entry point to 'offline' facilities is a high capacity storage system, connected with 'online facility' through a multilink high-speed network. Data from high capacity storage at the Laboratory of Information Technologies will be copied to the tape-based mass storage system for long term storage.

At the same time, data from high capacity storage will be processed on different computing facilities as in JINR as in other collaborative institutions.

The hierarchy of offline processing facilities can be introduced:

- Tier 1 level facilities should provide high capacity long term storage which will have enough capacity to store a full copy of primary data and a significant amount of important derived data;
- Tier 2 level facility should provide (transient) storage with capacity that will be enough for storing of data associated with a period of data taking;
- optional Tier 3 level are opportunistic resources, that can be used to cope with a pile-up of processing during some period of time or for special analysis.

Offline data processing resources are heterogeneous as on hardware architecture level so by technologies and at JINR site it includes batch processing computing farms, high performance (supercomputer) facilities, and cloud resources. A set of middleware services will be required to have unified access to different resources.

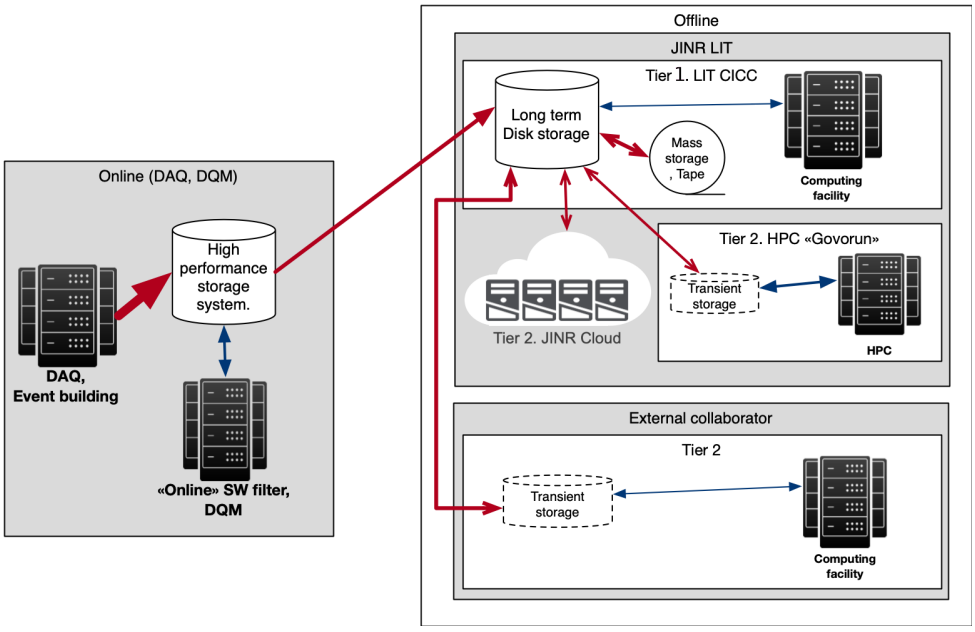

Figure 1.4: Scheme of the SPD computing system

1.5.2 Distributed computing

Computing systems for NICA at JINR are naturally distributed. Experimental facilities and main data processing facilities placed across two JINR sites and, inter alia, managed by different teams. That causes some heterogeneity not only on hardware systems but also on the level of basic software: different OSs, different batch systems etc.

Taking into account the distributed nature and heterogeneity of the existing infrastructure, and expected data volumes, the experimental data processing system must be based on a set of low-level services that have proven their reliability and performance.

It is necessary to develop a high-level orchestrating system that will manage the low-level services. The main task of that system will be to provide efficient, highly automated multi-step data processing following the experimental data processing chain.

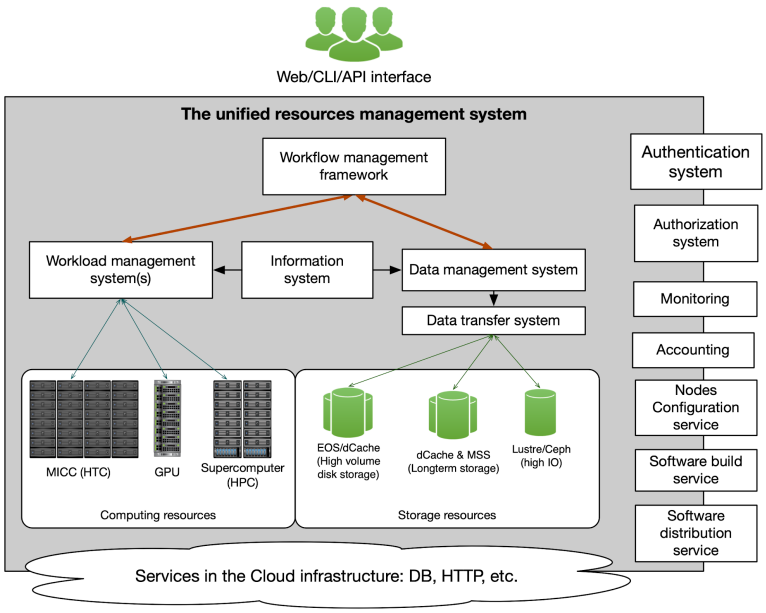

Figure 1.5: Distributed SPD computing services

The Unified Resource Management System is a IT ecosystem composed from the set of subsystem and services which should:

- unify of access to the data and compute resources in a heterogeneous distributed environment;
- automate most of the operations related to massive data processing;
- avoid duplication of basic functionality, through sharing of systems across different users (if it possible);

- as a result - reduce operational cost, increase the efficiency of usage of resources;
- transparent accounting of usage of resources.

Many distributed computing tools have already been developed for the LHC experiments and will be re-used in SPD.

1.5.3 Data management

For the distributed data management RUCIO [21] package will be deployed. For the massive data transfer FTS [22] will be used.

1.5.4 Task management

For the production management PanDA [23] software will be used.

1.5.5 Software distribution and deployment

CVMFS and docker-based containers will be used for the software distribution.

1.5.6 Databases

The central database is going to be established to keep and distribute run information, slow control data and calibration constants.

1.6 Project management and resources

1.6.1 Stages

Low luminosity configuration
    High luminosity configuration

1.6.2 Work packages and responsibilities

Online filter
    Offline software
    Computing system
    Deployment and Operation

Table 1.2: Required SPD computing resources

	CPU [cores]	Disk [PB]	Tape [PB]
Online filter	6000	2	none
Offline computing	30000	5	9 per year
Cost estimate [kUSD]	4000	8000	4500 per year

1.6.3 Resource requirements

For the online filter we assume the CPU consumption of 1000 SPD events/core/second. This requires 3000 cores simultaneously for the fast tracking. Taking into account additional expenditures to the event unscrambling and data packing and including a real efficiency of CPU which will be lower than 100%, one derives the CPU resources for the online filter as 6000 CPU cores. This number sets the upper limit and the required computing power may decrease substantially if an efficient way to use GPU cores is implemented for the event filtration. As for the data storage, a high performance disk buffer of 2 PB capable to keep data of about one day of data taking is needed.

For the offline computing, the data storage is determined by the data rate after the online filter, or 4 PB/year of raw data. Besides that, we may expect the comparable amount of simulated data and estimate the long term storage as 10 PB/year, assuming two cycles of data processing and possible optimization of the data format and data objects to be stored permanently. We assume that a half of the annual data sample ($\sim$5 PB) is kept on disk storage, and the rest is stored on tape. The CPU power necessary to process the amount of data like this and to run Monte-Carlo simulation is estimated as many as 30000 CPU cores. The summary of computing resources is given in Table. 1.2. The cost estimate is conservative and will be defined more exactly in the TDR, when detailed hardware solutions and their actual price in the market will be considered.

ADD LOW-LUM SCENARIO

The burden of the SPD computing system operation is a subject of sharing between the computing centers of the participating institutes.

1.6.4 Schedule and milestones

TBD

Bibliography

[1] P. Abbon, et al., The COMPASS Setup for Physics with Hadron Beams, Nucl. Instrum. Meth. A 779 (2015) 69–115.

[2] D. Baranov, S. Mitsyn, P. Goncharov, G. Ososkov, The Particle Track Reconstruction based on deep Neural networks, EPJ Web Conf. 214 (2019) 06018.

[3] G. Ososkov, et al., Tracking on the BESIII CGEM inner detector using deep learning, Computer Research and Modeling 10 (20) 1–24.

[4] P. Goncharov, et al., BM@N Tracking with Novel Deep Learning Methods, EPJ Web of Conferences 226 (2020) 03009.

[5] E. Shchavelev, et al., Global strategy of tracking on the basis of graph neural network for BES-III CGEM inner detector, AIP Conference Proceedings 2377 (2021) 060001.

[6] A. Nikolskaia, et al., Local strategy of particle tracking with TrackNETv2 on the BES-III CGEM inner detector, AIP Conference Proceedings 2377 (2021) 060004.

[7] P. Goncharov, et al., Ariadne: PyTorch library for particle track reconstruction using deep learning, AIP Conference Proceedings 2377 (2021) 040004.

[8] M. Al-Turany, D. Bertini, R. Karabowicz, D. Kresan, P. Malzacher, T. Stockmanns, F. Uhlig, The FairRoot framework, J. Phys. Conf. Ser. 396 (2012) 022001.

[9] Key4hep software.
URL `https://key4hep.github.io/key4hep-doc/index.html`

[10] T. Sjöstrand, S. Ask, J. R. Christiansen, R. Corke, N. Desai, P. Ilten, S. Mrenna, S. Prestel, C. O. Rasmussen, P. Z. Skands, An introduction to PYTHIA 8.2, Comput. Phys. Commun. 191 (2015) 159–177.

[11] B. Andersson, G. Gustafson, B. Nilsson-Almqvist, A Model for Low p(t) Hadronic Reactions, with Generalizations to Hadron - Nucleus and Nucleus-Nucleus Collisions, Nucl. Phys. B 281 (1987) 289–309.

[12] B. Nilsson-Almqvist, E. Stenlund, Interactions Between Hadrons and Nuclei: The Lund Monte Carlo, Fritiof Version 1.6, Comput. Phys. Commun. 43 (1987) 387.

[13] S. Bass, et al., Microscopic models for ultrarelativistic heavy ion collisions, Prog. Part. Nucl. Phys. 41 (1998) 255–369.

[14] M. Bleicher, et al., Relativistic hadron hadron collisions in the ultrarelativistic quantum molecular dynamics model, J. Phys. G 25 (1999) 1859–1896.

[15] S. Agostinelli, et al., GEANT4–a simulation toolkit, Nucl. Instrum. Meth. A 506 (2003) 250–303.

[16] J. Allison, et al., Geant4 developments and applications, IEEE Trans. Nucl. Sci. 53 (2006) 270.

[17] J. Allison, et al., Recent developments in Geant4, Nucl. Instrum. Meth. A 835 (2016) 186–225.

[18] J. Rauch, T. Schlüter, GENFIT — a Generic Track-Fitting Toolkit, J. Phys. Conf. Ser. 608 (1) (2015) 012042.
URL `https://github.com/GenFit/GenFit`

[19] S. Gorbunov, I. Kisel, Reconstruction of decayed particles based on the kalman filter, Tech. Rep. CBM-SOFT-note-2007-003, CBM Collaboration (2007).

[20] F. Stagni, A. Tsaregorodtsev, L. Arrabito, A. Sailer, T. Hara, X. Zhang, DIRAC in Large Particle Physics Experiments, J. Phys. Conf. Ser. 898 (9) (2017) 092020.

[21] M. Barisits, T. Beermann, F. Berghaus, et al., Rucio: Scientific data management., Comput. Softw. Big Sci. 3 (2019) 11.

[22] A. Frohner, J.-P. Baud, R. M. Garcia Rioja, G. Grosdidier, R. Mollon, D. Smith, P. Tedesco, Data management in EGEE, J. Phys. Conf. Ser. 219 (2010) 062012.

[23] F. B. Megino, et al., PanDA: Evolution and Recent Trends in LHC Computing, Procedia Comput. Sci. 66 (2015) 439–447.